Universidade de Aveiro Departamento de Física
2007

Daniel Elísio Ferreira Marinha

Preparação e caracterização do supercondutor MgB_2

Preparation and characterization of MgB_2 superconductor

Universidade de Aveiro Departamento de Física
2007

Daniel Elísio Ferreira Marinha

Preparação e caracterização do supercondutor MgB_2

Preparation and characterization of MgB_2 superconductor

dissertação apresentada à Universidade de Aveiro para cumprimento dos requisitos necessários à obtenção do grau de Mestre em Ciência e Engenharia de Materiais, realizada sob a orientação científica do Dr. Vitor Amaral, Professor do Departamento de Física da Universidade de Aveiro e do Dr. Filipe Oliveira, investigador do CICECO

Apoio financeiro do POCTI no âmbito do III Quadro Comunitário de Apoio. Projecto POCTI/CTM/39340/2001

Apoio financeiro da FCT e do FSE no âmbito do III Quadro Comunitário de Apoio.

Este trabalho é dedicado ao meu Pai e à minha Mãe pelo apoio incondicional e em memória da minha Avó.

o júri

presidente

Prof. Dr. Luís António Ferreira Martins Dias Carlos
professor catedrático da Universidade de Aveiro
Prof. Dr. Pedro Manuel de Melo Bandeira Tavares
professor associado da Universidade de Trás-os-Montes e Alto Douro
Prof. Dr. Vitor Brás de Sequeira Amaral
professor associado da Universidade de Aveiro
Prof. Dr. Filipe José Alves de Oliveira
investigador auxiliar da Universidade de Aveiro

agradecimentos

Os meus agradecimentos em primeiro lugar para o Professor. Vitor Amaral pela oportunidade concedida e pela orientação científica. Gostaria de agradecer também ao Dr. Filipe Oliveira pelas engenhosas soluções e capacidade de incentivo; ao Mestre vidreiro António Morais pelo excelente apoio no trabalho com vidro; ao Dr. Augusto Lopes pelo apoio na parte de microscopia; a todos os que de uma forma geral contribuiram para a execução deste trabalho.

palavras-chave física, materiais, supercondutor, prensagem isostática a quente, HIP, MgB_2, boreto, encapsulamento

resumo

Amostras supercondutoras de MgB_2 foram produzidas seguindo os métodos *ex situ* e *in situ* e posteriormente caracterizadas. As amostras *ex situ* foram obtidas recorrendo a sinterizações a 950ºC numa prensa isostática a quente (HIP) sob pressões de 30, 50 e 190MPa. Nestas condições obtiveram-se valores de densidade até 98% da densidade teórica do material. Foram usadas técnicas de XRD, SEM, TEM e EDS para caracterizar as amostras que revelaram uma melhoria do controlo sobre a formação de fases secundárias. Recorrendo a uma técnica de encapsulamento em vidro as quantidades finais de MgO foram limitadas a ~10% (em massa) e a formação de MgB_4 foi impedida. As amostras *in situ* foram obtidas através do encapsulamento de misturas de pós de Mg e B nas proporções molares de 1:2, 1.2:2 e 1.5:2 e posterior sinterização em vácuo num forno de grafite. Deste processo resultaram amostras porosas e com fraca resistência mecânica. Técnicas de SEM, EDS e XRD revelaram grandes quantidades finais de MgO enquanto que a formação de MgB_4 foi evitada. As amostras *ex situ* são supercondutoras com valores de T_c~37K e respectivas larguras de transição na ordem dos 0.5 K. Para além destes resultados, as medidas eléctricas e magnéticas permitiram também determinar os valores de densidade de corrente crítica, J_c, do material. Contrariamente ao T_c, o J_c parece ser sensível às condições de processamento e foram obtidos valores que variam entre 0.37 e 3.89 $x10^6$ A/cm^2 a 10K.

keywords physics, materials, superconductor, hot isostatic pressing, HIP, MgB_2, boride, glass encapsulation

abstract Superconducting bulk samples of MgB_2 were produced, using *ex situ* and *in situ* processing routes, and characterized. *Ex situ* samples were obtained by hot isostatic pressing (HIP) under pressures up to ~200MPa at 950ºC. In these conditions, full densification of samples was obtained (~98% of theoretical density). SEM, TEM, EDS and XRD analysis on final dense bodies were used to evaluate samples. These show increasing improvement in controling the amounts of secondary phases. MgO was limited down to ~10% wt. and complete prevention of formation of MgB_4 by using simple glass encapsulation techniques and addition of Mg(s) to the capsule. *In situ* samples were obtained by encapsulating and sintering a mixture of Mg and B powders with Mg:B molar ratios of 1:2, 1.2:2 and 1.5:2 under vacuum in a graphite furnace. This process resulted in porous samples with poor mechanical resistance. SEM, EDS and XRD analysis have shown large amounts of MgO while MgB_4 formation was successfully avoided. *Ex situ* samples display superconducting properties (T_c~37 K), including narrow critical transition in electrical properties (ΔT_c~0.5 K). Magnetic and electric measurements were performed allowing the determination of critical current density, J_c, and critical transition temperature, T_c, of the material. Contrary to T_c, J_c is quite sensitive to the processing conditions and values from 0.37 and 3.89×10^6 A/cm^2 are obtained at 10K.

Index

List of tables

List of figures

1 Superconductivity

1.1 Brief History

Dutch physicist H. Kamerlingh Onnes was responsible for the discovery of the superconductivity phenomenon while working in what was at the time, the coldest place on earth – the cryogenics laboratory at the University of Leiden. There he worked as professor in experimental physics, thirty one years after he had successfully completed his PhD study with a thesis entitled "Nieuwe bewijzen voor de aswenteling der aarde" (tr. New proofs of the rotation of the earth)[1]. He was studying the electrical behaviour of different pure metals under cooling[1] when he found that mercury showed no electrical resistance below 4.2 K[2]. This value was termed *critical temperature*, T_c, and it refers to the characteristic temperature below which a given material displays no electrical resistance. Onnes reported that after an abrupt drop in the material's resistance to electrical flow below T_c, mercury had passed into "a new state, which on account of its extraordinary electrical properties may be called the superconductive sate." Besides further discovering that tin and lead were also superconductors at similarly low temperatures (3.8 K and 7.2 K, respectively), Onnes performed a series of studies in which he observed that there were at least two more critical values that, similarly to T_c, could not be surpassed if the material was to remain in the superconductive state: the *critical current density* (current intensity per unit of area, J_c) and the *critical magnetic field*, H_c,. The superconductive state can only be observed if all three conditions are met.

In 1933 German scientists Fritz Walther Meissner and Robert Ochsenfeld found a new intrinsic property of the superconductive state: regardless of the experimental conditions, a superconductor will always expel a magnetic field lower than H_c from its interior[3]. This was later called *the Meissner-Ochsenfeld effect* and is nowadays widely used as a mean to evaluate superconductivity of samples. This effect is the reason behind levitation of magnets over superconductors, applied in the construction of the renowned Maglev train projects.

As research advanced several other materials, particularly intermetallic compounds, were found to superconduct at increasingly higher T_c's such as niobium-nitride, vanadium-silicon and niobium-titanium. The maximum was reached in 1973 with niobium-germanium at 23.2 K[4]. This record was kept until the next decade, when in 1986 a new class of superconducting materials made its first appearance in the form of layered copper-oxide ceramics[5]. George Bednorz and Alex Müller found that a sample of lanthanum copper oxide doped with barium was superconductive below 35K. This discovery was a

[1] Onnes had previously been the first person to successfully liquefy Helium, in 1908. He was subsequently able to achieve temperatures as low as 0.9 K. This achievement was what allowed him to probe material's behaviour in such low temperatures, and together with superconductivity, this was the main reason why he has attributed the Nobel Prize in Physics in 1913.

breakthrough in many ways, but perhaps the biggest surprise lies in the fact that ordinary ceramics are insulators at room temperature. This caused some initial reluctance in accepting the reported behaviour to be the same as superconductivity. Later the authors presented the definite proof when they demonstrated the Meissner-Ochsenfeld effect on their sample[6]. Based on their findings that barium doped lanthanum copper oxide ($La_{2-x}Ba_xCuO_4$), similar materials were also presented as superconductors, where barium was replaced with strontium and calcium, with the generic formula of $La_{2-x}M_xCuO_4$ with M = Ba, Sr and Ca. In 1987, research led by M. K. Wu and C. W. Chu made the first entry into the modern high temperature superconductors when lanthanum was replaced by yttrium in $YBa_2Cu_3O_7$, also known as YBCO, reaching an unprecedented T_c above 90 K[7]. The following year the first high temperature superconductor without a lanthanide element in its composition was discovered by Maeda, *et a*[8]. The system of Bi-Sr-Ca-Cu-O, with common designation of BSCCO, yielded T_c's between 110 – 120 K. These and other compounds comprised an all together new class of superconductors. Starting up with a T_c of about 35 K, they revolutionized the way in which superconductivity was being understood, and have reached T_c's as high as 135 K [9] at ambient pressures. Because the critical temperatures of these compounds are quite higher than typical superconductors, these are called *high temperature superconductors*.

Ever since the Onnes' discovery the class of superconducting materials is ever expanding. From the first generation of pure metals, to alloys and finally to complex compounds, spanning several different crystallographic structures, superconductivity is all but rare. Figure 1-1 shows the periodic table where the known superconductive elements are highlighted.

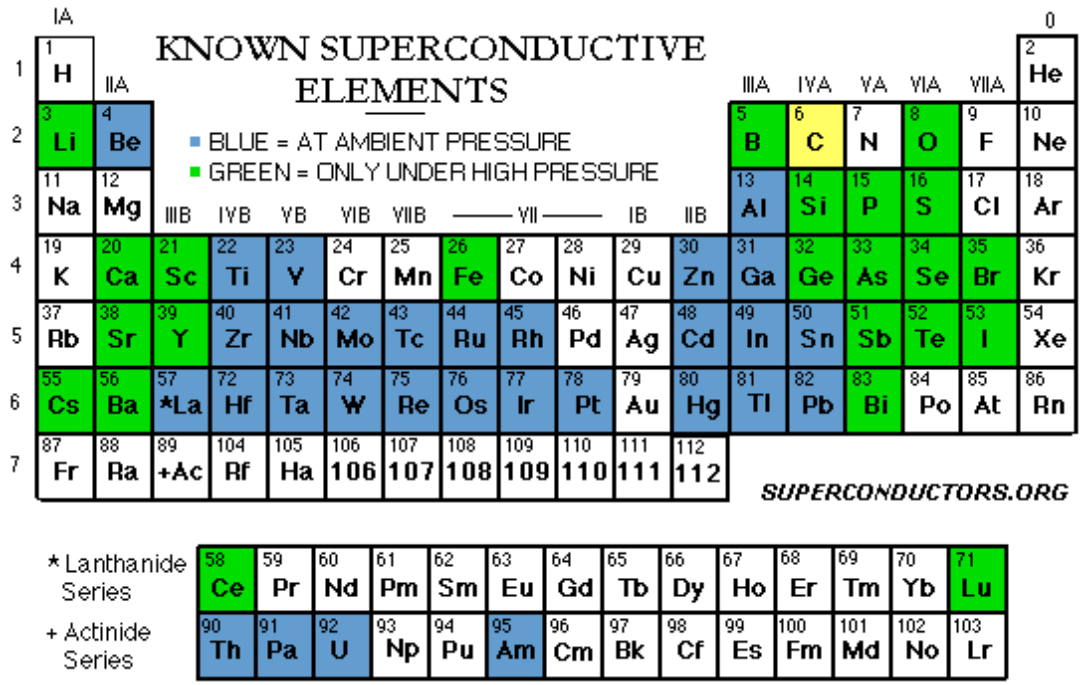

Figure 1-1: Table of known superconducting elements[10].

However, superconductivity remains a phenomenon restricted to low-temperatures. The first goal of research in this field has been the tailoring of superconductors with increasingly higher critical temperatures, but so far these materials are still bound to low temperature phenomena. The fact that these materials must be cooled down to such temperatures implies a great barrier when it comes to designing commercially advantageous applications. The existing market for superconductors is restricted to a small niche of very specific applications. The optimal characteristics that a superconductor should meet in order to make a successful entry into the world of large-scale industrial applications would be: low cost and environmentally friendly raw materials; low cost processing; ease in being shaped into coils, tapes, and complex shaped pieces; sufficiently high T_c value so that refrigeration can be nitrogen-based or obtainable using inexpensive cryocoolers; and high enough J_c and H_c to meet the requirements of the applications.

1.2 Overview on the fundamental properties of superconductors

1.2.1 Zero resistance

The resistivity, ρ, of a metal decreases with temperature, according to Equation 1-1, where m is the mass of the electron, n the number of electrons, e the charge of the electrons and τ is the mean free lifetime, which is the temperature-dependent main contribution in metals.

$$\rho = \frac{m}{ne^2\tau} \qquad \text{Equation 1-1}$$

Upon cooling from room temperature, resistivity will decrease following a linear behaviour. At a given point at much lower temperatures, it tends towards a constant value called residual resistivity. The reason for this behavioural change lies in the fact that at higher temperatures electrical conduction is proportional to the mean free lifetime between collisions of the electrons against the lattice. Upon cooling, the atoms comprising the lattice vibrate less. With lesser scattering, the mean free lifetime increases as temperature decreases. This accounts for the initial linear response. Residual resistivity is the result of impurities scattered in the lattice which are also obstacles for the electrons. At lower temperatures, when the lattice atoms vibrations are almost totally stopped, the mean free lifetime term in the equation is dominated by the amount of impurities, which is constant, thus causing the residual resistance. On the other hand, a superconductor will display a sudden resistivity drop to zero at a given temperature, T_c, below which it becomes an ideal conductor, regardless of the impurities. This behaviour can be seen in Figure 1-2 for the case of mercury.

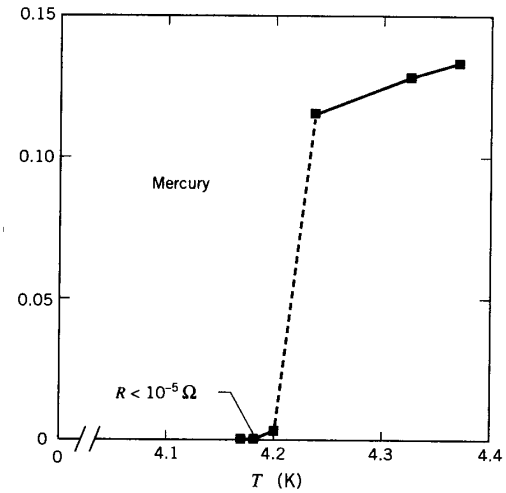

Figure 1-2 – The transition of mercury to the superconducting state, at approximately 4.2 K[2].

As aforementioned, electrical resistivity is a result of the interaction between the electrons and the lattice together with impurities. When in a superconductive state, electrical conduction is still done by electrons, inside the same lattice with exactly the same impurities. If all those are things that remain constant, what must change is the interaction itself.

1.2.2 Meissner effect

In a sense, superconductors are magnetic mirrors. When submitted to a magnetic field, a material in its superconductive state will form superficial persistent currents, which in turn will generate a second magnetic field, in order to exactly counteract the first. In this way, it prevents penetration of the external field inside the material, apart from a small fraction near the surface. Because of this shielding effect, superconductors are said to display *perfect diamagnetism*. There is, however, more to superconductivity than just that. Diamagnetism means that a material will react to a change in an external magnetic field according to Faraday's law, in such a way as to compensate for the change (Lenz's law). This means that above T_c, a non-diamagnetic material would allow permeation of a magnetic field to its interior. If this external field was maintained constant and the material cooled down below T_c, it would become diamagnetic but there would be no reason for the appearance of the persisting currents or the mirror field, because there had been no change in the external field. In these conditions, a diamagnetic material would not shield itself from the external field. What happens is that even when cooled under and externally applied constant field, a superconductor will still completely repel it. This is one of the reasons why one speaks of a superconductive state: under the same experimental conditions a superconductor always displays the same properties.

1.2.3 Types of superconductors

In 1957 Alexei Abrikosov[2] theoretically predicted that superconductors could be divided into two separate categories, type-I and type-II, according to their behaviour under a magnetic field[11]. Experimental confirmation came approximately three years later. Type-I or otherwise called, soft superconductors, are comprised by most metals and metalloids. Examples include mercury, lead and aluminium. Typically they present T_c < 10K and they have a single critical field, H_c, above which the

[2] Abrikosov was awarded the 2003 Nobel Prize in Physics for pioneering contributions to the theory of superconductors and superfluids.

material is no longer able to repel external magnetic field from its interior and it returns to its normal state. The magnetic performance of a type-I superconductor is presented in Figure 1-3. From this figure it is possible to see that as the applied field increases an induced field that exactly mimics and cancels the first one is created by the superconductor, until H_c is reached and the material abruptly undergoes a transition to the normal state, even if it remains below T_c. Type-I superconductors have very low H_c for practical applications. The highest H_c for a type-I superconductor is found in pure lead and it amounts to ca. 800 Gauss, which is too low for most practical applications.

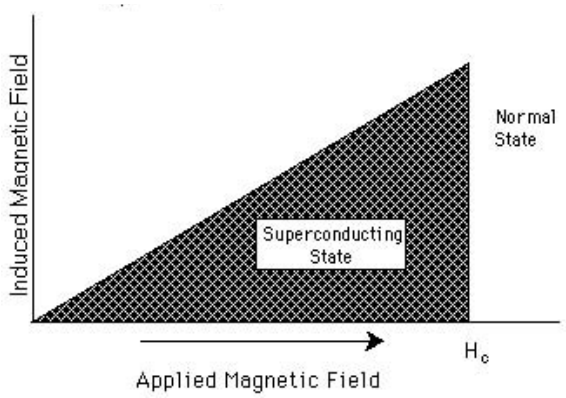

Figure 1-3 – Schematic representation of the induced magnetic field versus applied magnetic field for a type-I superconductor[12].

Type-II or hard superconductors have two distinct critical field values, H_{c1} and H_{c2}, otherwise known as *lower* and *upper* critical fields, as presented in Figure 1-4.

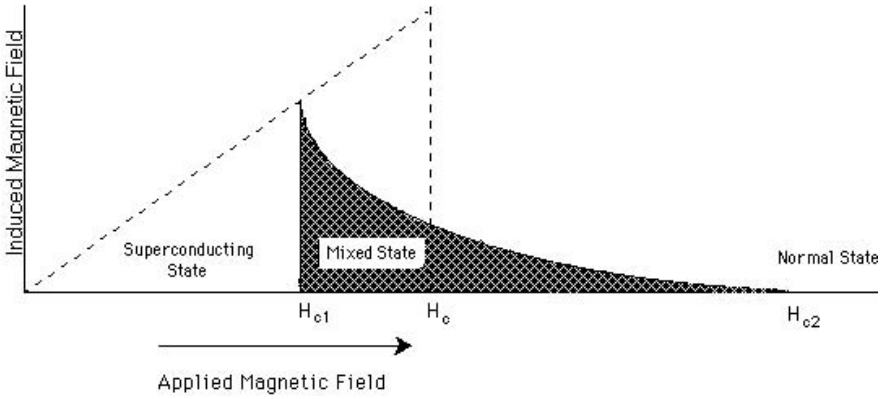

Figure 1-4 – Schematic representation of the induced magnetic field versus applied magnetic field for a type-II superconductor[12].

Increasing the applied magnetic field will cause the induced field to increase as well, as in type I superconductors. But when H_{c1} is reached, the material enters what is called the *mixed state*. This is an intermediate state limited by H_{c1} and H_{c2} where the material no longer expels completely the external magnetic field. Instead, it allows a fraction of the field to intrude in a tubular shape. The material becomes divided into superconducting regions separated by non-superconducting regions. Each of these

tubes is called a *vortex* and all together they form a periodical lattice inside the material called *Abrikosov vortex lattice* (Figure 1-5).

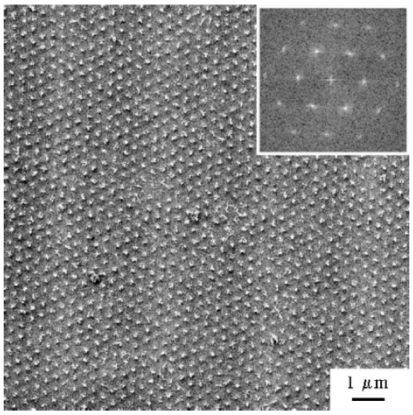

Figure 1-5 – Periodical Abrikosov vortex lattice in MgB_2 single crystal, at magnetic field of 200 Oe[13].

As the applied field continues increasing, so does the number of vortices until H_{c2} is reached and the material transits to the normal state. At low temperatures, the upper critical field can reach values in the order of a hundred Tesla for high temperature superconductors. The vortices inside the material are able to move about, resulting in frictional energy loss and consequently electrical resistance. A superconductor in the mixed state cannot transport electrical current without losses. As the vortices move, they may become trapped, or pinned, at impurity or crystalline defect sites. Due to repulsive forces between them, it only takes a small fraction of them to be fixed to cause the whole lattice to freeze. This pinning effect of the vortex lattice eliminates electrical resistance to current flow, and so it is of interest to attain. However, zero resistance is only restored for direct current and only below a certain field called irreversibility field, H_{irr}. This field is a function of temperature and its typical behaviour is shown in Figure 1-6.

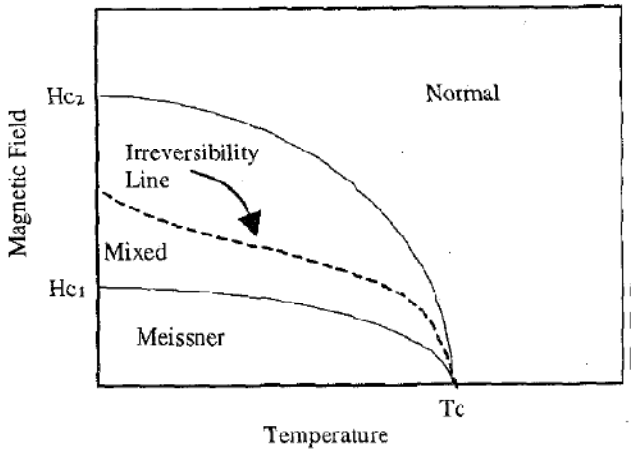

Figure 1-6 - Phase diagram showing the applied magnetic field as a function of temperature, for type II superconductors[14].

Under alternating currents such vortices induce hysteresis which leads to dissipation of energy. This means that a superconductor in the mixed state cannot transport ac current without losses.

These intrinsic physical characteristics of type-II superconductors have made them the election material in all power applications due to the possibility of operating at higher temperatures and magnetic fields. A material with T_c~130 K requires an operating temperature ~90 K which can be obtained through liquid nitrogen refrigerating systems or cryocoolers. This poses all sorts of advantages because nitrogen is relatively cheap, abundant and environmentally friendly.

1.2.4 Superconducting theory

The first attempt to completely model superconductivity was the Ginzburg-Landau theory, developed in 1950, which presented a thermodynamical approach to the macroscopic properties of a superconductor. Later in 1957 came the long awaited BCS theory of superconduction[15], named after its developers John Bardeen, Leon Cooper and Robert Schrieffer, co-authors of the best known and widely accepted theoretical reasoning for the occurrence of superconductivity, so far. It was able to account for the microscopic origins of the phenomenon and could quantitatively predict the properties of some superconductors such as their T_c.

According to the BCS theory, electrons below T_c are able to overcome electrostatic repulsion between them and become bonded in *Cooper pairs*[16] – an indirect attraction between two electrons mediated by the lattice which creates a bound state. Such an interaction between the lattice and the electrons had been initially published in 1950 simultaneously by Fröhlich[17] and Bardeen[18], but Cooper was the first to demonstrate it. In this state, electrons are able to flow through the lattice by condensing into a similar energy level leaving an energy gap separating them from any available higher energy states. At low temperature regions of the superconducting state, the lattice vibrations cannot supply enough energy to overcome the gap and break up the pair. This allows the Cooper pairs to flow unimpeded through the crystal lattice without ordinary electrical resistivity.

Although the BCS theory has successfully described superconductive behaviour for elements and simple alloys in low temperatures regimes, it was found to be inadequate to fully describe all superconductivity phenomena. In fact, it had predicted a theoretical maximum for the T_c of a superconductor of around 30 K – 40 K, which does not account for the whole class of high temperature superconductors.

1.2.5 High Temperature Superconductors

There is no precise definition stating the temperature above which a material should be considered a high temperature superconductor. The term itself was initially used in the renowned 1986 paper by Bednorz and Müller[5]. At the time a T_c of 35 K was more than 10 K above the previous maximum. Nowadays that the record has been set in the orders of the hundred Kelvin, the threshold has increased and "a superconductor is usually referred to as a high temperature superconductor (HTS) if the superconducting state is attained by cooling in liquid nitrogen"[19], i.e., above 77 K. All high temperature superconductors present a type-II behaviour under external magnetic fields. This enables them to remain superconducting under higher magnetic fields than conventional low temperature superconductors (LTS).

Structurally, high temperature superconductors have a perovskite-like crystal arrangement and show an array of different layered structures. They can be grouped into three categories[19]:

- "three dimensional compounds based on $BaBiO_3$;
- layered copper oxide compounds with hole conductivity;
- compounds based on Nd_2CuO_4 with electron conductivity."

The second category of layered cooper oxides, or cuprates, includes some of the most known compounds such as $La_{2-x}Sr_xCuO_4$, $YBa_2Cu_3O_{7-x}$, $BiSr_2CaCu_2O_{8+x}$ and $Tl_2Ba_2Ca_2Cu_3O_{10}$. Of these, the polycrystalline forms of YBCO- and BSCCO-type compounds have attracted most of the attentions in terms of practical applications. All of these materials have at least one CuO_2 crystal plane per unit cell in its lattice. It is believed that superconductivity is strongly connected to the electronic interactions in these CuO_2 planes in which Cu has a mixed valence state, according to the coordination number of oxygen atoms. Indeed, T_c increases with the increasing number of these planes in copper oxide superconductors.

But the same layered structure that makes up the heart of these superconductors is also responsible for their limitations, such as anisotropic behaviour and poor mechanical properties. Common applications for superconductors require them to be drawn into long flexible wires but because high temperature superconductors are ceramic in nature, this is often an issue. These materials have a highly anisotropic superconductive behaviour. This happens because the Cooper pairs are formed via vibrational interactions with the crystal lattice, which makes some directions more favourable than others. In the case of these materials, superconductivity is favoured along the CuO_2 planes. Anisotropy becomes problematic when it comes to polycrystalline pieces, where each grain is randomly oriented and only a small fraction of the material will be correctly oriented in a finished device. When the superconducting current does not flow adequately from grain to grain, either due to relative orientation, crystalline defects, or impurities, these are said to be "weak-linked". The weak link effect is undesirable because it limits the critical current density and critical field values[20].

1.3 Applications of superconductors

Ever since the discovery of superconductivity, a world of practical applications was immediately envisioned: powerful magnets could be built much smaller than existing ones; windings could carry enormous amounts of electrical current without energy loss; smaller electrical generators could generate the same amount of electricity with less energy input which could be distributed without losses; energy storage could rely on superconductors to be retained for large periods of time without losses. Unfortunately, also ever since that day, the main obstacle to wide-spread applications, particularly those that involve operation over large extensions of space, has been the increased costs of very expensive and unpractical refrigeration equipment to produce and maintain the low temperatures required for superconductivity. That is the reason why HTS were considered a giant step forward, which has continued up until now. Helium-based refrigeration is no longer mandatory and can be replaced for cheaper and safer liquid nitrogen or cryocoolers.

Superconducting materials are usually synthesised in the form of bulk, wires (tapes) or film, according to the intended application:

- bulk – structures or devices where a specific shape is necessary
- tapes / wires – where large length is a factor
- film – employed in microwave devices, detectors and microelectronic circuits.

Some superconductors are already well established in some specific areas of application, such as research and industrial applications, particularly NbTi (Tc = 9 K) and Nb_3Sn (Tc = 18 K). Although HTS present the greatest amount of potential in terms of their physical properties, such as higher critical values, they are yet to reach a market position that threatens the overall dominance of both these materials.

The most recognizable of all superconductor applications must be the Maglev train. The underlying concept of operation relies on the Meissner effect that causes the train to be suspended above the rails, thus allowing it to glide virtually frictionless, at speeds up to 550 Km/h. But the Maglev train is still problematic, and has been recently constrained due mainly to environmental concerns regarding the strong magnetic fields that are potentially bio-hazardous. Most of the applications for superconductors are heavily concentrated on superconducting quantum interference devices (SQUID) and susceptometers, used for materials science and bio-physics research. Another example of a solidified market niche lies in biomedical applications. Magnetic resonance imaging (MRI) and nuclear magnetic resonance (NMR) devices require large magnetic fields that enable accurate diagnosis and reduce the need for exploratory surgery and present an optimal opportunity for new superconductors. There are also some applications that are strictly envisioned towards scientific development such as those used high-energy particle physics. These devices also require strong magnets to accelerate particles until they reach velocities in the order of light speed and collide. An example is the Large Hadron Collider (LHC) at CERN. While the superconductor used is, in this case, NbTi, another accelerator using HTS with increased

capabilities, coined the Very Large Hadron Collider (VLHC), is currently being developed. In the first model project, the material of choice was BSCCO but most of these applications were developed with LTS conductors. These are attractive due to their low cost, well known properties, ability to be manufactured into wires, high current densities and to the fact that by now the relationship between material and intended application in these devices is understood, providing a very insuring stability.

In terms of upcoming applications, the biggest potential market for new superconductors is in the area of electric power and magnet applications at temperatures above 30 K. Examples of these are power transmission cables, high-power industrial and ship propulsion motors, utility generators, synchronous condensers, fault-current limiters, and transformers. In these the "benefits of HTS power generation include improved efficiency, thermal management reduction, improved power handling, reduced life cycle costs, and size and weight reduction."[21]

Some of the current production problems to solve for new superconductors are:

- cost: commercially available second generation HTS must be silver sheathed to retain their properties;
- mechanical properties: due to their brittle nature, these materials are difficult to shape into wires;
- materials science: the understanding of these materials is still limited and optimization processes are empirical in nature.

2 Literature review on MgB_2

2.1 Discovery

Magnesium boride has been known as an intermetallic compound for over fifty years[22]. So far it had been used as a typical reagent in chemical reactions. In January of 2001, Jun Nagamatsu presented it has a superconducting material at a conference in Japan[23]. At a time when a great deal of effort in research was being made in the area of HTS, it was a surprise that an extremely simple compound presented a relatively high critical transition temperature at 39 K. It is the highest ever reported for a non-copper perovskite. Superconductivity in boride compounds appears to be of a somewhat controversial matter. There are conflicting results regarding some of these compounds, with some reporting superconductivity while some deny it, where ZrB_2[24, 25], TaB_2[25, 26] are examples. It is believed that these contradictions are due to stoichiometry of the compounds, which seems to play an important role. For example, the stoichiometric compound BeB_2 is not superconducting[27] while $BeB_{2.75}$ was found to superconduct at 0.7 K[28]. For a review on superconductivity in borides, see Buzea and Yamashita[29].

In this family of boride compounds with generic formula MB_2 including non-stoichiometric compounds and binary boride alloys, the highest T_c reported is 11.2 K for $Mo_{0.85}Zr_{0.15}B_{2.5}$[30], roughly four times lower than that of MgB_2. Due to these discrepancies, scientists were quickly triggered into suspecting that superconductivity in MgB_2 arose through a non-conventional mechanism. But soon evidences would start pointing another way. MgB_2 is now recognized as a conventional low temperature, type-II superconductor, albeit having some unconventional properties.

2.2 Crystal structure

X-ray crystallographic studies show that MgB_2 has a theoretical density value of 2.625 g/cm^3[31] and a AlB2-type hexagonal structure (space group P6/*mmm*), which is typical for some transition metals and most lanthanide diborides[22, 32]. The crystal structure has alternating layers of Mg and B atoms (Figure 2-1), with lattice constants a= 3.082±0.001 Å and c= 3.522±0.002 Å[32]. Each unit cell (Figure 2-2) contains one magnesium atom and two boron atoms. The boron atoms are arranged in a honeycombed layer, similar to the ones found in graphite. Each metallic atom is coordinated by 12 boron atoms.

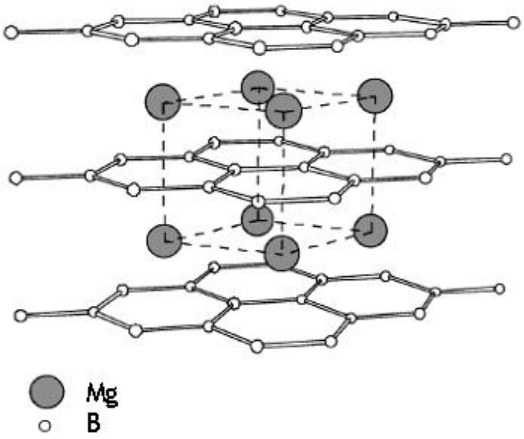

Figure 2-1 – Schematic representation of the crystallographic structure of MgB_2[33].

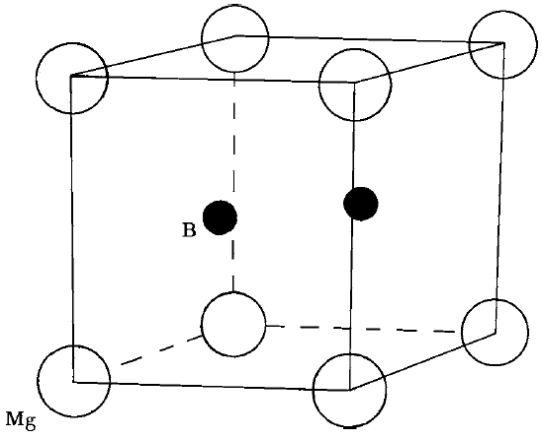

Figure 2-2 – Unit cell of MgB_2[32].

2.3 Mg-B equilibrium phase diagram

Thermodynamical data, and phase diagrams in particular, are key elements to pre-emptively access the behaviour of a compound under different conditions of temperature, composition, pressure and/or atmosphere. This allows modelling and optimization of processing conditions and hint on the final properties of a given mixture of elements or compounds. Regardless of that, such data for all Mg–B compounds seems to be scarce and incomplete. In fact, no experimental phase diagram for the Mg-B system has been reported, and the atomic ratios in stoichiometric compositions of boron-rich phases is an issue still being debated[34].

In 2001 Dou *et al.*[35] reported a model of the temperature-composition, pressure-composition and pressure-temperature phase diagrams, which were calculated using CALPHAD method. In this particular study boron-rich phases with Mg:B molar ratios above 1:7 were not taken into account. The resulting composition-temperature diagrams at two distinct pressures are presented on the next pages. Looking at the diagram corresponding to ambient pressure (Figure 2-3), one can see that at ambient pressure the MgB_2 phase is stable up to 1545 °C, coexisting sequentially with solid, liquid and gaseous Mg, as temperature increases. Above this temperature, it decomposes into gaseous Mg and MgB_4. These results were substantiated by an independent publication in 2002 by Brutti *et al.*[34].

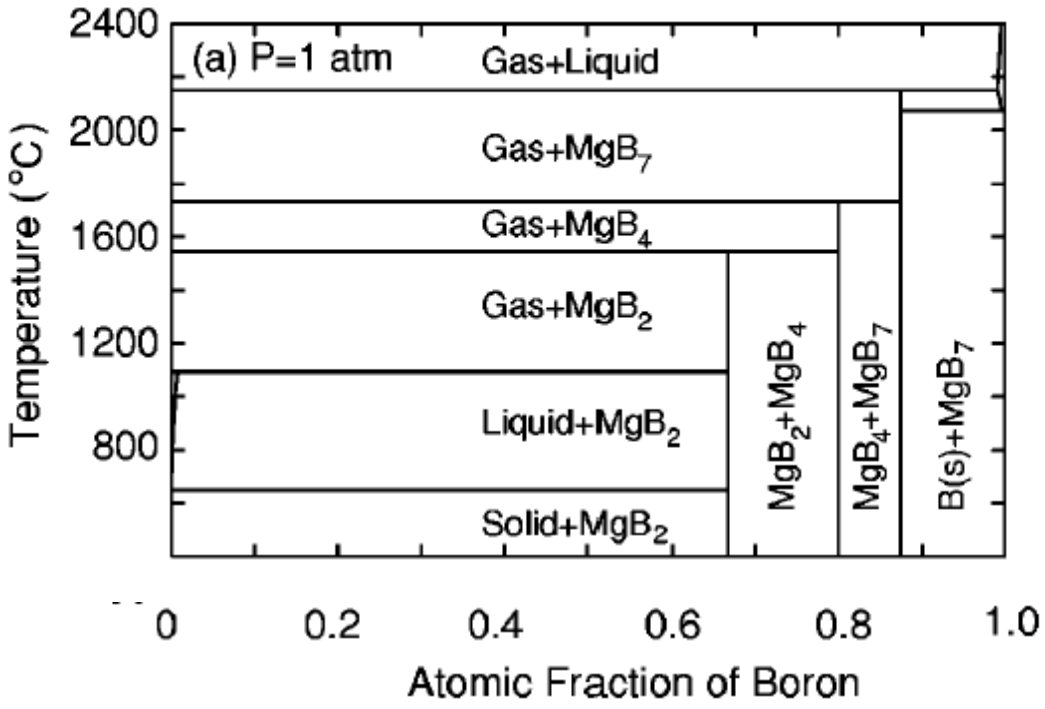

Figure 2-3 – Computer-modulated temperature-composition phase diagrams for Mg-B system at atmospheric pressure[35].

Dou's work also showed that decreasing the pressure to 1 Torr (~10^{-3} atm) severely influences the decomposition temperature, lowering it to 912°C (Figure 2-4). The effect of pressure on the composition of a compound is paramount for film processing techniques which occur under vacuum conditions, but also for apparatus that apply external pressure to the material.

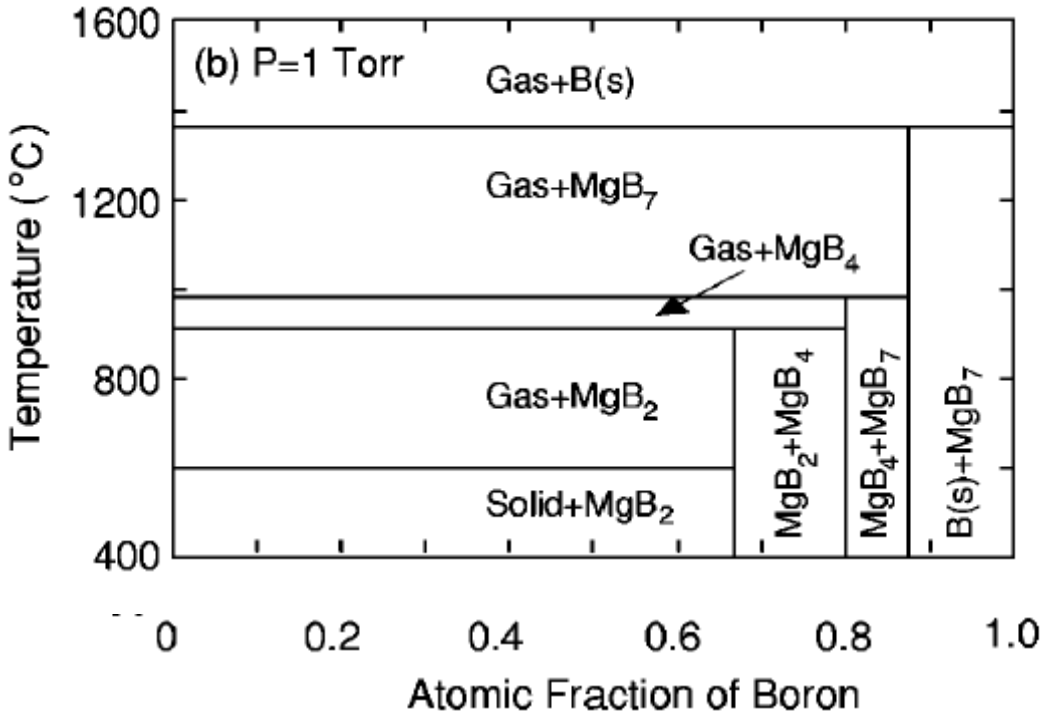

Figure 2-4 – Computer-modulated temperature-composition phase diagrams for Mg-B system at P=1 Torr[35].

Most recently, in 2005, two separate research groups published alternative phase diagrams. Cook *et al.*[36] reported a decomposition temperature of 1268 °C, which is significantly lower than the one obtained by Dou *et al.*. The phase diagram determined by Cook *et al.* is reproduced below in Figure 2-5.

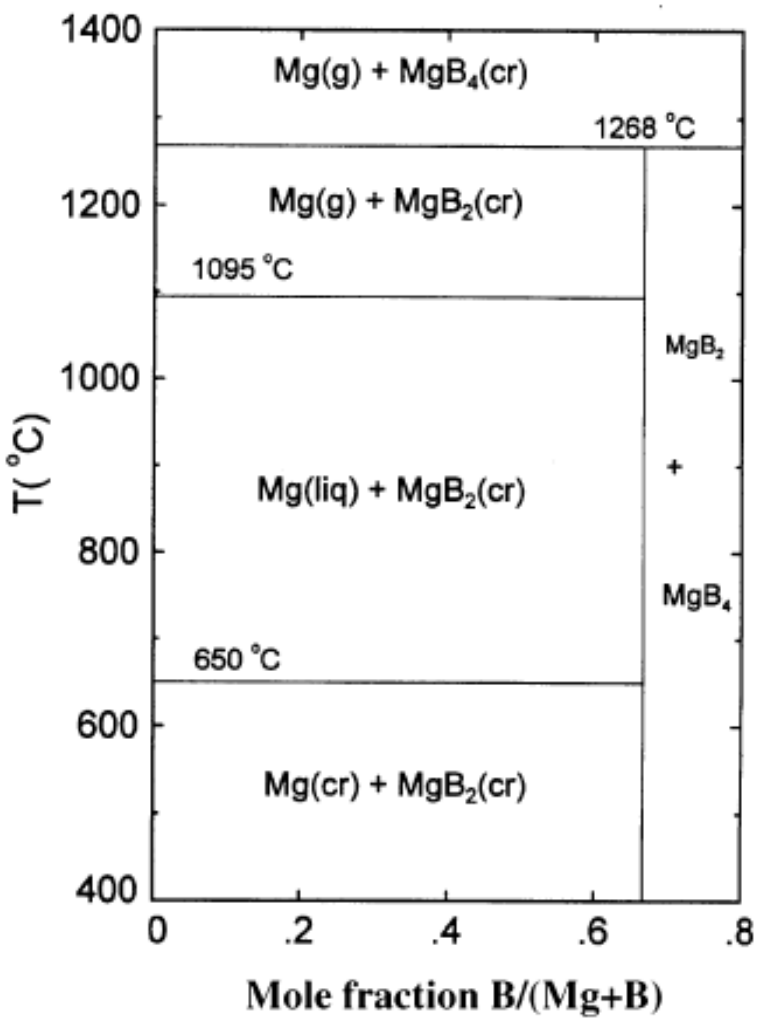

Figure 2-5 – Calculated phase diagram for the Mg-rich region of the Mg-B system at ambient pressure[36].

On the other hand, a paper published by Balducci *et al.*[37], in which new data together with a reassessment of the previous data reported by Cook *et al.* is presented, 1707 °C is pointed out to be the decomposition temperature of MgB_2. The phase diagram obtained and published in that work can be seen in Figure 2-6.

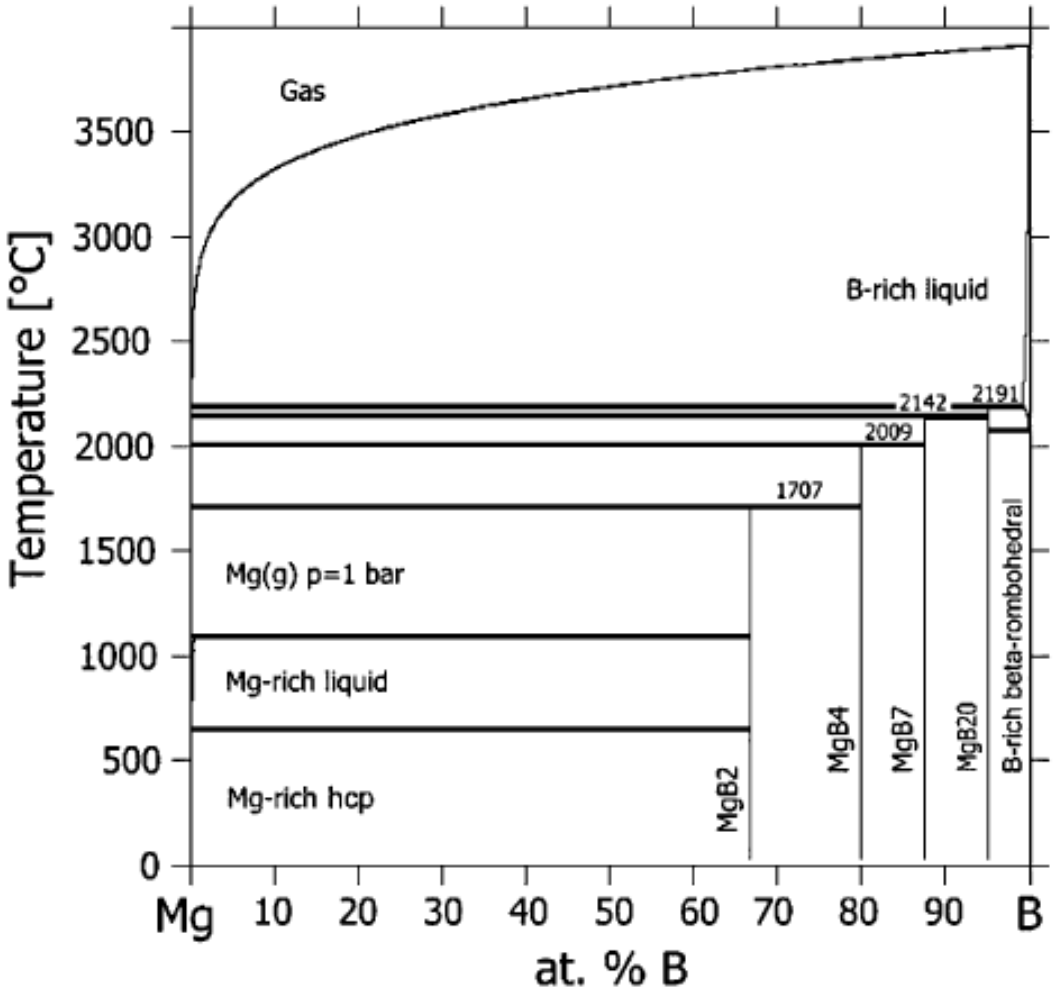

Figure 2-6 – Calculated Mg-B equilibrium phase diagram at ambient pressure[37].

The dispersion in these values and corresponding diagrams is eloquent in demonstrating the need for consolidation of the thermodynamical data regarding the Mg-B system.

2.4 Preparation methods

There are several ways to synthesize superconducting MgB_2 into a wide range of sizes and shapes with different properties. Once all the parameters, operating conditions and the material's behaviour are well understood, these different processing methods can be used to engineer the material in a way that best fits a given application. Until that point, most of the work is typically empirical in nature. However MgB_2 made such an impact that it was almost immediately being processed in a variety of forms, from single crystals to polycrystalline bulk samples, including thin films, wires and tapes.

There are two main approaches into the fabrication of MgB_2, according to whether the compound is formed prior or during the sintering step. These are commonly called *ex situ* and *in situ* methods, respectively. In this chapter the different preparation methods leading to the different forms of MgB_2 will be briefly reviewed, and this differentiation will be made evident, whenever applicable. Stronger emphasis will be made in the preparation of bulk samples.

2.4.1 Bulk

Because in principle the process is simpler, initial practical research on a new material is mainly focused on bulk samples. The accumulated knowledge acquired during this process can then be extrapolated to other methods. Bulk MgB_2 samples can be obtained following either the *ex situ* or *in situ* methods. In the *ex situ* preparation method, commercially available MgB_2 powder is packed into a die, pressed and then sintered in different conditions of pressure/temperature. The sintering step serves the single purpose of densifying the powder into a compact solid. *In-situ* processing is basically the same as reactive sintering. In this case the powder is comprised of a mixture of the desired elements, which then follows the same steps as the *ex-situ* method. The sintering step must be chosen between a range of temperatures which will cause the powder mixture to react and form the desired compound, followed by densification. This method has the additional advantage of allowing some control over the stoichiometry of the compound. It also allows doping the material with different elements. In the case of *in situ* processing some care is required due to the fact that magnesium melts at approximately 650 °C, which is below the temperature of MgB_2 phase formation[38]. Many different ways have been used to sinter bulk MgB_2. They can be divided into three categories according to the pressure applied during that stage.

2.4.1.1 High pressure sintering

The high pressure methods require multiple-anvil apparatus and typical sintering pressures applied are in the order of several GPa[32, 39-46]. In these cases the sample sizes are very small[39, 42, 44], typically in the order of a few millimetres, which makes them impracticable for any ends other than research. They are however fully densified[39, 40, 43] by the end of the process and with good mechanical properties, with reported density values that even surpass that of the theoretical value of MgB_2[39, 42]. This is probably due to the presence of other phases that went unaccounted for in the calculations.

Albeit the extreme pressures applied, sintering is performed at similar temperatures used in methods that don't require such high pressure values. The lowest sintering temperature reported was 700°C, used by Angst *et al.*[42]. However, sintering was performed for 8 hours under 5.5 GPa. The typical sintering temperature in the above mentioned references is situated around 950°C. Although it is clear that pressure has a strong effect on the final sample density, the effects on the superconducting properties seem less obvious. Although at the time they presented significant improvements on the results first reported by Nagamatsu, it became evident later when lower pressure methods were employed, that the highest contribution of pressure-assisted sintering was in deed to the densification of the samples. High pressure methods were widely used initially after the discovery of superconductivity in MgB_2, probably because that had been the way Nagamatsu's sample had been processed. These methods were replaced by others involving lower pressures and have fallen to more or less into disuse in recent years, the two latest reports being those of Prikhna *et al.*[41] in 2004 and Kalavathi *et al.*[46] in 2005.

2.4.1.2 Ambient and low pressure sintering

The logical tendency for any process is simplification. There have been many attempts to produce MgB_2 samples recurring to low pressure sintering [47, 48], ambient pressure[32, 42, 49-51] or in vacuum conditions. Although it is relatively simple to obtain superconducting MgB_2 samples, it is the control over secondary phases, sample densification and related mechanical resistance of the material, which instead turn into issues resulting from this method. Synthesis at low pressures typically originates highly porous samples[43, 48] due to either decomposition of MgB_2, in the case of *ex situ* processing, or Mg evaporation for the *in situ* route. Because of poor densification some samples lack mechanical resistance[32] and are too fragile even to be handled. To minimize the loss and oxidation of magnesium, encapsulation techniques are used, where the material is inserted into a capsule which is then sealed, often under vacuum. Different encapsulating techniques have been used, from simply wrapping the starting material in tantalum foil[32, 51], to inserting it into quartz ampoules[50], iron or tantalum tubes[48] which were sealed later on, and sometimes a combination of these[52]. Whenever there is no encapsulation, inert sintering

atmospheres such as Ar[32, 49, 50] and He[52], or reducing atmospheres such as H_2[43], are used. Typical XRD patterns for samples resulting from low pressure methods indicate the presence of MgO[47, 48] and sometimes MgB_4[48], the most common secondary phases when no additives are used. Both phases appear as a result of MgB_2 decomposition. Upon heating, once the decomposition temperature of MgB_2 is reached, it decomposes into MgB_4 and frees magnesium, according to Equation 2-1[34].

$$2MgB_2 \xrightarrow{T} MgB_4 + Mg \qquad \text{Equation 2-1}$$

The free magnesium will easily react with any available oxygen to form MgO, according to Equation 2-2.

$$Mg + {}^1/_2\, O_2 \xrightarrow{yields} MgO \qquad \text{Equation 2-2}$$

MgO can also already be present in the initial composition, or it can be formed during sintering from oxidation of free magnesium eventually present in the powder mixture.

The superconducting properties reported by research groups using these methods are usually obtained through magnetic instead of transport measurements[47], due to both the frailty of the material and presence of secondary phases, including porosity, which most of the times constitute barriers to current flow.

Amongst the best overall results are the samples produced by a variant of the *in situ* method, termed reactive liquid Mg infiltration method[53]. In this method a pre-form of crystalline boron powder is pressed and sintered in the presence of magnesium, which is added in massive form, inside a sealed container which should be in close contact with the pre-form. During thermal treatment, the liquid magnesium will infiltrate and react with the boron in the pre-form, resulting in samples with relative densities above 90% and in a variety of shapes, including hollow pieces and wires[53]. With T_c in the range of 39 to 40 K and J_c in the 10^5A/cm^2 up to 3 T, these samples presented excellent results both in terms of superconducting as well as structural properties.

2.4.1.3 Medium pressure sintering

Medium pressure methods make use of hot isostatic pressing (HIP) apparatus that apply pressure to the samples during sintering that reaches up to 200 MPa. This was originally how Nagamatsu produced the first superconducting MgB_2 samples. Mentioned in the corresponding seminal paper, are the remaining preparation conditions: *in situ* sintering of a stoichiometric mixture of the elements at 1246 °C and 196 MPa for 10 hours. Results included the X-ray diffraction pattern, the magnetic and transport results. No reference was made in that or any other following paper, as to the density of the samples or their

microstructure was made. Evaluation of the superconducting phase volume of the sample done by magnetic measurements at 5 K resulted in 49%.

Allied to the advantages of using pressure-assisted sintering, HIP also allows for larger samples with complex shapes to be produced. Nonetheless, few studies have been performed using HIP methods to produce the samples. Among them is included the work of Frederick *et al.*[54], which have succeeded in producing MgB_2 samples at lower sintering temperatures and times than those used in high pressure methods. In one of their publications, they stated that simple HIPing of pre-prepared MgB_2 powders was insufficient to produce dense samples[54]. To ensure densification samples were wrapped in zirconium and tantalum foil and encapsulated in glass capsules, which were then sealed under vacuum. Separate capsules were sintered at two different temperatures, 850 °C and 1000 °C, for 2.5 hours at 200 MPa. Sintering at the lower temperature resulted in samples that lacked mechanical strength, albeit having relative densities above 90%. Those sintered at higher temperature had relative densities above 100%, similarly to what was reported for high pressure methods[39, 42], and were much more resistant to handling. No XRD results were presented or discussed. Despite the poor mechanical strength (the samples were said to "not have resulted in a solid compact"), the samples sintered at 850 °C were superconducting with T_c ~ 36.8 *K* according to susceptibility measurements. In transport measurements, samples sintered at 1000 °C had T_c ~ 37.5 *K*. The main difference was found in the transition width, ΔT_c, which was approximately 0.5 *K* for the 1000 °C samples and ~11 *K* for the 850 °C.

Months later, the same group reported a similar work where samples had been fully densified using a HIPing cycle at 950 °C and 100 MPa for 4 hours[55]. XRD revealed the presence of secondary phases MgO and MgB_4 indicating that MgB_2 had decomposed during sintering. Because no XRD of the initial powders was presented, it is not possible to conclude if oxidation had occurred during sintering, or if it was already present in the initial composition. Microstructural evaluation showed that starting with average particle size of 1 μm, grain sizes reached 150 μm. Grains consisting in B-rich phases were visible in SEM micrographs, appearing as darker islands in the matrix (Figure 2-7). T_c of 37,5 *K* was determined by susceptibility measurements and J_c found to be in the order of 10^6 A.cm^{-2} at 20 *K* at zero field, similarly to the values reported for the samples in Ref. [54], but more importantly, to samples obtained recurring to high pressure methods.

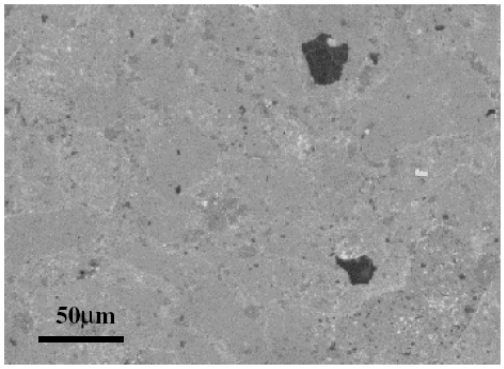

Figure 2-7 – SEM micrograph of a HIPed MgB2 (grey matrix) sample with B-rich grains (darker grains)[55].

Serquis *et al.* have made a comparative study between HIPed samples and sintered at ambient pressure[56]. An MgB_2 sample was synthesized *in situ* using an atomic ratio of Mg:B = 1:1. The mixture was wrapped in tantalum foil and sintered at 900 °C for 2 hours under flowing argon. This sample was characterized as to its magnetic and electrical properties and then ground back to powder and used to make another sample, this time by HIP. This second sintering was performed for approximately 3,5 hours at 1000 °C and 200 MPa and followed the same characterization procedures as the first sample. A third sample was prepared in HIP following the *ex situ* processing route. No results regarding the composition of the samples or their densities were presented. The first interesting result is that susceptibility measurements revealed that the two first samples had higher T_c's (roughly 1 K higher) and sharper transitions than the third sample. Among the two first samples, the HIPed one had the highest T_c. In terms of critical current densities, they found that although both *in situ* samples had similar values at 0 T, the third sample performed better with increasing magnetic fields. It is believed that this was due to flux pinning enhancement caused by crystalline defects and microstructural changes that had occurred during the HIPing process. SEM micrographs (Figure 2-8a and b) show the differences aspect the HIPed and un-HIPed samples' microstructure.

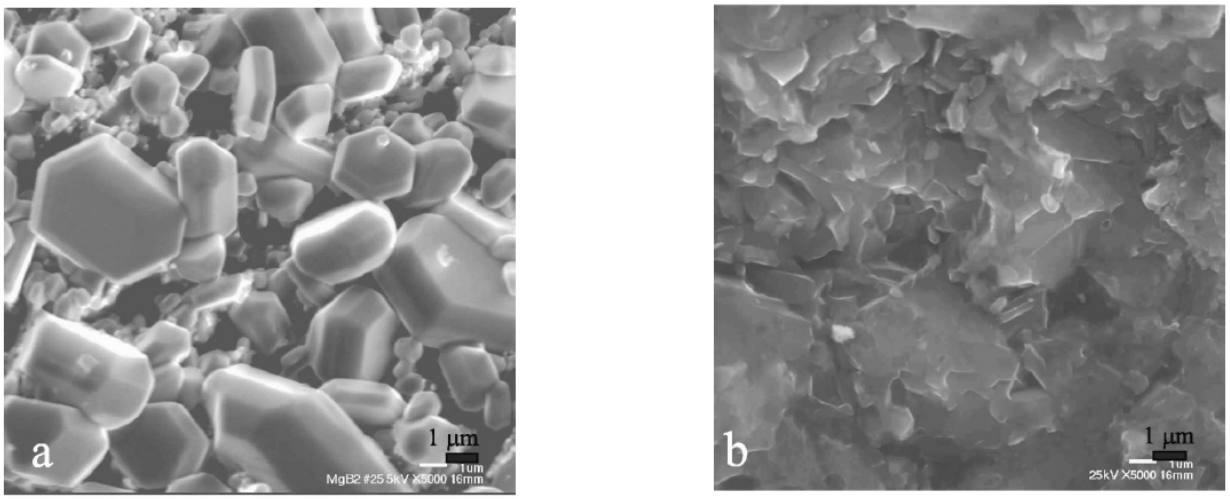

Figure 2-8 – SEM micrographs of sample surfaces of: a) *in situ* sample sintered at ambient pressure, with well developed grains (0.3 – 0.5 µm) and poor connectivity; b) HIPed *in situ* sample, with noticeable improvement in intergranular connectivity[56].

When samples were observed using TEM, MgO was found at the grain boundaries of MgB_2 grains of the un-HIPed sample and evidence of porosity was described. MgB_2 grains in the HIPed sample were clear or at least, MgO was not detected. Conclusions of these study state that although HIPing reduced sample's T_c, it had improved J_c by enhancing flux pinning. The reduction in T_c is explained by the fact that the same sample had been sintered twice, possibly leading to changes in composition. HIPing also reduced porosity of the sample and MgO was either absent, which is unlikely, or it was finely dispersed in the matrix, perhaps aiding and enhancing the flux pinning effect. Comparison between *ex situ* and *in situ* shows that the former results in samples with higher T_c values.

Serquis *et al.* went on to produce MgB_2 wires by *ex situ* PIT method[57]. The wires were then HIPed at 900°C and 200 MPa for 0,5 hours. A second set of samples annealed at ambient pressure was used for comparison with similar conclusions regarding the advantages of HIP processing. These conclusions were confirmed in a TEM microstructural study on the presence of defects of HIPed wires.

HIP has also been successfully used in chemical doping of MgB_2. After finding that doping MgB_2 with Si, C and SiC particles increased J_c of samples up to $2.4x10^5$ A/cm^2 at 2T and 20K, which is an order of magnitude higher than those of undoped samples, Dou *et al.* used HIP to improve densification of the samples[58]. Densification in their previous samples processed at ambient pressure was lower than 50%. As a result of doping, T_c decreases by as much as 2.7 K and hinders densification, while increasing flux pinning effects and consequently, J_c[59]. The addition of these dopants promotes also the appearance of secondary phases such as Mg_2Si, MgB_2C_2 and Mg_2C_3, which are believed to be the reason behind enhanced flux pinning.

Senkowicz *et al.*[60] have also produced HIPed MgB_2 samples doped with carbon, but following a different strategy. Pre-reacted MgB_2 powder was high energy ball milled with powdered graphite with nominal compositions of $Mg(B_{1-x}C_x)_2$ with $\times = 0.0525$ and $\times = 0.17$. The mixture was encapsulated into steel tubes under vacuum, and then HIPed at 1000°C and pressure above 200 MPa for approximately 3,5 hours. The resulting samples were "black, lustreless and lacked mechanical strength". They encapsulated the samples again, this time adding extra magnesium so that during sintering they would be exposed to magnesium vapour. Heat treatment was performed at 900°C for 5 hours. Samples were now dense and hard, although XRD peaks had lower intensities and were broader than before. The best sample was the one with $\times = 0.0525$ with $T_c = 35$ K and J_c in the order of 10^5 A/cm^2 at 20 K and 2 T. These are similar results to the ones obtained by Dou *et al.*[58].

2.4.2 Wires and Tapes

Fabrication of superconducting wires and optimization of their properties is fundamental for most practical applications and particularly, those that represent today's biggest market for these materials: the biomedical and research devices. As expected, MgB_2 wires were processed very soon after Nagamatsu's discovery. The first wires produced were reported by Canfield *et al.* and were obtained by diffusion of gaseous magnesium into pre-forms of boron fibbers with a tungsten core[61]. Following an *in situ* method, a nominal mixture of magnesium and boron fibres were sealed in an ampoule, sintered for one hour and then quenched to room temperature. With a J_c in the order of 10^5 A/cm^2 at 5 K and zero field, dropping to 10^3 A/cm^2 at 20 K and zero field, this successful first attempt showed promising results and a second group soon reproduced this method with slightly poorer results[62]. Both groups obtained short wires due to the limitation in the boron fibber's length.

Although most wires and tapes reported are usually short, in the order of a few centimetres, long coils up to 100 meters have already been processed[63]. The main fabrication procedure of metal clad MgB_2 wires and tapes is the powder-in-tube or PIT method, following either the *in situ* or the *ex situ* approach. In this method pre-reacted MgB_2 powder or Mg+B powder mixture is inserted into one or several metallic tubes. These tubes are then cold-drawn into thinner wires which can be rolled into the shape of tapes, or maintained to obtain wires. This is followed by heat treatment, optional in the case of *ex situ* processing, with the purpose of densifying and reducing tensions in the final piece. The sheathing metal has to be ductile and should act as an effective barrier to magnesium evaporation and diffusion, and at the same time it shouldn't affect the superconducting properties of the core material. Metal sheaths used so far include Cu[43, 48, 59, 64-71], Fe[35, 59, 72-79], Ag[59, 66, 80], Ni[72, 74, 81-83], Nb[79, 84] and Ta[79].

Grasso *et al.* obtained MgB_2/Ni superconducting tapes with J_c values in the order of 10^5 A/cm^2 at 4.2 K without any heat treatment[80]. Suo *et al.* have managed to produce dense monofilamentary MgB_2/Ni tapes, with J_c as high as 2.3 x 10^5 A/cm^2 at 4.2 K and 1.5 T with an annealing step at 980 °C for 30 minutes[72]. A value above 1000 A for critical current was determined by extrapolation to zero field. Working with Fe-clad MgB_2 wires, annealed at 800 °C for 3 minutes, Wang *et al.* have attained J_c in the order of 10^5 A/cm^2 at 10 K and 2 T[35]. Grovenor *et al.* have produced wires in which J_c reached 10^6 A/cm^2 at 4.2 K in self-field with an annealing using annealing temperatures from 850 °C to 110 °C[84]. By doping the MgB_2 with SiC nanoparticles, Wang et al. have managed to increase J_c values up to 10^6 A/cm^2 in zero field and up to 10 K, and 10^5 A/cm^2 for 30 K and zero field, 20 K in 2 T and 10 K in 4 T[70].

HIP can also be used in the annealing step of PIT processing method. It has been done by Serquis *et al.*[85, 86] with the same advantages as for the case of bulk samples: increased densification, enhancement critical current densities and irreversibility field. The 25 m long wire was able to generate a magnetic field of 1 T at 25 K in self-field.

2.4.3 Thin Films

Superconducting thin films are used for electronics devices, as is the case of Josephson junctions, and for superconducting quantum interference devices (SQUID). There are many reports by groups that have successfully prepared MgB_2 thin films. Some issues in the preparation of these films are similar to the ones found in the remaining processing methods, such as high volatility of magnesium and its strong tendency to oxidize. But in the case of film processing there is a particular problem: the great difference between the vapour pressures of magnesium and boron. There are many ways to prepare these films, and in a variety of substrates. Common processing methods include pulsed laser deposition[87-94], Mg diffusion[95-97], molecular beam epitaxy[98-101] and magnetron sputtering[58, 65, 102-104]. Thanks to the hexagonal structure of MgB_2, which is able to accommodate substrates with different lattice parameters, films have been grown on different substrates such as Al_2O_3[87, 89, 91, 94, 103], SiO_2, $SrTiO_3$[58, 100, 105] and MgO[97, 102, 106].

These methods can also be divided into *in situ* and *ex situ* techniques, the first requiring a single step for the preparation of the film, and the second being a two step preparation method (film deposition and annealing). The *ex situ* method has been the most used to attain good crystallization and superconducting properties, but has the disadvantage of not being able to produce multi-layered films, while the *in situ* method the opposite happens. For applications in electronics, single-step processing is highly desirable.

2.5 Chemical Doping

MgB_2 has the advantage of having a relatively high T_c, but its behaviour under magnetic fields still leaves some room for improvement. One way to increase the critical current densities is to enhance flux pinning. This can be done in different ways, but the most common and perhaps, most practical, is through chemical doping. By doping the material it is possible to add extra pinning centres in the materials' microstructure in different ways, depending on the nature of the dopant and the chemical interaction with the matrix.

Doping of MgB_2 has been experimented in a variety of ways, but it has been claimed to be misreported for all cases except for carbon, aluminium and manganese[107]. According to Cava *et al.* other elements do not meet the criteria for successful chemical doping, and most reported doping attempts were unable to control the formation of secondary phases that appear due to decomposition of MgB_2 and oxidation of Mg. Despite that, doping has been studied extensively, and there are many reports in which magnesium and boron have been partially replaced by using elements such as C [35, 58, 94, 108-117], Al [70, 85, 118-128], Si [70, 118], Zr [76, 129, 130], Ti [49, 51, 75, 129-134], Fe [98, 135, 136], Ag [70, 130, 137], Na [43, 138, 139], Li [32, 118, 129, 140-142], Cu [136, 143-145], Ca [94, 146], Co [147, 148], Mo [75], Y[75], Zn [70], Pb [42, 149], Hf [131], Ir [150, 151], Sn [147] and Mn [152]. Some compounds have also been used as dopants, including $ZrSi_2$ [49], Wsi_2 [49], ZrB_2[24, 49], Si_3N_4 [51, 153], Y_2O_3 [43], $MoSi_2$ [51], SiC [51, 70, 154, 155], SiO_2 [124, 155, 156], Al_2O_3 [124, 157, 158] and polycarbosilane (PCS)[51]. All of these papers report a drop in T_c with doping, as steep as 17 K in the case of carbon doping[115], depending on dopant concentration, although carbon was also reported by Hol'anova *et al.*[110] to improve the irreversibility field, and J_c by Pogrebnyakov *et al.*[114].

The most common reason for T_c drop reported are chemical pressure effects[75, 130, 137, 149], formation of secondary phases and hindered percolation due to grain boundary segregation of doping elements[113] or resulting reaction phases[120]. On the other hand, J_c is increased as a result of enhanced flux pinning effects when compared with their undoped counterparts. The exceptions to this were found in samples that actually denote a drop in J_c as well as T_c [43, 115, 124, 126, 135, 157]. Most of these dopants also lead to poorer mechanical properties of the samples, with the appearance of secondary phases and low sample densities, with the exceptions of those doped with titanium[49, 129, 130, 134], copper[143] and zirconium[76].

Some of the best results in terms of J_c include those of samples doped with PCS with $3.6x10^5$ A/cm^2 at 8T and 10K[51], SiC with $1.4x10^5$ A/cm^2 at 10T and 4.2K [51], Zr with $1.8x10^6$ A/cm^2 at self field and 20K [129], Ti with $1x10^6$ A/cm^2 at 0T and 20K[130] and Cu with $5x10^5$ A/cm^2 at self field and 20K[136]. J_c values are usually difficult to compare because they are taken at different conditions of temperature/field that vary from publication to publication, even if the results are coming from the same research team.

2.6 Physical properties

2.6.1 Anisotropy

The knowledge of anisotropy is important not only for a better understanding of the properties of a material, but also in devising practical applications for that material, since it strongly influences pinning characteristics and critical values.

MgB_2 is an anisotropic material. Due to its layered structure, measured values of field and electric currents will vary depending on their orientation relatively to the crystallographic alignment. These anisotropic differences can be assessed and quantified by measuring the properties on single crystals. In the case of polycrystalline samples where the grains are randomly oriented, this characteristic is not fundamental to the materials' final properties, and the obtained values are an average. It becomes much more significant in the case of drawn wires where the grains tend align perpendicularly to the applied pressure, and in films, where the sample is textured as the grains are lined up against the flat surface of the substrate.

The anisotropy of H_{c2} can be evaluated from the anisotropy ratio,$\gamma = \frac{H_{c2}^{ab}}{H_{c2}^{c}}$, where H_{c2}^{ab} corresponds to the critical values measured along the crystallographic a-b plane and H_{c2}^{c} is the same value measured along the c axis. While some groups have found a constant value for γ below T_c[159], most results published point to a dependence of this value with temperature, decreasing as temperature approaches T_c[38, 42, 58, 160]. γ values reported from measurements in single crystals near 0 K vary greatly, ranging from 1.6 to 6[161].

2.6.2 Critical magnetic fields

The lower critical field values, H_{c1} at 0K have been determined to be H_{c1}^{ab} ~ 120 mT and H_{c1}^{c} ~250mT by Caplin *et al.*[159], which have recognized a potential use in microwave applications if these values could be attained in textured films.

The higher critical field, H_{c2}, indicates the capacity of a material to maintain superconductivity under external magnetic fields and is an important property in determining its potential applications. Similarly to the other values presented in this chapter, these values vary widely from sample to sample. Measurements at 0K in single crystals have resulted in H_{c2}^{c}values which vary from 3.2 T to 7 T, and in H_{c2}^{ab} ranging from 14.6 T up to 21 T[107, 160, 162, 163]. H_{c2} has also been determined for single crystals doped with aluminium and carbon. Results at 0K show that H_{c2} decreases with the increase in doping levels for the former[120]. For samples doped with C it was found that H_{c2}^{c} increases with increasing doping level with a maximum at 11.3 T and H_{c2}^{ab} only increases up to a certain doping level, reaching a maximum at 35.4 T[164].

In a study by M. Kiuchi *et al.*[165] two undoped samples of MgB_2 with different processing conditions and two B_4C and SiC-doped samples were evaluated as to their H_{c2} values. The highest value for the undoped samples was attained in a sample sintered at 600 °C for 24 hours with 14.5 T, against the 9.8 T for a sample sintered for 12 hours but at 950 °C. In the doped samples the values were similar with 17.9 T and 18.4 T for the B_4C and the SiC doped, respectively. Doping the samples can further increase this value to 25 T as in the case of carbon doping[133], or 40 T as reported for a SiC-doped sample by Matsumoto et al.[166]

2.6.3 Irreversibility field

Ultimately, the irreversibility field, H_{irr}, is the value above which a superconductor loses the ability to carry current without losses. Among the studies on irreversibility field of bulk samples, one can find values as different as 3.3 T[43], 3.8 T[130], 4.2 T[35], 5.2 T[51] and 5.7 T[59], at 20 K for undoped samples. Du *et al.*[51] have stated that this discrepancy in reported H_{irr} values for stoichiometric MgB_2 hinders a systematic comparison of the results and raises the possibility that the actual composition of the samples is not accurate, which would justify the different results. One other possible explanation may be the eventual differences in microstructural characteristics of the samples.

2.7 Attractiveness and potential

It is of common agreement that Nb-Ti and Nb-Sn-based LTS that have ruled the market of practical applications for the last four decades have reached their limits. They are now being replaced by the HTS, such as silver-sheathed BSCCO, that have been under strong development since the 1980's. These have already reached a point in their development that allows them to threaten the market position of the conventional superconductors. The alternatives are not limited only to HTS.

Regardless of being a newcomer in this field, MgB_2 is already considered a good alternative to conventional LTS and HTS, providing an intermediate solution between both. This situation was acknowledged by Scanlan *et al.* in a 2004 review paper[167], where it is said that "for the first time, one can say that the Nb-based LTS conductors are approaching their limits and that BSCCO and YBCO materials and perhaps MgB_2 are ready to surpass LTS capabilities in higher fields and higher temperature domains, thus opening new markets". The following characteristics are presented as requirements that superconductors should meet for power and magnet technology:

- wires should mechanically resistant to withstand fabrication steps;
- J_c must reach 10^4-10^5 A/cm^2 in magnetic fields from 0.1 to 25 T*;*
- T_c as high as possible.

Because superconductors are used in conditions of large electric currents and/or magnetic fields, it is necessary to insure that these do not cause a transition of the material to its normal conducting state during operation. In practical applications superconductors are cooled to a temperature substantially lower than their T_c, typically to about half of this value. This means that a T_c of about 20 K, as in the case of LTS, refrigeration systems must reach 10 K which can only be achieved by recurring to liquid helium. The superconductor with lowest T_c that can be applied recurring to hydrogen-based refrigeration systems is MgB_2.

Unlike HTS, the performance of MgB_2 is not limited by weak link effects. The critical values are independent of the alignment of the grains in the microstructure. This was first described by Dhalle *et al.*[168] and Kim *et al.*[45] when they observed that the transport measurements of bulk samples resulted in similar J_c values to those obtained through inductive measurements. For this reason it is not necessary to be concerned with texture in polycrystalline samples. In fact, it has been stated by Caplin *et al.* that a reasonable degree of anisotropy is helpful in sustaining J_c in higher field values[159].Fabrication of wires with HTS cores requires expensive silver sheathing, while MgB_2 wires have been presented with relatively inexpensive materials such as copper and iron. Reasonable properties have been obtained for PIT wires even without any heat treatment.

Summarizing, the high critical temperature of 39 K, absence of weak link effects, high critical currents and fields, and relatively low costs of raw materials and fabrication processes, make MgB_2 a promising material for applications with operating ranges above 20 K, the temperature of boiling hydrogen at normal pressure, or attained by recurring to cryocoolers, which do not require helium. These are the reasons behind the technological interest of this material, and the motivation behind the present study.

3 Experimental Methodology

In this chapter the experimental procedures followed in preparing and producing the samples and in characterization studies for this study, will be described.

3.1 Sample Preparation

Polycrystalline bulk samples of MgB_2 were prepared by the conventional solid state reaction following both the *in situ* and the *ex situ* routes.

3.1.1 Ex situ

For the preparation of *ex situ* samples, commercial MgB_2 powder (Alfa Aesar -365 Mesh) was used to make three sets of samples, named A, B and C. Set A is comprised of a single sample, while sets B and C are comprised of four samples each. From now on, samples will be designated by their corresponding set letter and number. As an example, Sample B3 refers to the sample number 3 from set B. The MgB_2 powder was weighed and conformed in a cylindrical mould under uniaxial pressure of 500 MPa. All samples except A1 were wrapped with metallic foil before being inserted into the glass capsule. Set B samples were wrapped in tantalum foil (Goodfellow, 10 μm thickness, 99.9% purity) and set C samples in zirconium foil (Goodfellow, 12,5 μm thickness, 99.5+% purity). The samples were then encapsulated and sealed under vacuum in a pyrex glass tube and magnesium flakes were added to the bottom of capsules of set B and C.

3.1.1.1 Encapsulation step

In order to keep the sample from oxidizing and deteriorating while sintering, the furnace chamber must be kept in vacuum. Still, the volume of the chamber is much larger relatively to the sample volume. The vacuum efficiently is limited and the relative amount of gas molecules remaining inside the chamber will react with the samples, increasing the amount of secondary phases by the end of the processing cycle. Encapsulating the samples under vacuum conditions reduces the amount of atmospheric molecules to

which they are exposed. Several alternatives for the encapsulating material were pondered and glass was considered the most promising: it was relatively easy to work, it is a good pressure transmitting medium and samples were easily recoverable at the end of the process.

Pyrex borosilicate glass 3.3 (chemical composition in Table 3-1) was chosen because of its high melting point (821 °C) and improved thermal shock resistance due to its low expansion coefficient (3.3×10^{-6} K^{-1}).

Table 3-1 – Typical chemical composition of pyrex glass in weight fraction

SiO_2	80.6%
B_2O_3	13.0%
Na_2O	4.0%
AI_2O_3	2.3%

Long tubes of pyrex glass with 13.4 mm of inner diameter and 2 mm wall thickness were used to prepare the capsules. Once cut into smaller sections with roughly 25 cm long, one end of the tube was sealed using a blow-torch. The samples were inserted and pushed into the tube until they reached the closed end. With a diameter of 13 mm adding to the thickness of the metallic wrapping, the samples were tightly fit into the tube. Heating the tube, two constricted areas were made: the first 2 to 2.5 cm above the sample furthest from the closed end; the second 7 to 9 cm away from the first. The first constriction was done at the Glass-Blower's Workshop in the Chemistry Department at the University of Aveiro. It was fundamental that this constriction had the following characteristics:

- length should be between 2 and 2.5 cm;
- the inner diameter should be the smallest possible, without fully closing;
- the wall thickness should be kept between 1 and 2 mm.

The second constriction was not such a demanding task, and required a longer length and thinner wall. The open end of this second constriction was then inserted into a hose connected to two step rotary/molecular vacuum pump and evacuated. The closed end was inserted into a heated tube furnace to help the vacuum process and removing any humidity left inside the capsule. The exact preparation parameters used for the three sets are discriminated in Table 3-2. At the end of this step, the closed end was taken from inside the furnace, and a blow torch was used to heat the glass at the first constriction leaving the pump running. Once the glass was softened and vacuum made it collapse, the closed end of the tube was pulled and the blow torch used to finish sealing the capsule.

Table 3-2 – Encapsulation parameters used for *ex situ* samples.

Sample Set	A	B	C
Temperature	160 °C	200 °C	200 °C
Time	3 hours	1 hour	2 hours
Internal Pressure	10^{-2} mbar	10^{-2} mbar	10^{-5} mbar
Sample wrapping	no	Ta	Zr

Once the capsules were prepared they were placed in a graphite crucible filled with graphite powder to prevent glass flow once they reach high temperatures. Sintering was performed in a Hot Isostatic Press (HIP) (Vitek HIP/GPS system) which can be seen in Figure 3-1. Each capsule was sintered under different conditions of temperature and pressure. In all there was a first hold step at 700 °C where the glass is already softened and pressure could be increased until it reaches the desire value, minimizing the possibility of cracking. Sintering conditions are discriminated below for each sample set. Samples were recovered after the processing cycle by breaking the glass capsules.

Figure 3-1 – Hot Isostatic Press used for *ex situ* sample sintering at the Ceramic and Glass Department.

3.1.1.2 Set A

Sample A1 was heated at a rate of 20 °C/min until 700 °C and held until pressure reached 50 MPa (~500 bar). Heating was then resumed and sintering occurred at 950 °C for 2 hours. Figure 3-2 shows a representation of the pressure/temperature cycle.

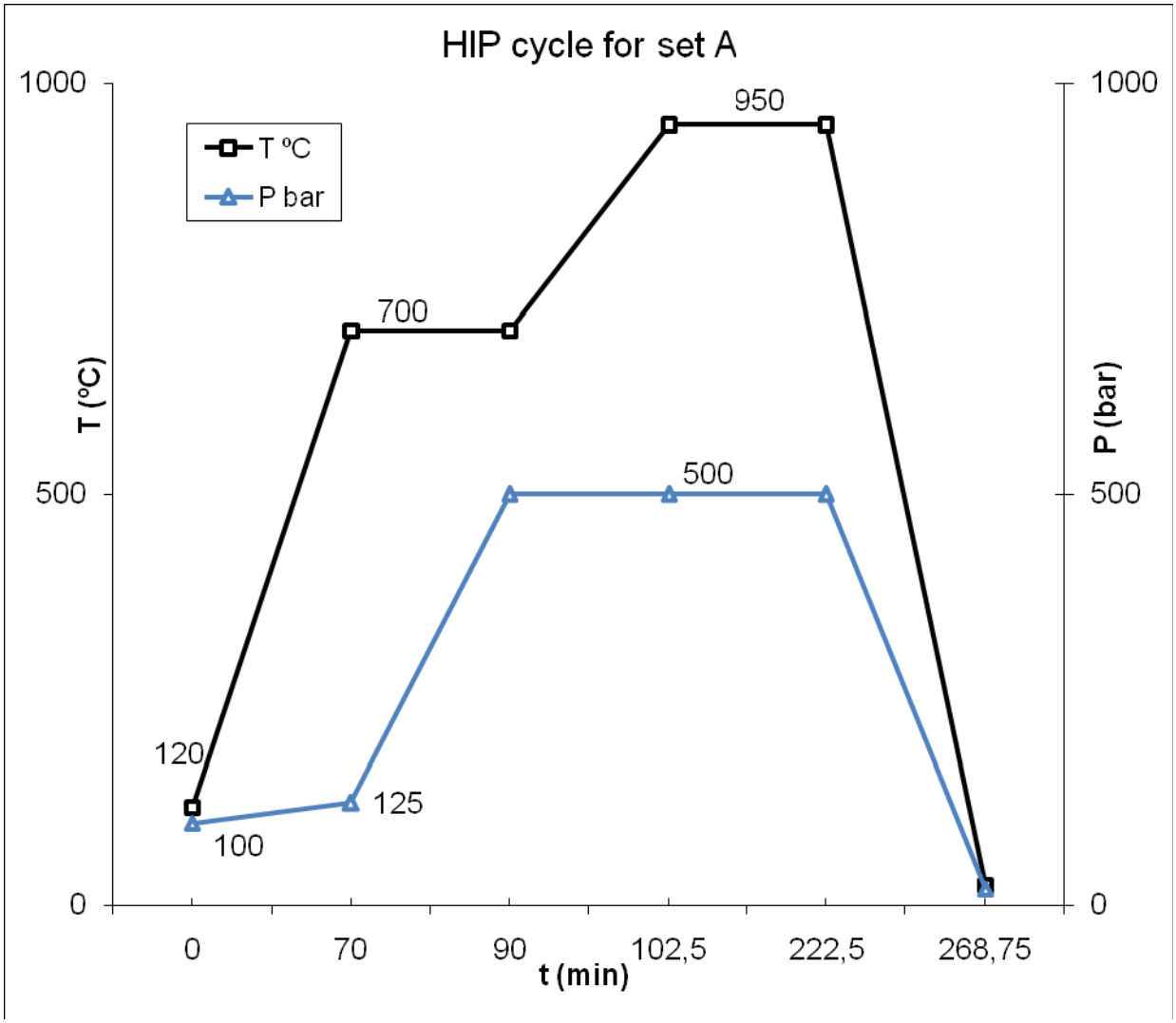

Figure 3-2 – Temperature/pressure cycle used in processing sample A1.

3.1.1.3 Set B

Four samples were prepared in this cycle. They were heated at a rate of 20 °C/min until 700 °C and held until pressure reached ~30 MPa. Heating was then resumed and sintering occurred at 950 °C for 3 hours. Figure 3-3 shows a representation of this cycle.

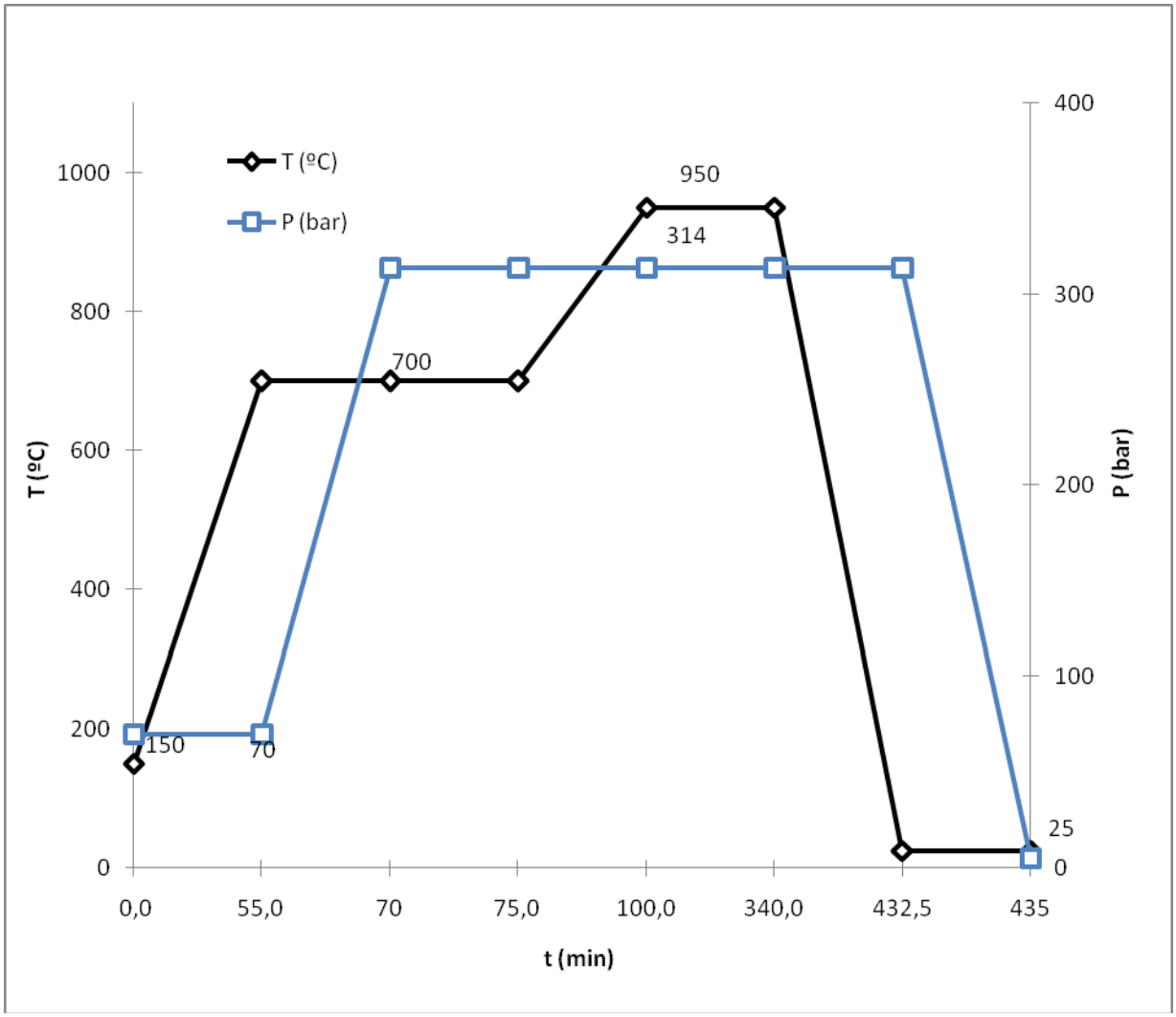

Figure 3-3 – Temperature/pressure cycle used in processing samples from set B.

3.1.1.4 Set C

Four samples were prepared in this cycle. They were heated at a rate of 20 °C/min until 700 °C and held until pressure reached a maximum of 190 MPa. Heating was then resumed and sintering occurred at 950°C for ~1,5 hours. Pressure was not maintained constant due to equipment malfunction, which caused pressure to oscillate between 190 MPa and 145 MPa. Figure 3-4 shows a representation of this cycle.

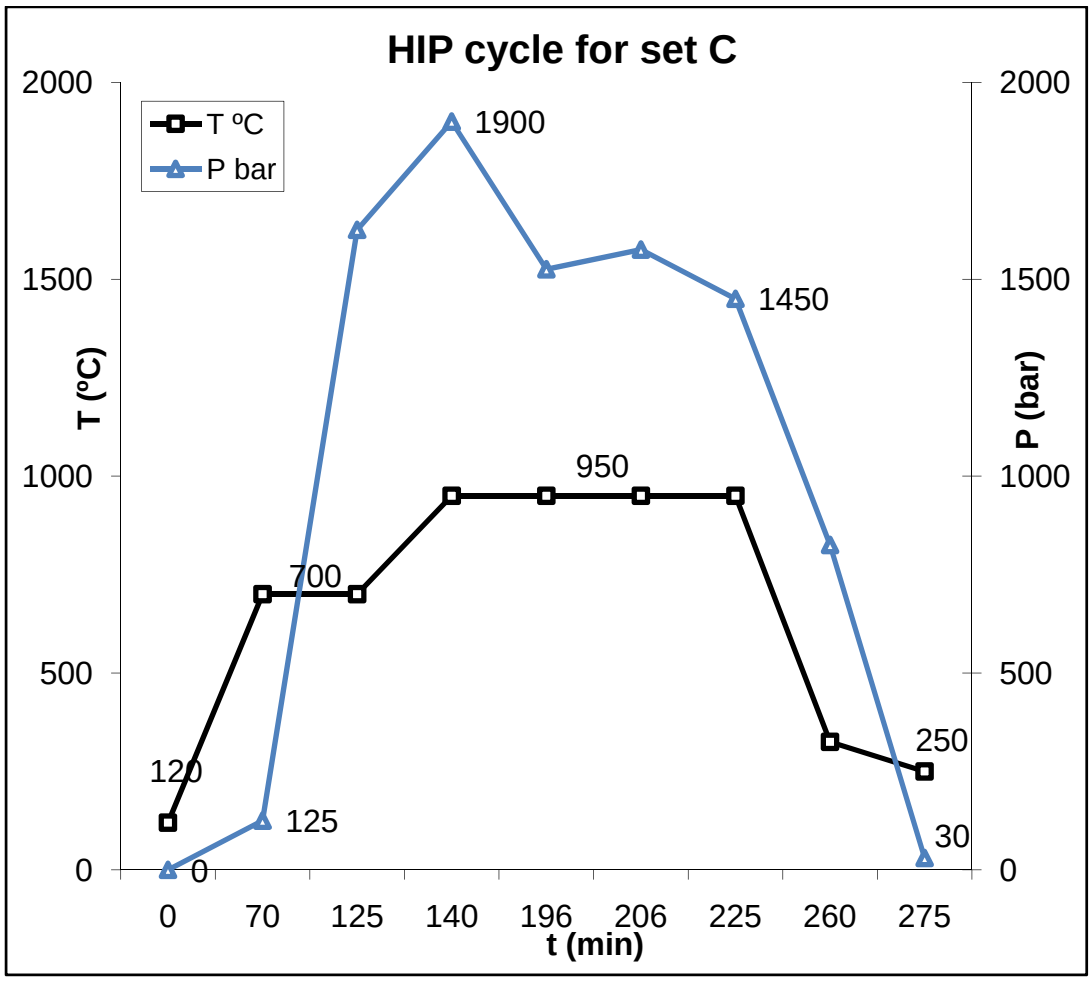

Figure 3-4 – Temperature/pressure cycle used in processing samples from set C.

3.1.2 In situ

In situ samples were prepared using magnesium powder (Alfa Aesar -325 Mesh, 99.8% purity) and boron powder (ABCR amorphous < 1μm, 99% purity). Powders were weighed separately and mixed by hand in the following Mg : B molar ratios: 1 : 2; 1,2 : 2 and 1,5 : 2. These compositions were designated by A, B and C, respectively. Each sample was then pressed into pellets, individually wrapped in zirconium foil and encapsulated in the same way described for the *ex situ* samples. The capsules were then heated to 110°C and sealed under vacuum of 10^{-2} mbar. Samples were sintered under vacuum inside a graphite furnace (Thermal Technology Inc). Pressure inside the chamber reached 2,5 x 10^{-1} mbar at 100 °C and was maintained for 30 minutes. Furnace was then heated at 20 °C/min until it reached 700 °C and was maintained for 1 hour. Cooling occurred at 20 °C/min until room temperature. The samples were recovered by breaking the glass capsules.

3.2 Sample Characterization

This chapter lists all the procedures used for the characterization of raw materials and finished samples.

3.2.1 Raw materials

Initial powders used for sample processing were characterized as to particle size distribution, phase composition and chemical composition.

3.2.2 Particle size distribution

Initial particle size distribution for the commercial MgB_2 powder used in *ex situ* sample processing was determined by laser diffraction. In this analysis, an aqueous suspension of MgB_2 powder dispersed with dispex was prepared and analysed using a Coulter LS230 system. The powders were later observed using scanning electron microscopy (SEM).

3.2.3 Phase composition and morphology analysis

X-ray diffraction (Rigaku – Diffractometer system "Geigerflex" D\max – C series), Hitachi S4100 field-emission scanning electron microscope (SEM) coupled with energy dispersive spectroscopy (EDS) were used to carry out these phase composition and morphological analysis.

3.2.3.1 X-ray diffraction and Rietveld method

X-ray diffraction technique was used to determine the qualitative phase composition of the initial powders and processed samples. Once the diffraction patterns were obtained, a semi-quantitative determination of the detected phases was made, recurring to Rietveld method. This analysis gives a relative abundance measure (weight fraction, *wt.%*) of the phases identified in the diffraction pattern. Determining the relative amounts of each phase is considered to be quantitative analysis. Semi-quantitative analyses are those in which the results yield some measure of the quantity of phases using a somewhat subjective assessment of the data, or a method that does not allow its accuracy to be determined. The difference between semi-quantitative and quantitative analysis is the degree of uncertainty in the results obtained. However when comparing results obtained via the same approach, although accuracy may be compromised, one usually assures precision.

There are different methods used to determine relative phase composition. In this work the Rietveld refinement method was used[169]. The Rietveld method is based on a refinement technique and therefore, a starting point is necessary. The objective is to refine all parameters which determine the structure of the diffracting phases. A special requirement is that any instrumental and sample factors that affect the diffraction behaviour have to be correctly specified. The objective is then to obtain a theoretical diffraction pattern which best fits into the one obtained experimental experimentally. This process is referred to as profile fitting. The chance of success is increased with an experimental pattern of good quality and the availability of structural data, which can then be modified as the profile fitting is done. In this work FullProf software[170] was used for profile fitting. This is an iterative method in which small changes in the parameters are implemented and then the software calculates the resulting theoretical pattern based on these parameters. At the end of each iteration, both diffraction patterns are overlapped and displayed on screen, so that the user can make an evaluation of the fitting. As a measure of the fitting accuracy a parameter, chi^2 or χ^2, is calculated and presented by the software during every step of the iteration. The closest it gets to zero, the better the fitting. In the resulting output file, the phase relative phase composition is presented as weight ratios. Some advantages of this method are presented in the following list:

- All the peaks in the pattern play a part in the analysis.
- The use of a continuous fitting function provides a much improved background fit.
- The effects of preferred orientation and extinction are reduced.
- Crystal structure and peak profile parameters can be refined in several stages, thus it is easier to refine peak widths, peak asymmetry, peak shape and instrument zero.

3.2.3.2 SEM

SEM provides fundamental information about a given material's microstructure through a combination of high resolution, relatively simple sample preparation procedure, ease in interpreting the images, together with the possibility to realize localized elemental analysis and semi-quantification recurring to EDS. MgB_2 powders were observed using SEM to analyse general particle morphology, namely their shape and size. EDS was used to probe local chemical composition. The powders were mixed in ethanol in a dilute suspension. A drop was placed on top of an aluminium sample holder. After drying the powders were inserted into the SEM specimen chamber and analysed.

3.2.4 Bulk Samples

The processed samples were characterized as to their density, chemical phase composition and microstructure. For each experiment, a different piece of each sample was cut and analysed.

3.2.4.1 Density Measurements

Initial (green) and final density of the samples was determined for every HIP processing cycle. Two different methods were used: geometrical for green and final sample densities; through immersion or Archimedes technique for a second assessment of final sample density. In the latter a small piece of the HIPed sample was cut and weighed in air, yielding m_0 Then they were immersed in diethylphtalate oil and slightly heated for some minutes to saturate any open porosity. After being cooled to ambient temperature, they were weighed while immersed in the oil, yielding m_1 After they were taken from the oil and their surface wiped with a clean cloth, a third and final weighing in air was done, yielding m_2 The sample's experimental density was determined using Equation 3-1.

$$\rho_{exp} = \frac{m_0}{m_1 - m_2} \times \rho_{oil} \qquad \text{Equation 3-1}$$

where ρ_{oil} = 1.118 g/cm^3.

Densification of a sample is commonly determined through its relative density, which is obtained dividing its experimental density by the theoretical density of the material it is made of. When the sample is not composed of a single phase, one must take into account its relative composition and corresponding theoretical densities of all phases. To attain a more accurate theoretical density value, ρ_t,for a sample with *n* phases, the following equation was used:

$$\rho_t = \frac{1}{\sum_{i=1}^{n} f_i / \rho_i} \qquad \text{Equation 3-2}$$

where f_i is the weight fraction of phase *i*, and ρ_i its corresponding theoretical value.

3.2.4.2 X-ray Diffraction

Two types of XRD analysis were performed on bulk samples: broad and small-angle, otherwise known as grazing incident angle XRD. The former is the most common type to access phase composition in bulk or powdered samples to a certain depth of the sample surface, depending on the test conditions and sample compositions. Low-angle XRD is used when information about the composition of the phases closer to the surface of the sample is required. It is very commonly used for thin films, since they have low diffraction volumes. The difference between both techniques is depicted in Figure 3-5.

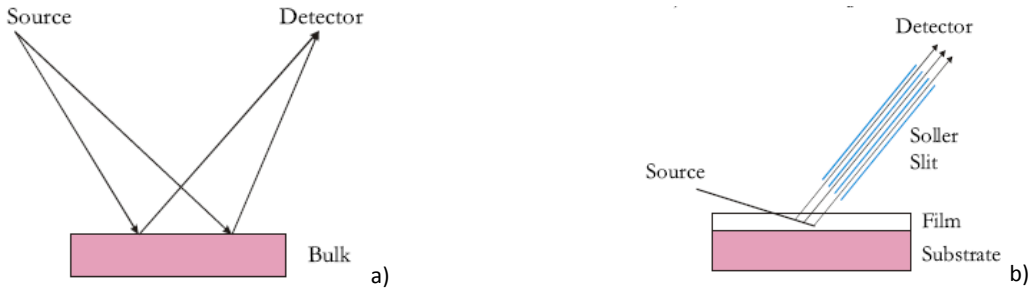

Figure 3-5 – Differences between broad and small-angle XRD: a) conventional geometry for broad angle XRD; b) small-angle XRD[171].

In broad-angle technique, the incident beam is broader and irradiates a larger volume of the sample simultaneously at different angles. The angle range can be setup for each measure, but typical values range from 5° to 90°. The detector is movable and it rotates over to the opposite side of the sample as it

gathers diffracted beam information. In the case of low-angle technique, the incident beam hits the sample at a lower angle, thus increasing the X-ray beam path at the surface, and retrieving more information on its composition. In this configuration, the incidence angle is maintained fixed while the detector rotates through the angular range collecting the resulting data. There is no special preparation required for the experiment, apart from exposing the correct sample surface one wishes to analyse.

3.2.4.3 SEM / EDS

In order to observe the processed sample's microstructure each pellet was cut in half. One of the halves' exposed surface was polished using diamond coated films with decreasing grain sizes, of 30 μm, 15 μm, 3 μm and 1 μm. The polished surface of some of the samples was cleansed by immersion in HCl 0.1 N solution for 10 seconds. This procedure will be noted whenever applicable. The samples were then glued to a sample holder using carbon glue. With the inner surface exposed, it was possible to observe any microstructural differences and porosity along the cross section of the sample. Local chemical analysis was performed on specific areas of the sample using EDS.

3.2.4.4 TEM / EDS

Transmition electron microscope (Hitachi S9000) coupled with EDS was used to study two representative samples with the intent of further characterizing the sample's microstructure, analysing the dispersion of MgO grains on the microstructure and study the chemical composition along the grain boundaries. TEM samples were prepared by polishing a small piece of HIPed MgB_2 in diamond coated films with decreasing grain sizes until sample thickness reached ~70μm, followed by ion milling until perforation. Because samples have shown signs of surface alteration upon air exposure, great care was taken to avoid such problems. Sample C7, which was the first one prepared for TEM observation, was kept inside the ion milling vacuum chamber until the observation date, but still showed sign of surface contamination, obvious in the micrographs taken. Sample B3 was removed from the ion miller after polishing, kept under ambient conditions for 2 days and was ion milled again for 20 minutes just before TEM observation. This sample showed no signs of such surface alterations during its observation.

4 Experimental Results

In this chapter experimental measurements and characterization results will be presented in detail for the starting MgB_2 powders, the three sets of HIPed samples that followed the *ex-situ* processing route, and the *in-situ* samples sintered in the graphite furnace under vacuum. Although there are some important remarks to take into consideration for a full analysis of these results, in the current chapter only results and immediate conclusions will be presented. Their discussion will be reserved to the following chapter.

4.1 Starting MgB_2 Powders

4.1.1 Crystalline phase composition

A theoretical XRD pattern was calculated using crystallographic data presented on section 2.2 and plotted using Carine Crystallography software and is presented in Figure 4-1. This can be compared with the experimental x-ray diffraction pattern in Figure 4-2, where it is visible that besides MgB_2 (95% wt.) a second phase corresponding to MgO (5% wt.) is already present. The weight fraction of the two phases was obtained by profile fitting using Rietveld analysis (Figure 4-3).

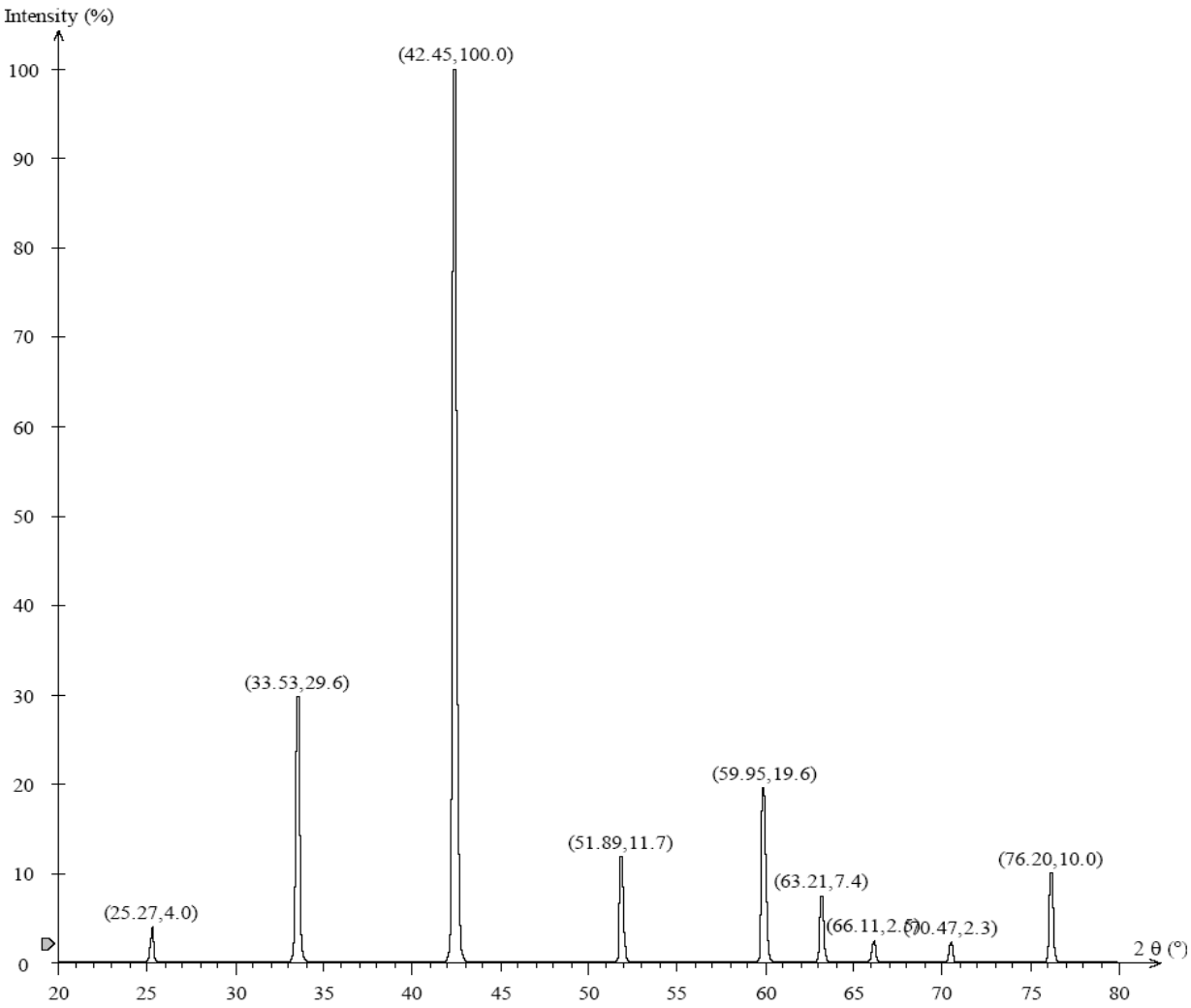

Figure 4-1 – Theoretical X-ray diffraction pattern for MgB_2 as obtained using Carine software.

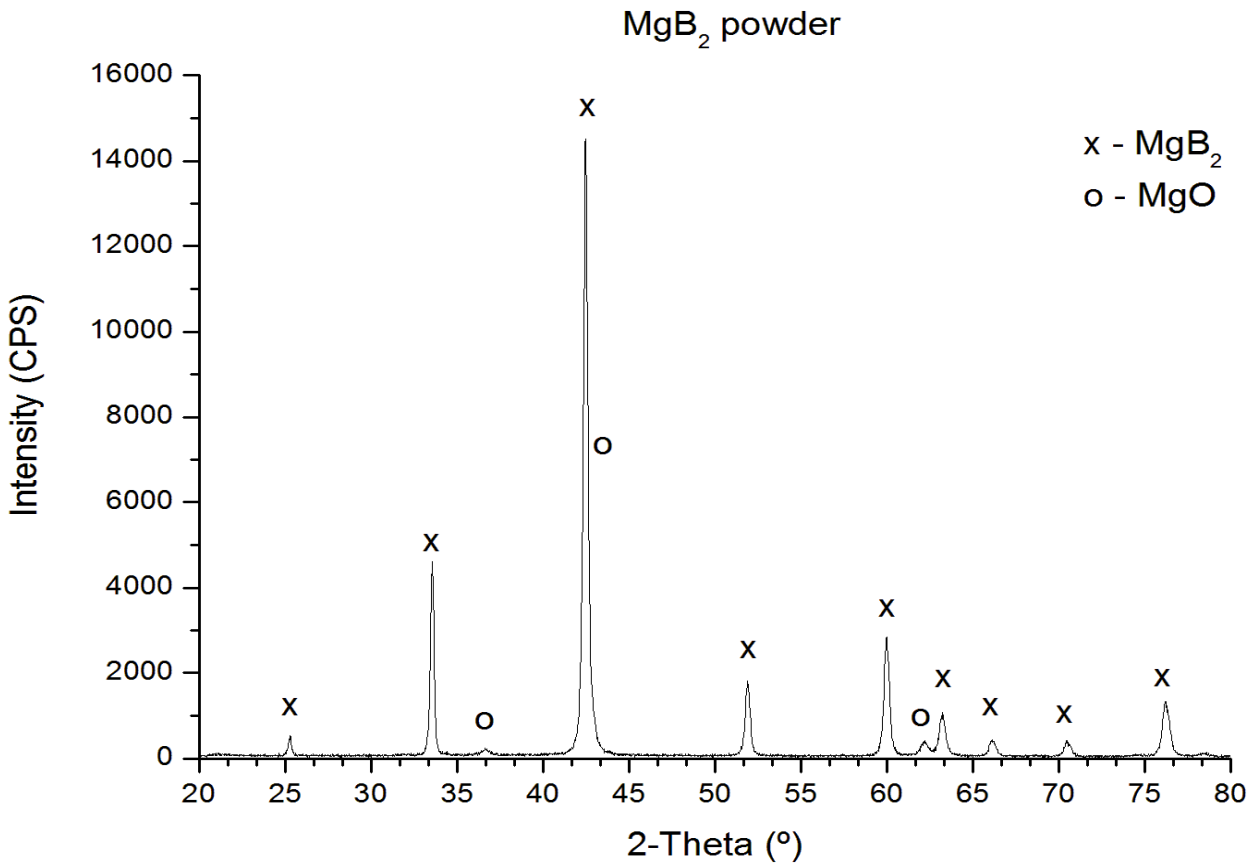

Figure 4-2 - Shows the experimental diffraction pattern of the starting MgB_2 powders.

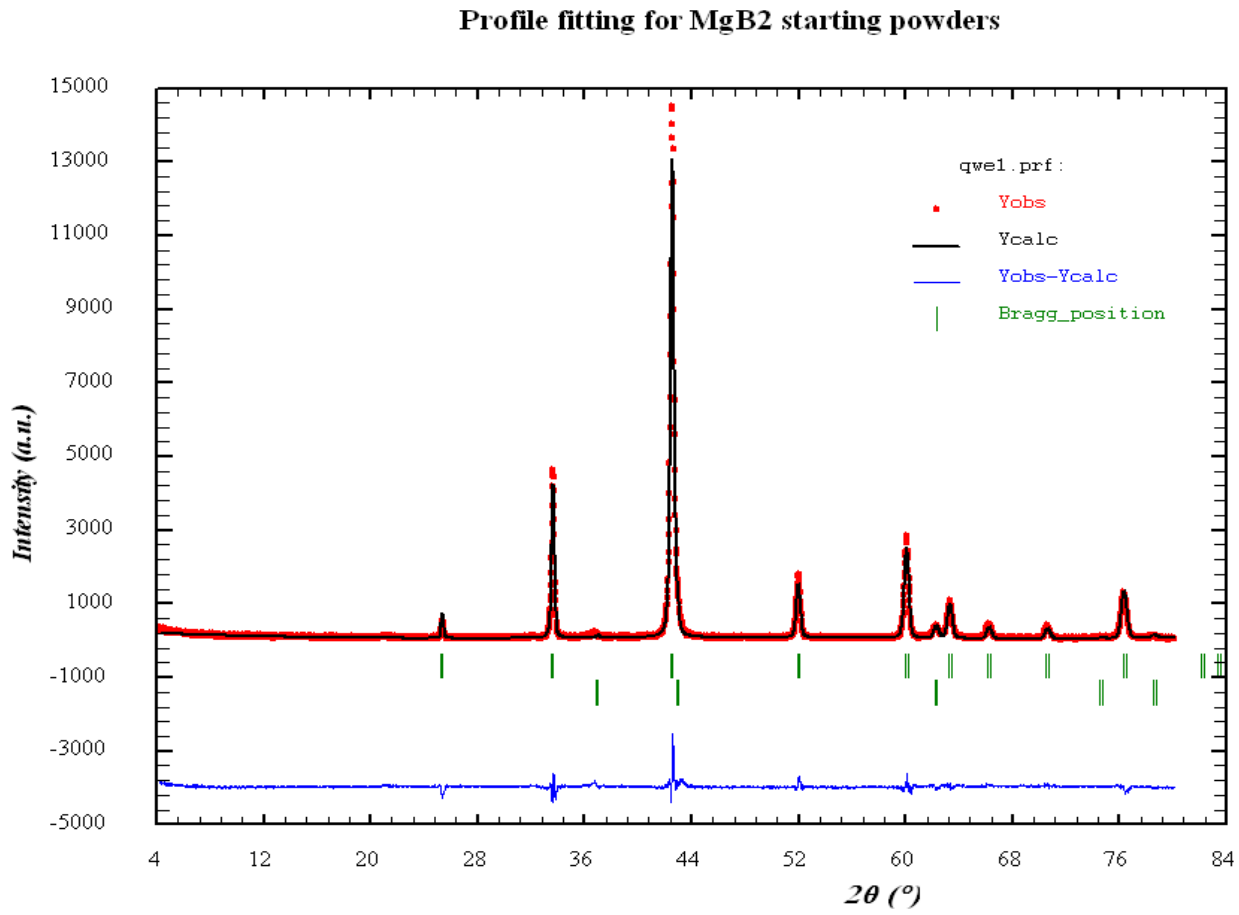

Figure 4-3 - Profile fitting as determined by Rietveld refinement, for the starting MgB_2 powders. On the caption *Yobs* refers to the experimental data points (in red), *Ycalc* the refined peaks (in black), *Yobs-Ycalc* is the difference between theoretical and experimental data points (in blue, at the bottom), and *Bragg_position* the diffracting angles for both phases (in green: top – MgB_2, bottom – MgO).

4.1.2 Particle Morphology

Laser diffraction performed on initial powders shows a bi-modal log-normal distribution of particle size with peaks centred on 0.4 μm and 3 μm (Figure 4-4).

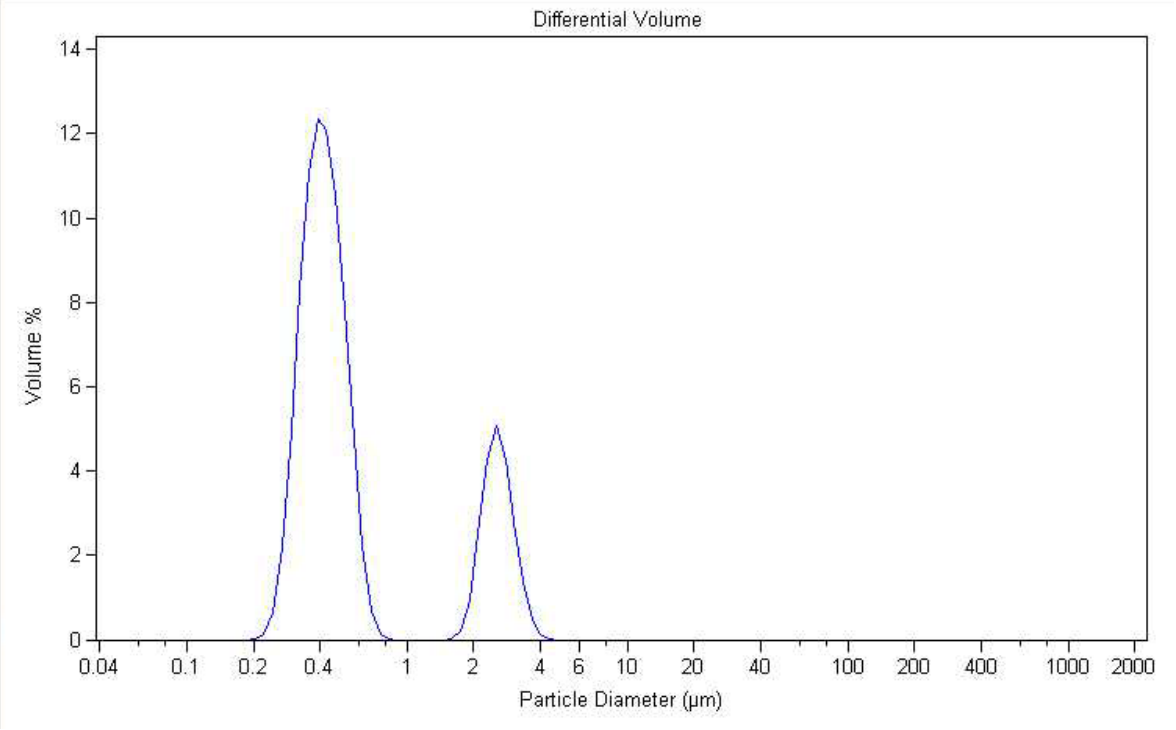

Figure 4-4 – Differential volume distribution of the MgB_2 powder obtained by laser diffraction technique.

The average particle size is 0.903 µm. The particle size distribution in percentage is presented in Table 4-1.

Table 4-1 – Particle size distribution for MgB_2 powder.

Vol. % particles with sizes lower than	**10**	**25**	**50**	**75**	**90**
Particle size (µm)	0.319	0.368	0.446	0.601	2.615

Observation of the powders in SEM confirms the previous particle size values. Figure 4-5 shows a micrograph of the powers comprised of particles as small as 1 µm and others as big as 15 µm. A closer look (Figure 4-6) reveals that these particles consist in physically connected agglomerates of smaller plate-shaped particles.

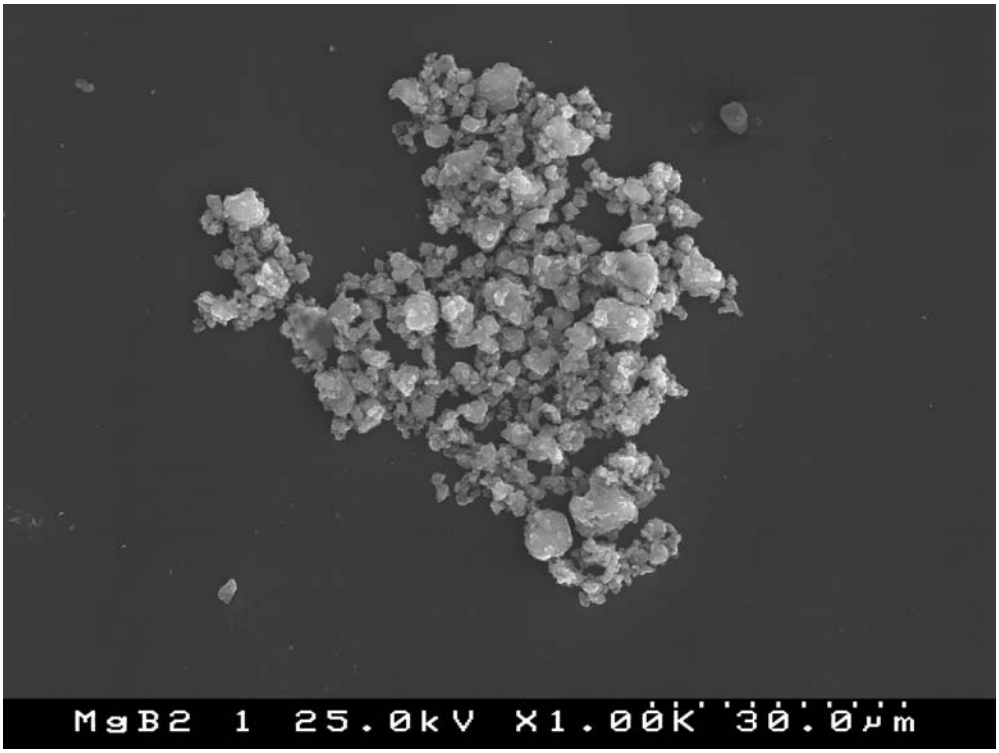

Figure 4-5 – SEM micrograph of MgB_2 powders (1000x magnification).

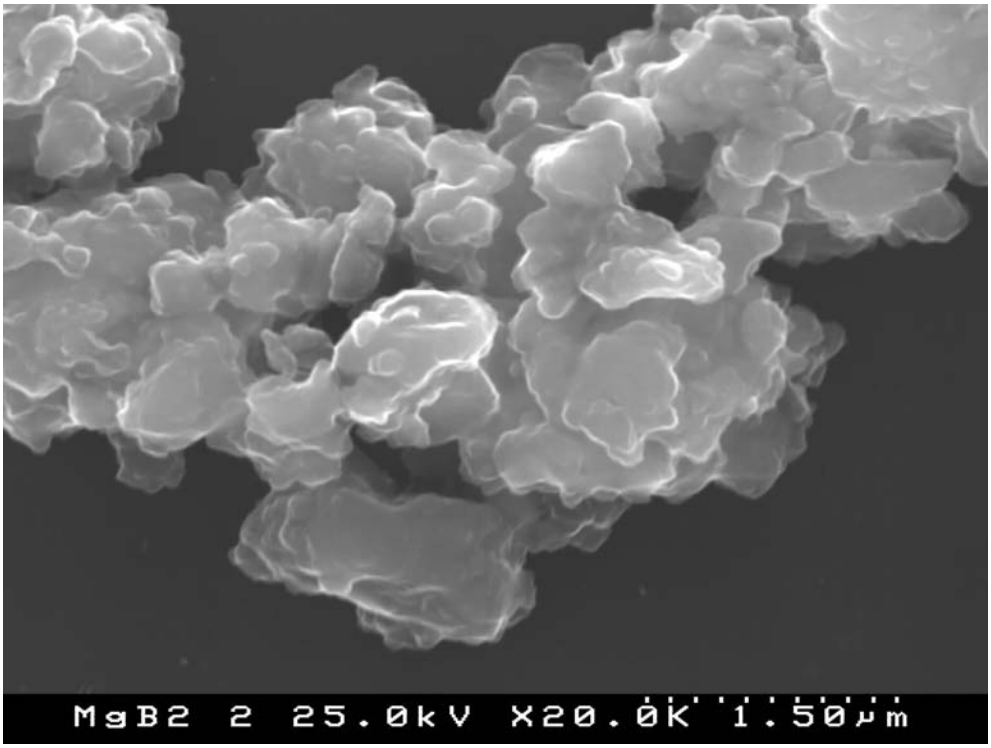

Figure 4-6 – SEM micrograph of the same powders (magnification 20000x).

4.2 Ex situ Samples

Ex situ samples were HIPed under different conditions of pressure and time while temperature was maintained constant. In Table 4-2 an overview of the processing conditions for all three sets is resumed. Detailed parameters for the processing cycles can be found in the previous chapter.

Table 4-2 – Summary of the sintering conditions for HIPed samples.

Sample	T (°C)	P (MPa)	t (hour)
A1	950	50	2
B2 - 5	950	30	3
C6 - 10	950	150	1.5

4.2.1 Set A

Table 4-3 shows the dimensions of A1 sample (both green and HIPed) used to determine experimental densities, which were obtained from their geometry. As this was the first sample to be processed, its main purpose being to test the capsule and the HIP apparatus, data collected was not very detailed. The dimensions presented for the HIPed sample correspond to a fraction of the whole sample because some glass from the capsule had collapsed and adhered to the sample's surface. To remove it, the sample was polished using diamond abrasive film.

Table 4-3 – Geometrical and relative density values for green and HIPed sample A1.

A1	m (g)	d (cm)	h (cm)	ρ_g (g/cm^3)	ρ_r (%)
Green	1.55	1.310	0.665	1.73	66
HIPed	0.89	1.080	0.450	2.16	82

caption:

m – sample's weight

d – sample's diameter

h – sample's height

ρ_g – experimental density

ρ_r – relative density

Figure 4-7 shows the XRD pattern obtained for sample A1, where three crystalline phases were identified: MgB_2, MgO and MgB_4.

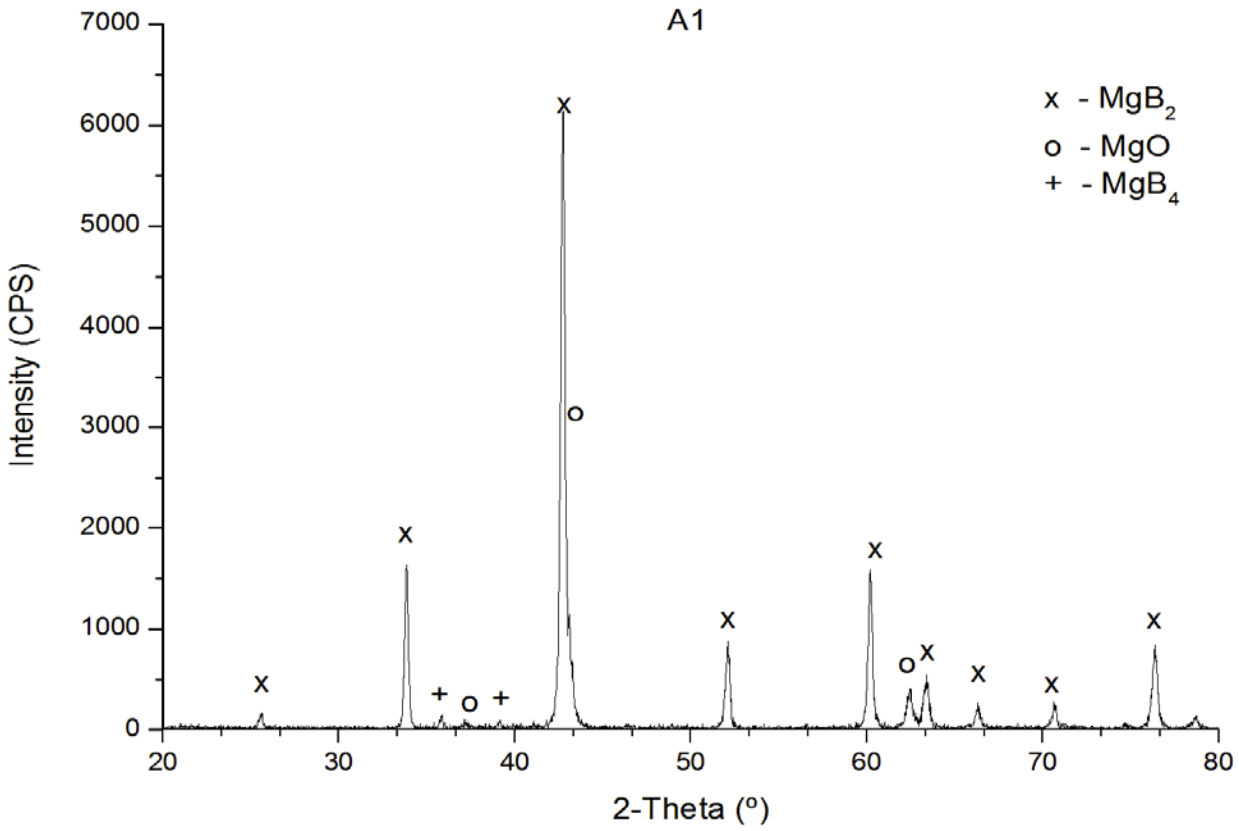

Figure 4-7 – Diffraction pattern for sample A1 revealing the presence of a third phase, MgB_4, which was formed during sintering.

Table 4-4 presents the results for the density values and phase composition determined for sample A1. The theoretical density was determined taking into account the relative phase composition as determined by XRD and Rietveld analysis, using Equation 3-2.

Table 4-4 – Phase composition and corrected density values for sample A1.

Sample A1	ρ_{exp} (g/cm^3)	Phase composition (wt. %)			ρ_t (g/cm^3)	ρ_r (%)	Π (%)
		MgB_2	MgO	MgB_4			
Green	1.729	95	5	0	2.625	66	34
HIPed	2.159	75	17	8	2.738	88	12

caption:

ρ_{exp} – experimental density

ρ_t – theoretical density

ρ_{MgO} – 3.580 g/cm^3

ρ_{MgB4} – 2.482 g/cm^3

ρ_r – relative density

Π – porosity

4.2.2 Set B

Table 4-5 summarizes the results obtained for Set B samples in green and after being HIPed, where the relative density values were calculated using the theoretical density value for MgB_2.

Table 4-5 – Results of green and after processing of samples of Set B.

		B2	B3	B4	B5
weight (g)	m_0	1.946	1.911	1.924	1.908
	m_f	1.823	1.793	1.794	1.896
	Δm (%)	-6.3	-6.2	-6.8	-0.6
diameter (cm)	d_0	1.310	1.310	1.310	1.310
	d_f	1.185	1.170	1.180	1.235
	Δd (%)	9.5	10.7	9.9	5.7
density (%)	ρ_{r0}	68	68	69	67
	ρ_{rf}	89	88	88	80

Caption:

m_0 – green sample mass

m_f – HIPed sample mass

Δm – weight variation, calculated using Equation 4-1

d_0 – green sample diameter

d_f – HIPed sample diameter

Δd – linear retraction, calculated using Equation 4-2

ρ_{r0} – green sample's relative density

ρ_{rf} – HIPed sample's relative density

$$\Delta m = \frac{m_f - m_0}{m_f} \times 100 \qquad \text{Equation 4-1}$$

$$\Delta d = \frac{d_0 - d_f}{d_f} \times 100 \qquad \text{Equation 4-2}$$

Phase composition was determined by XRD on all samples and semi-quantification was calculated by Rietveld analysis. A typical XRD with the refinement pattern already included can be seen in Figure 4-8, where the MgB_4 phase subsides.

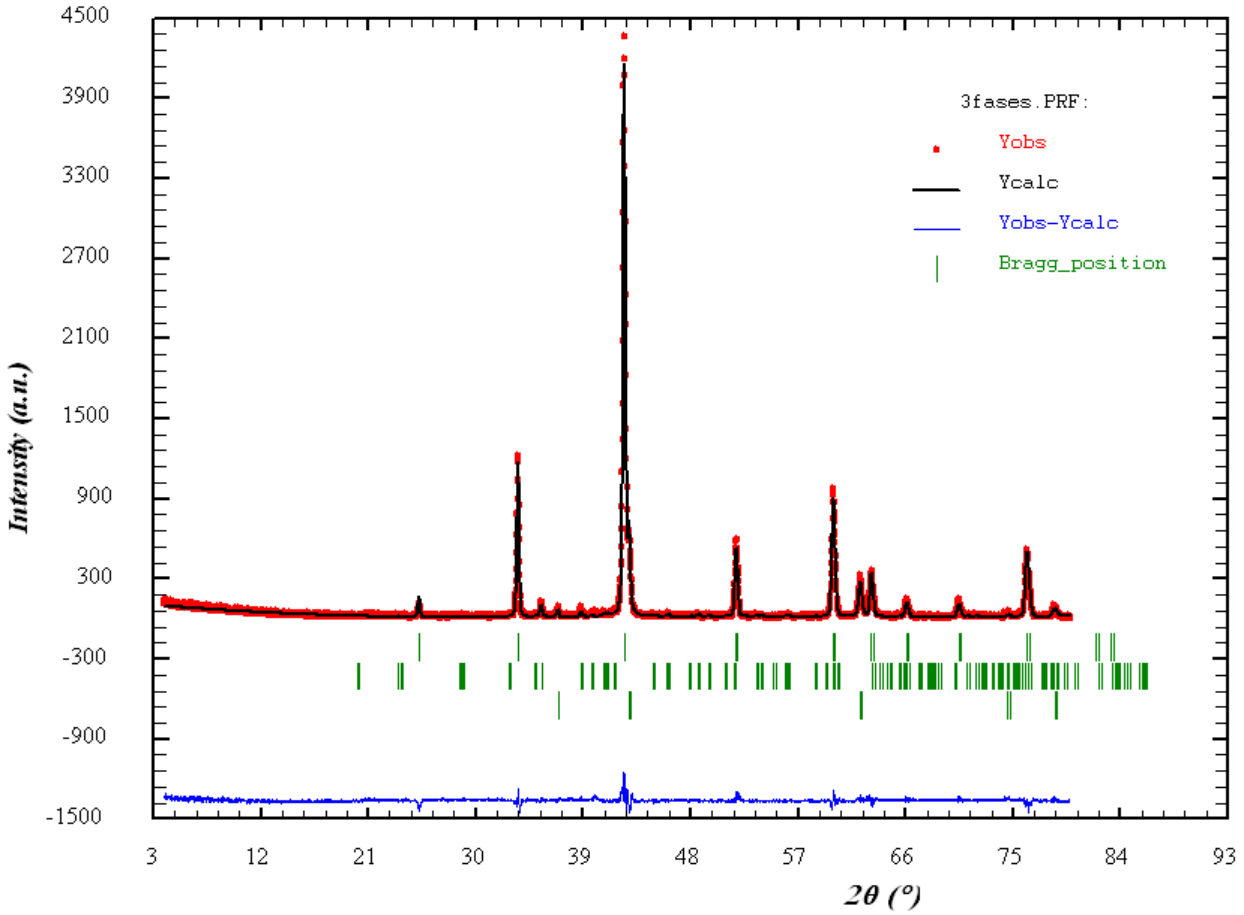

Figure 4-8 – XRD and profile fitting patterns for the sample B4. In caption, Yobs refers to the experimental data points (in red), Ycalc the refined peaks (in black), Yobs-Ycalc is the difference between theoretical and experimental data points (in blue, at the bottom), and Bragg_position the diffracting angles for both phases (in green: top – MgB_2, middle – MgB_4, bottom – MgO).

The density of the samples was measured again, this time using the Arquimedes method, and the relative weight fractions of the phases were obtained from the Rietveld analysis. These were used to correct the relative density values and porosity of the samples, taking into account the densities of MgO and MgB_4. The results are presented next in Table 4-6.

Table 4-6 – Phase quantification and corrected relative density values for set B samples.

SET B	Phase composition (weight %)			ρ_t	ρ_{exp}	ρ_r	Π
	MgB_2	MgO	MgB_4	(g/cm^3)	(g/cm^3)	(%)	(%)
B2	84	12	4	2.707	2.407	89	11
B3	80	12	8	2.704	2.366	88	12
B4	81	13	6	2.709	2.390	88	12
B5	78	14	8	2.715	2.450	90	10

Caption:

ρ_t – theoretical density

ρ_{exp} – experimental density

ρ_r – relative density = ρ_{exp}/ρ_t

Π – Porosity

All samples were prepared and observed in SEM. The collected images are presented in the following table. In a general way, the microstructures are heterogeneous both in terms of grain size distribution and inter-grain connectivity. Grain boundaries are not totally distinguishable, but tilting the sample between 30°-40° provides some visual enhancement.

Table 4-7 – Compilation of SEM images showing the microstructure of set B samples.

Overview images at low magnifications.	Microstructural details at high magnification and sample tilting (35°).
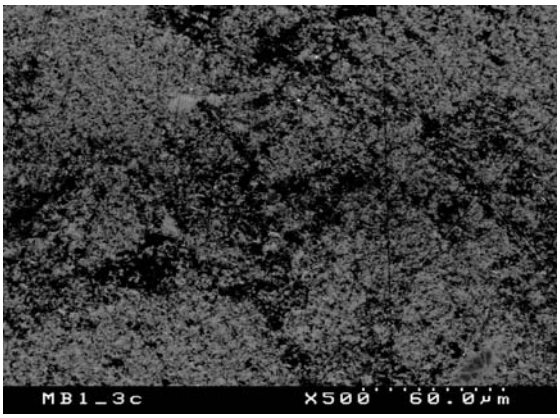	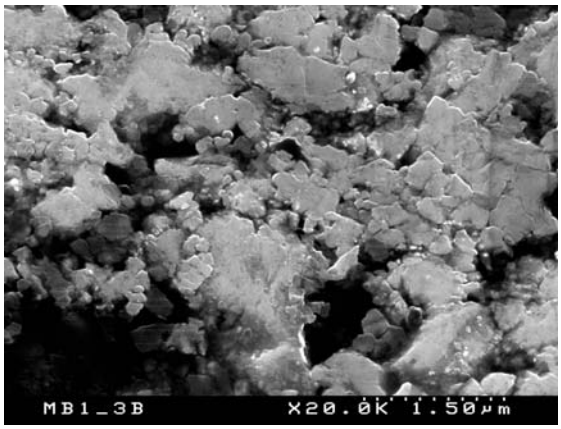
a)	b)

Figure 4-9 – Microstructure of sample B2: a) 500x magnified; b) 20000x magnified.

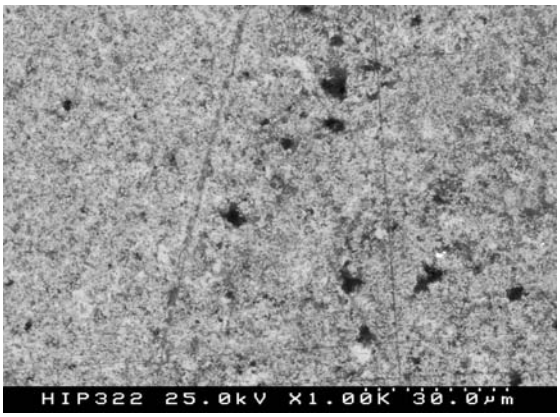

a)

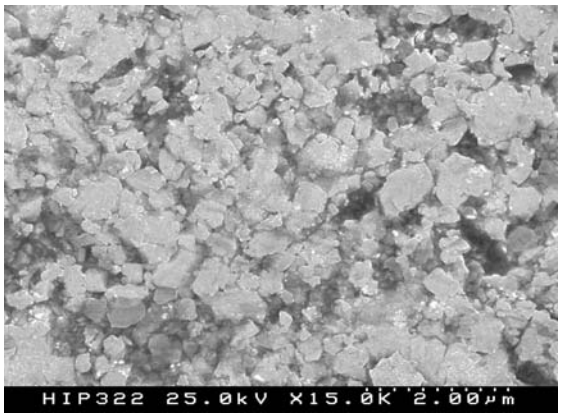

b)

Figure 4-10 – Microstructure of sample B3: a) 1000x magnified; b) 15000x magnified.

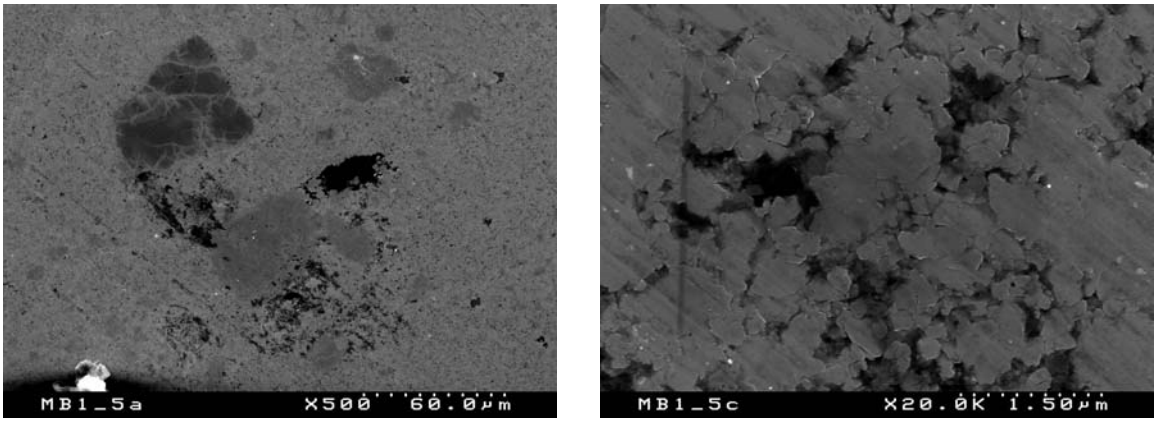

a) b)

Figure 4-11 – Microstructure of sample B4: a) 500x magnified; b) 20000x magnified.

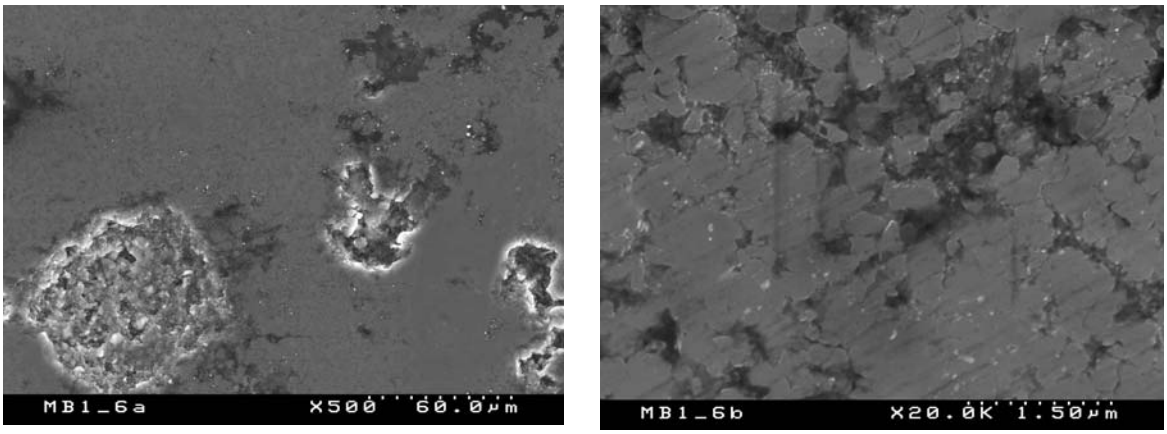

a) b)

Figure 4-12 – Microstructure of sample B5: a) 500x magnified; b) 20000x magnified.

EDS was performed on every sample. Sample B3 is presented here as an example because it was possible to capture typical microstructural features in a single image (Figure 4-13). The areas where EDS was performed are indicated in the picture and the corresponding results can be seen below.

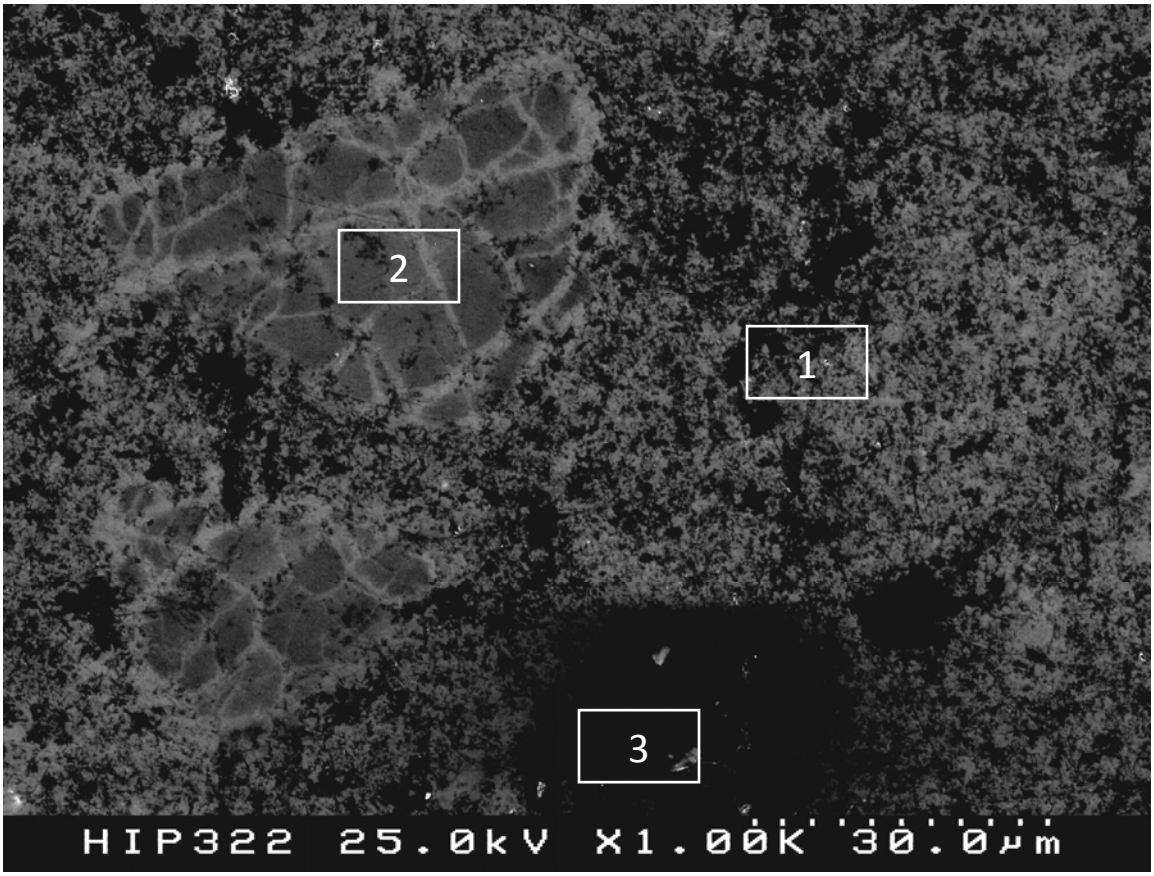

Figure 4-13 – SEM image showing some microstructural features of sample B3, which are more or less common to every sample. The rectangles indicate the 3 separate zones where EDS analysis was performed (magnification 1000x).

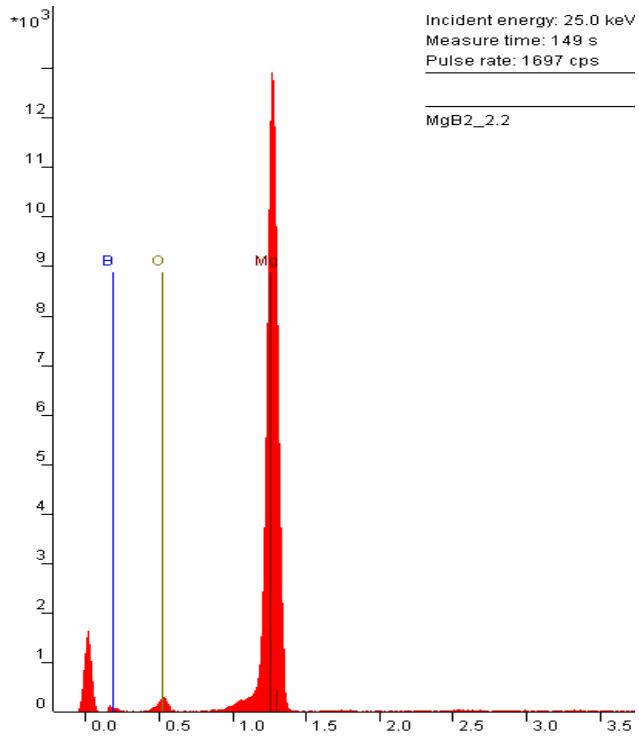

Figure 4-14 – EDS spectrum resulting from zone 1.

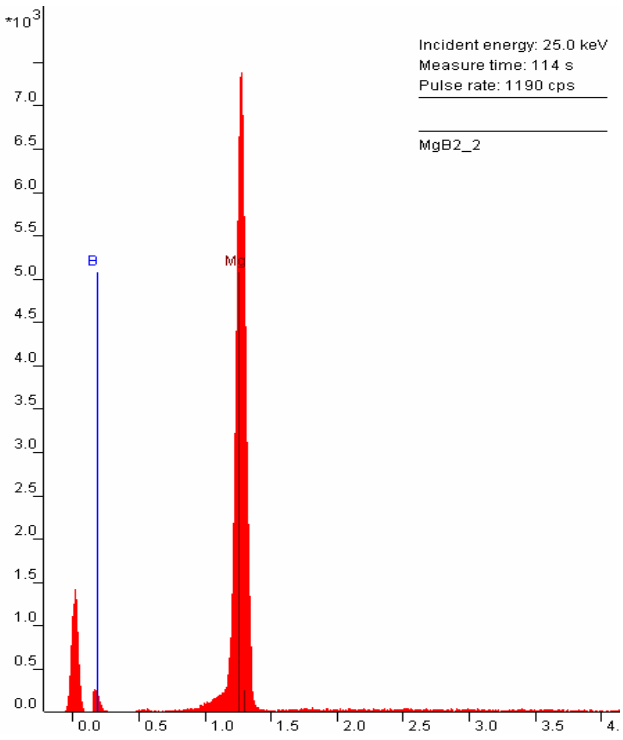

Figure 4-15 –EDS spectrum resulting from zone 2.

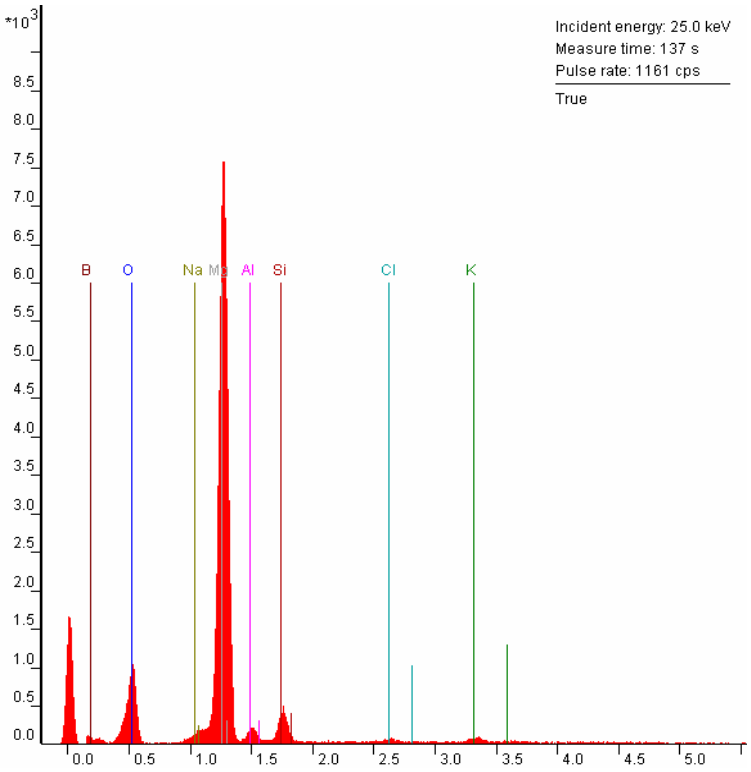

Figure 4-16 – EDS spectrum resulting from zone 4.

From the EDS analysis it is possible to know the elemental composition in specific areas of the sample. EDS made in zone 1 indicated the presence of boron and magnesium as the only detectable elements, while in zone 2 which had darker areas, a peak corresponding to oxygen is visible. Zone 3 is a depression on the sample surface and several extra elements, such as sodium, silicon, potassium, chlorine and aluminium were detected. More than likely these are impurities were introduced during sample preparation that was not properly eliminated.

Sample B3 was also prepared and taken for TEM observation. The resulting micrographs and EDS analysis are presented next. EDS showed that this microstructure consists of a matrix of grains with an Mg-B-based composition, and small MgO precipitates with sizes ranging from 20 to 100 nm (Figure 4-17 and Figure 4-18).

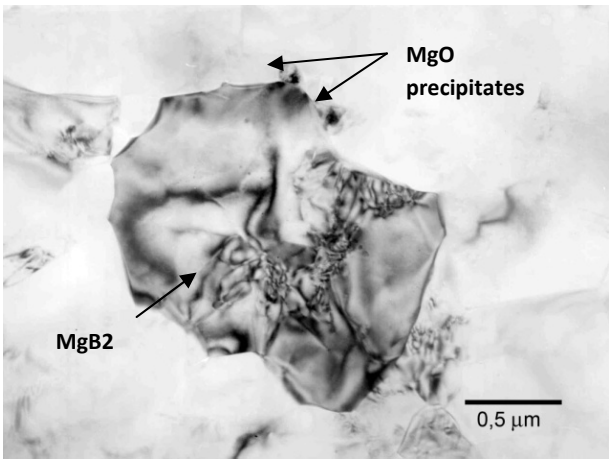

Figure 4-17 – Micrograph of an MgB_x grain (~3µm in size) and MgO precipitates on its grain boundary.

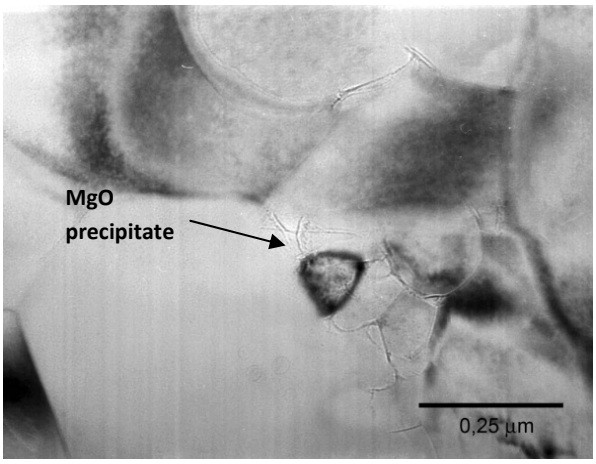

Figure 4-18 – Micrograph of an MgO precipitate on a triple point with ~80 nm in size.

EDS performed on matrix grains have shown a low-intensity peak corresponding to oxygen signal. MgO precipitates were perfectly distinguishable because they always displayed a noticeable increase in oxygen signal intensity (Figure 4-19 and Figure 4-20).

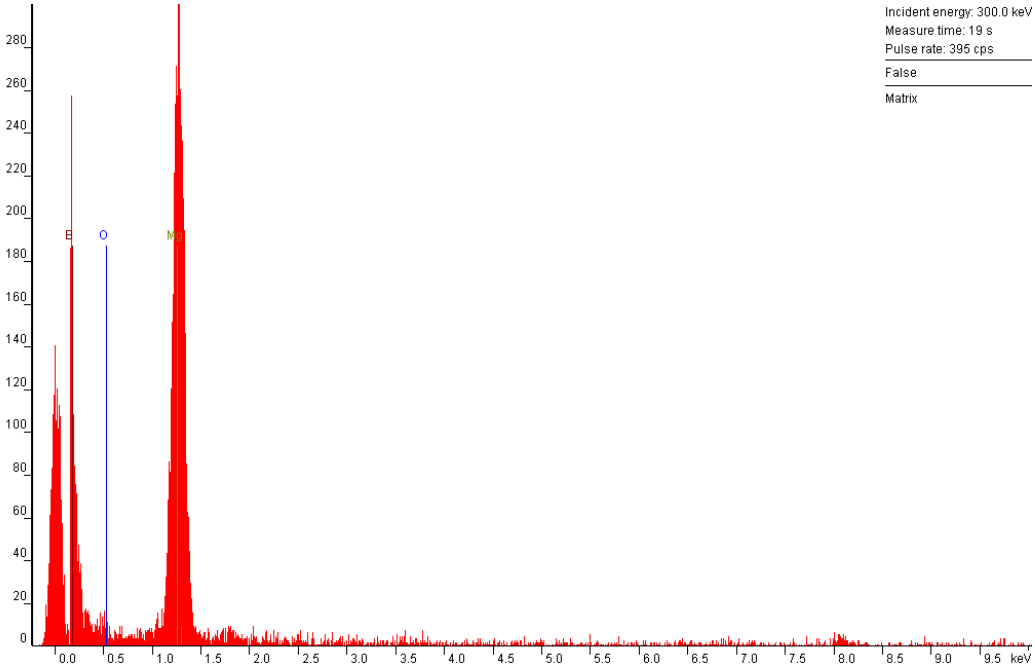

Figure 4-19 – EDS spectrum on MgB_x matrix grains.

Figure 4-20 – EDS spectrum on MgO precipitates.

Figure 4-21 shows MgO grains dispersed and isolated in the microstructural matrix. The shape of MgO grains found on both samples is often rectangular and with well defined facets. On the other hand, the precipitates found are round-shaped with a tendency to acquire the typical regular shape as growth occurs.

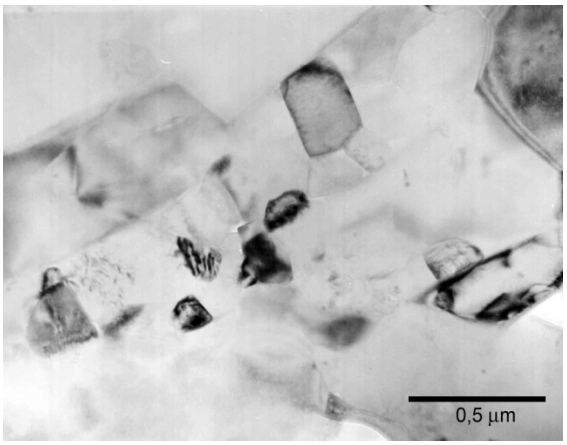

Figure 4-21 – Image showing the dispersion of some MgO grains with different sizes (~0.16 to 0.3 µm) in the matrix.

4.2.3 Set C

Table 4-5 summarizes the results obtained for Set C samples in green and after being HIPed. In this table the relative density values were calculated using the theoretical density value for MgB_2. In this set the weight of the samples has increased during thermal processing.

Table 4-8 – Results of both green and sintered samples of Set C.

		C6	C7	C8	C9
weight (g)	m_0	1.900	1.890	1.900	1.890
	m_f	1.916	1.904	1.911	1.942
	Δm (%)	0.8	0.7	0.6	2.8
diameter (cm)	d_0	1.310	1.310	1.310	1.310
	d_f	1.180	1.175	1.160	1.175
	Δd (%)	9.9	10.3	11.5	10.3
density (%)	ρ_{r0}	65	67	68	68
	ρ_{rf}	87	93	89	88

Caption:

m_0 – green sample mass

m_f – HIPed sample mass

Δm – weight variation, calculated using Equation 4-1

d_0 – green sample diameter

d_f – HIPed sample diameter

Δd – linear retraction, calculated using Equation 4-2

ρ_{r0} – green sample's relative density

ρ_{rf} – HIPed sample's relative density

Phase composition was determined by XRD on all samples and semi-quantification was calculated by Rietveld analysis. A typical XRD of sample C8, with the refinement pattern already included can be seen in Figure 4-22. In samples C8 and C9 no crystalline MgB_4 phase was detected. Instead, weak intensity peaks corresponding to metallic magnesium have appeared. MgB_4 is still present in samples C6 and C7.

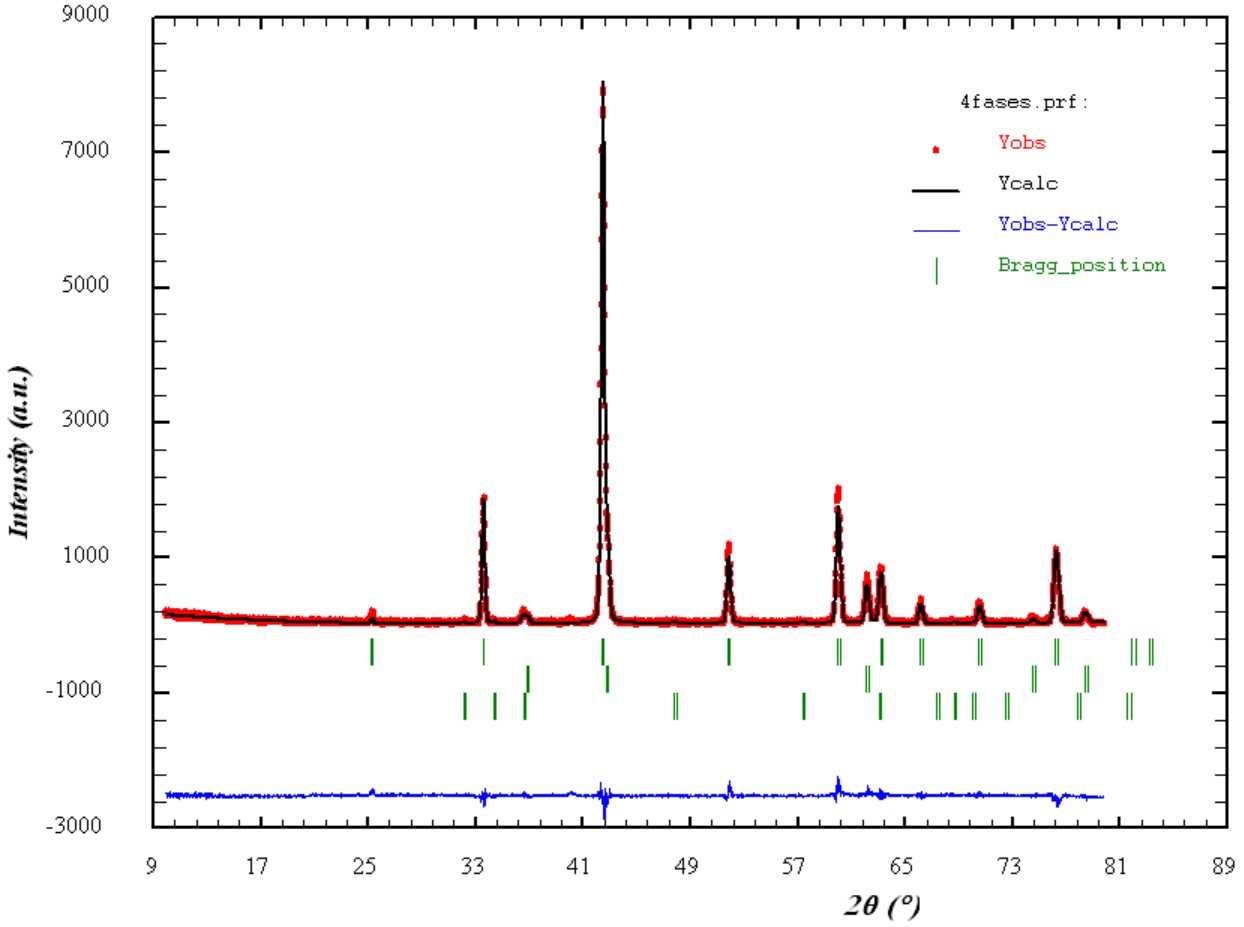

Figure 4-22 – XRD and profile fitting patterns for the sample C8. In the caption *Yobs* refers to the experimental data points (in red), *Ycalc* the refined peaks (in black), *Yobs-Ycalc* is the difference between theoretical and experimental data points (in blue, at the bottom), and *Bragg_position* the diffracting angles for both phases (in green: top – MgB_2, middle – MgO, bottom – Mg).

The density of the samples was measured again, this time using the Arquimedes method, and the weight fractions of the phases were obtained from the Rietveld analysis, exception made to metallic magnesium phase, whose values were lower than the error margin (< 1%). These were used to correct the relative density values and porosity of the samples and are presented in Table 4-9.

Table 4-9 – Phase quantification and corrected relative density values for set B samples.

SET C	Phase composition (weight %)			ρ_t	ρ_{exp}	ρ_r	Π
	MgB_2	MgO	MgB_4	(g/cm^3)	(g/cm^3)	(%)	(%)
C6	77	15	8	2.726	2.469	91	9
C7	79	13	8	2.710	2.558	94	6
C8	89	11	0	2.702	2.659	98	2
C9	86	13	0	2.700	2.652	98	2

caption:

ρ_t – samples' theoretical density

ρ_{exp} – experimental density

ρ_r – relative density

Π – Porosity

All samples were also prepared and observed in SEM. Between sample preparation and SEM observation there was a time lag of roughly two months. During this time, the surface of the samples lost their metallic mirror-like appearance, possibly due to air exposure. To remove this reacted layer, samples C6, C7 and C8 were polished again. Sample C8 was also immersed in HCl 0.1N in an attempt to better reveal the grain boundaries. Sample C9 was observed as it was, and then polished and observed a second time. The collected images are presented in the following table.

Overview images at low magnifications.

Microstructural details at high magnification and sample tilting (35°).

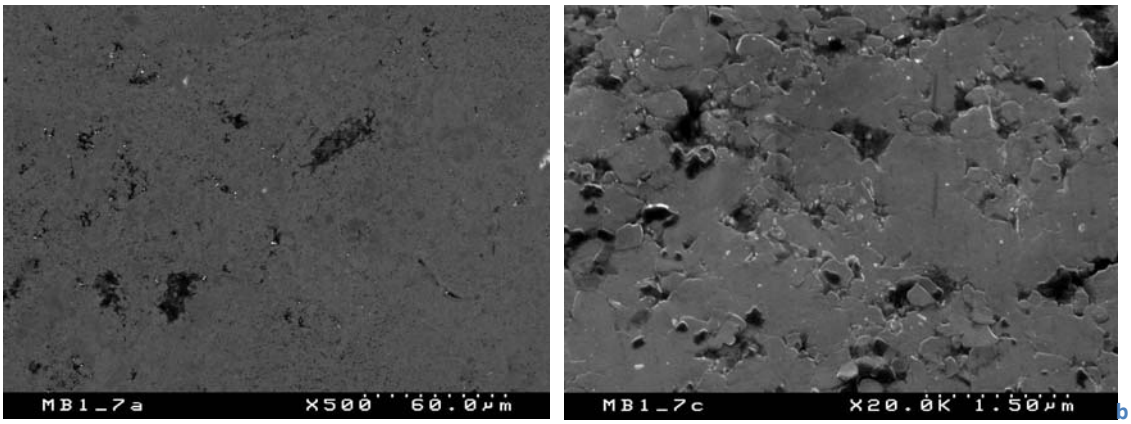

a) b)

Figure 4-23 – Microstructure of sample C6: a) 500x magnified; b) 20000x magnified.

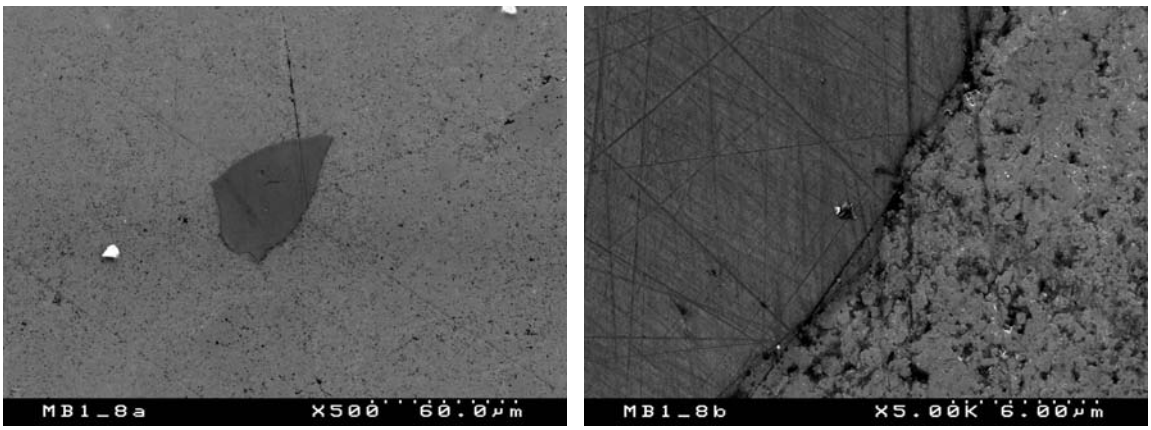

a) b)

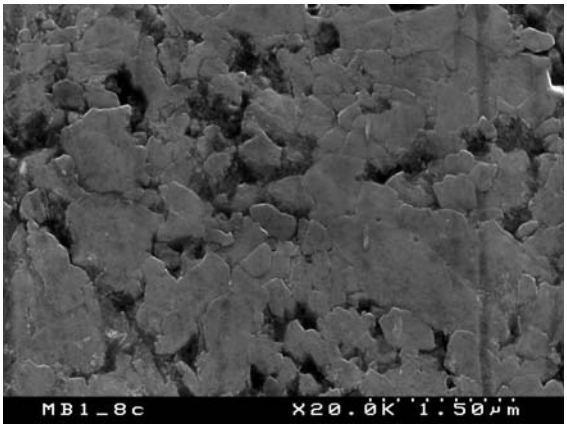

c)

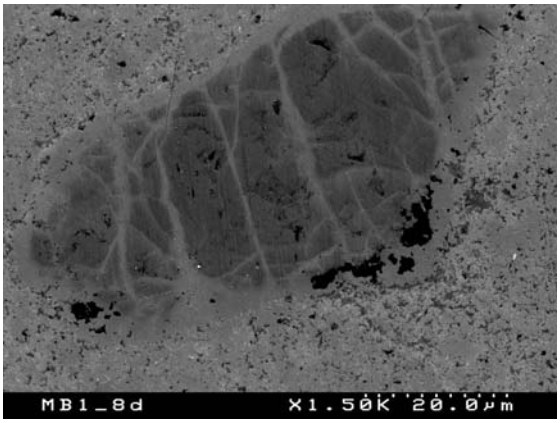

d)

Figure 4-24 – Microstructure of sample C7: a) 500x magnified showing a darker island-like grain embedded in the matrix; b) interface of the grain in a) with the microstructure, showing the polishing scratches (20000x magnified); c) general microstructure (20000x magnified); d) similar feature found in previous micrographs (1500x magnified)

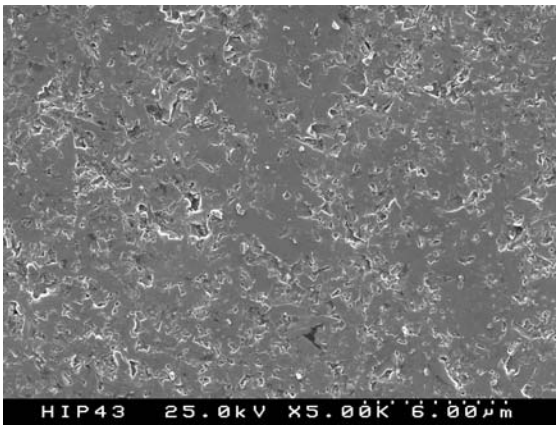

a)

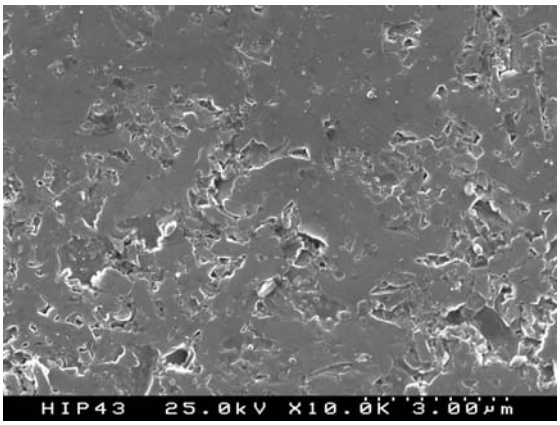

b)

Figure 4-25 – Microstructure of sample C8 after being immersed in HCl solution to clean the surface: a) 5000x magnified; b) 10000x magnified.

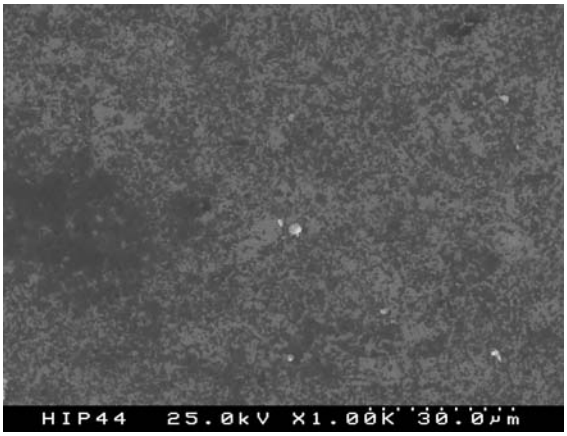

a)

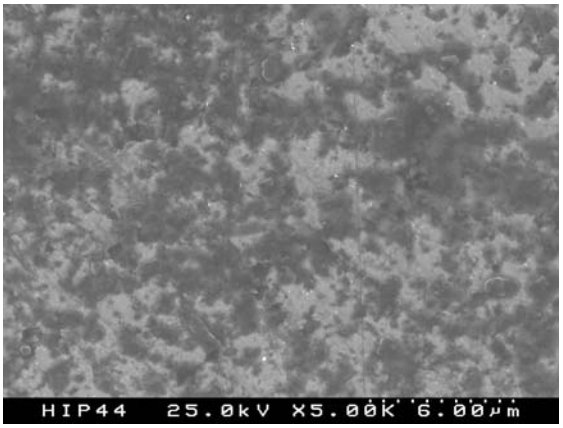

b)

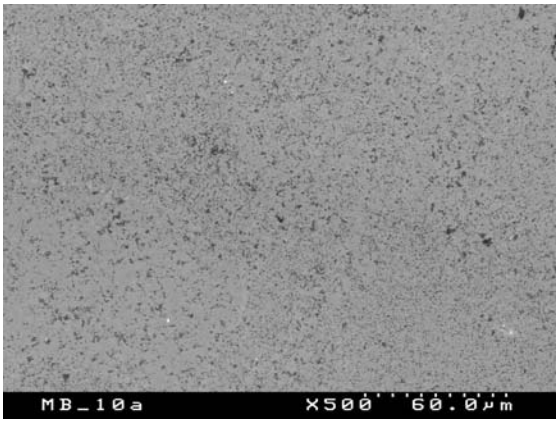

c)

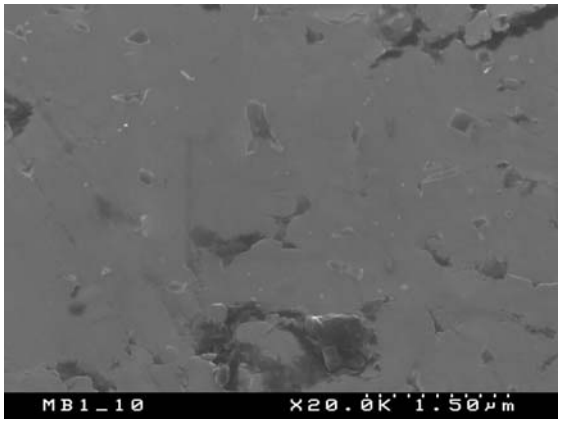

d)

Figure 4-26 – Microstructure of sample C9: a) un-polished sample showing some sort of reaction occurred at the surface; b) close-up of the reactive layer showing that this reaction is preferential in specific areas, while others remain apparently unchanged; c) same sample after being polished (500x magnification); d) magnified 20000x.

A contamination layer that appeared to be over the microstructure (Figure 4-27) was observed. It is possibly the same oxy-hydroxy phase that has been identified by XRD, but confirmation of its chemical composition by EDS was not possible due to this technique's limitation regarding light-weight elements. It is fundamental to avoid such contaminations if one wishes to perform TEM observation on the samples.

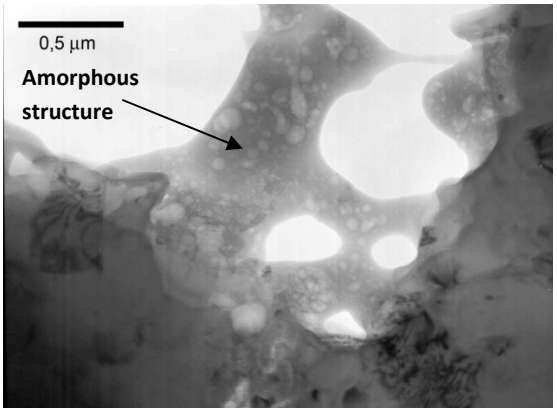

Figure 4-27 – Micrograph showing an amorphous layer, forming a web-like structure that interconnects the grains in the microstructure.

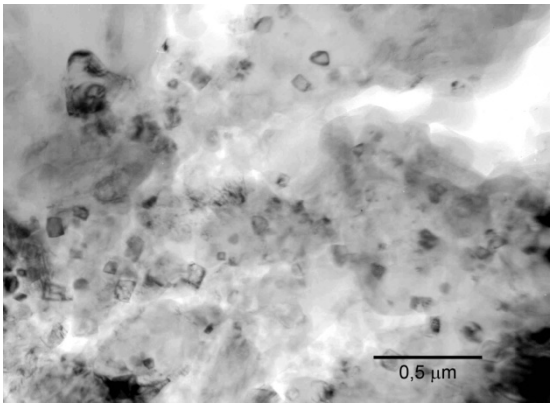

Figure 4-28 – Micrograph displaying an overview of the microstructure veiled by the contamination layer.

General microstructure of the sample consists of a matrix of MgB_2 / MgB_4 grains and small precipitates of MgO. MgB_2 and MgB_4 are undistinguishable both visually and by EDS performed, due to limited boron detection. In terms of observed grain size, it was possible throughout the observation to see that the

matrix grains range from ~3μm to sub-micron particles. MgO precipitates presented a size range of 20 to 100 nm (Figure 4-29 and Figure 4-30). It evidences MgB_x grains presenting intra-granular dislocations, which is often observed in TEM imaging of materials processed under pressure. The visualization of these defects relies on a variation of atomic planes in respect to the direction of the incident electron beam.

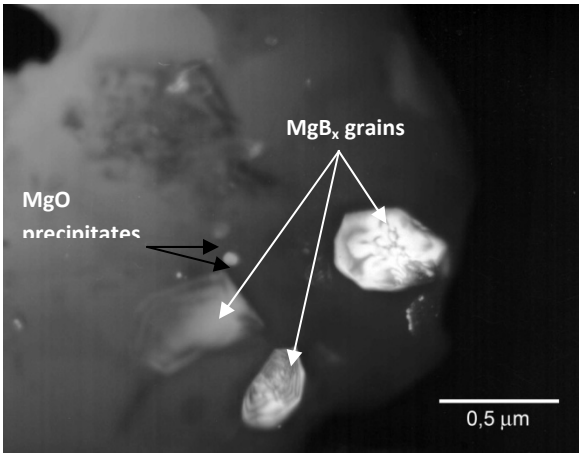

Figure 4-29 – Darkfield micrograph evidencing MgB_x grains and small MgO precipitates.

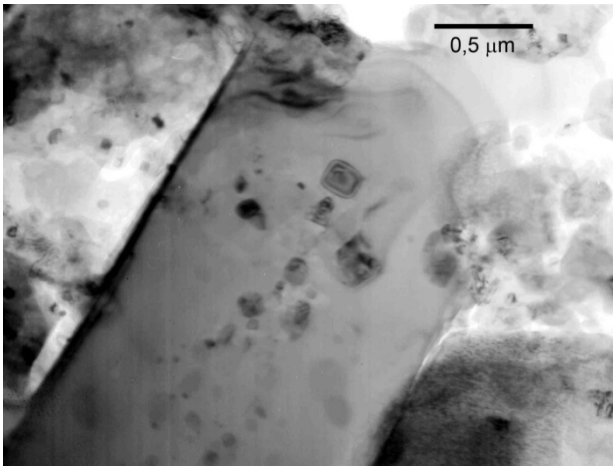

Figure 4-30 – Micrograph displaying an MgB_x grain with MgO precipitates over it.

MgO precipitates can be found dispersed throughout the microstructure, although at times they give the impression of being inside the matrix grains (Figure 4-30).

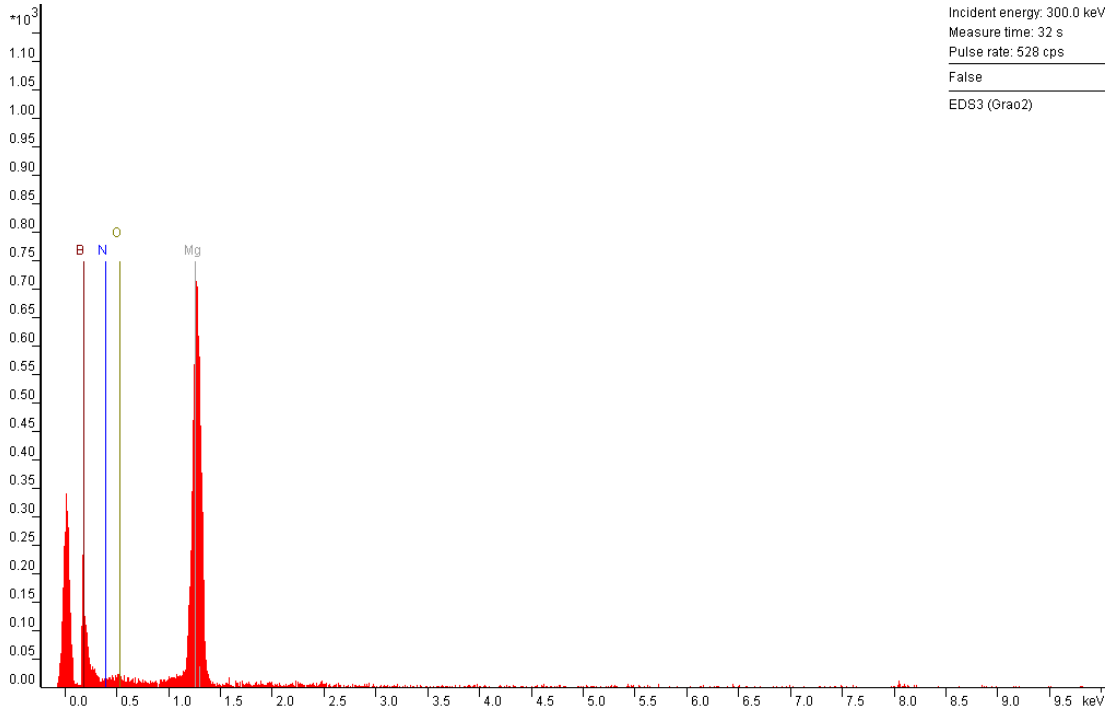

Figure 4-31– EDS spectrum resulting from the MGB_x grain in Figure 4-30.

4.2.4 Low angle X-ray diffraction

After samples from set C had shown signs of surface reaction while pending for SEM observation, the remaining samples were checked. At the time when this was situation was verified, sample A1 was no longer available for further studies. The surface of all the remaining samples, prepared in sets B and C, have shown some signs of alteration after being exposed to air. Apparently samples from set C were much more affected than those of set B. This was visible even by naked eye as the samples loose their metallic mirror-like appearance. It was also visible under SEM observation, as can be seen in Figure 4-26-a) and b). Low angle XRD was performed at an angle of 4°, in an attempt to find the composition of this superficial reaction layer. A summary of the results for all samples is presented in Table 4-10. Indication of an oxyhydroxyde - $MgBO_2(OH)$ - was detected only from samples C7 to C9.

Table 4-10 – Summary of the secondary phases (besides MgB_2 and MgO) detected by low-angle X-Ray diffraction; graphic sign * was used to identify the second results for sample C9, after being polished.

Sample	Secondary Phases		
	MgB_4	Mg	$MgBO_2(OH)$
B2	X		
B3	X		
B4	X		
B5	X		
C6	X		
C7		X	X
C8		X	X
C9		X	X
C9*	X	X	X

Sample C9 was polished in an attempt to remove the contamination layer and tested again. It was expected that the $MgBO_2(OH)$ would disappear, since it should be only superficial. Instead this second analysis still detected its presence and MgB_4 phase was also detected. Elemental magnesium was detected in samples C7 to C9, confirming the previous results obtained by conventional XRD. Samples were coated with sputtered carbon for SEM observation and some samples still had remains on their surface. This explains the carbon peaks found in some of the samples. Representative patterns are shown in Figure 4-32 and Figure 4-33.

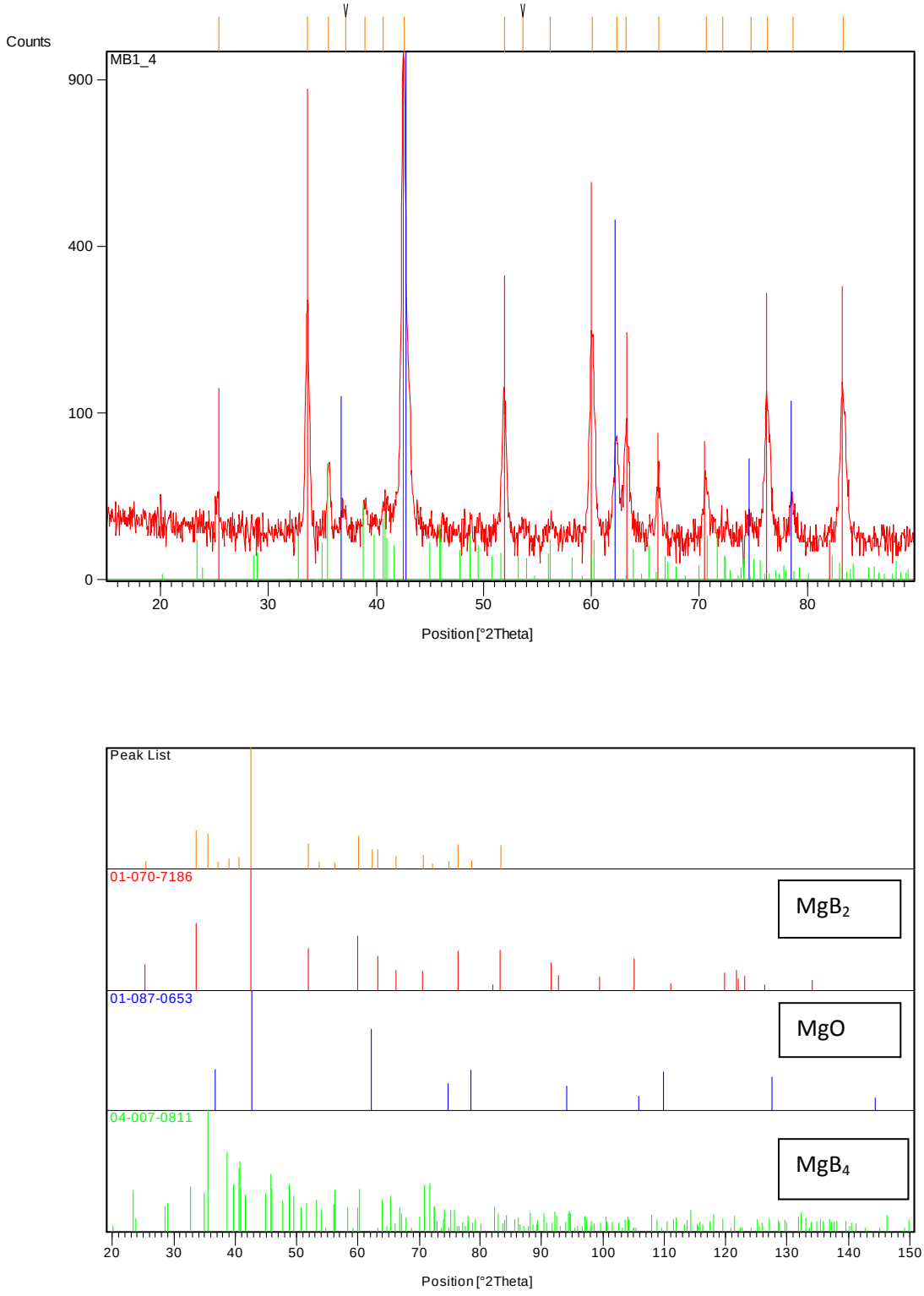

Figure 4-32 – Above: Low-angle diffraction pattern obtained for sample B3; Below: Peak list for the phases detected.

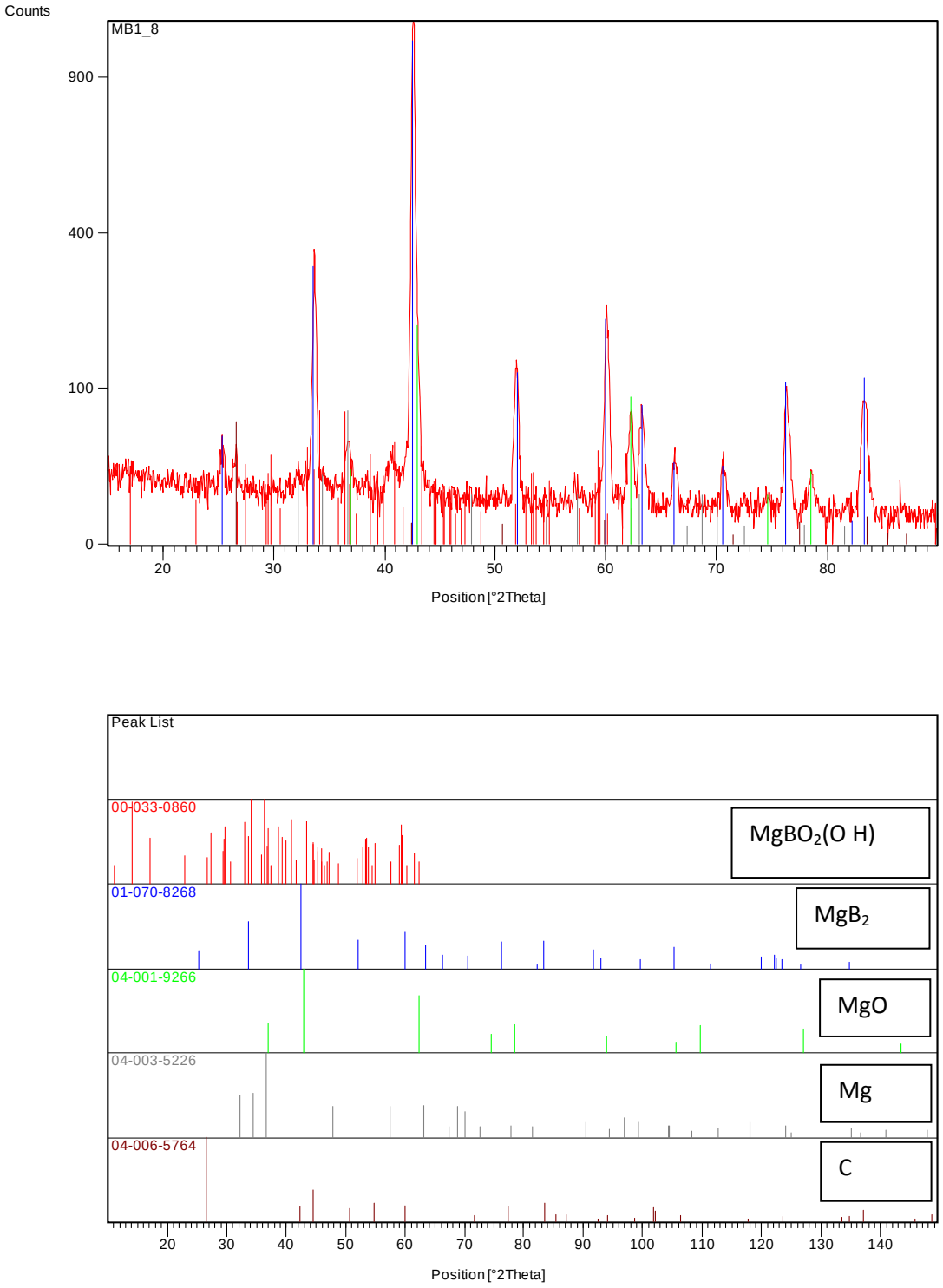

Figure 4-33 – Above: Low-angle diffraction pattern obtained for sample C7; Below: Peak list for the phases detected.

4.3 In situ samples

For this set of experiences, 3 capsules were initially prepared. Capsule C opened up during thermal treatment and a second capsule was prepared and sintered. These were designated capsules C-a and C-b, respectively. The following table shows the results of measuring and weighing, as well as density values for all the green in situ samples prepared.

Table 4-11 – Green sample's average dimensions and density values.

Composition	#	m_0 (g)	d (cm)	h (cm)	ρ_g (g/cm^3)
A **1 : 2**	1 2 3	1.000	1.310	0.500	1.48
B **1.2 : 2**	1 2 3	1.000	1.310	0.500	1.48
C-a **1.5 : 2**	1 2 3	0.994	1.310	0.487	1.52
C-b **1.5 : 2**	1 2 3	0.998	1.310	0.548	1.35

Caption:
m_0 – weight
d – diameter
h - height
ρ_g – geometrical density

Table 4-12 shows the results obtained after sample sintering, including linear retraction and weight variation obtained from the same formulas used previously for *ex situ* samples. These samples were darker than the HIPed samples, very fragile and had to be handled with care.

Table 4-12 – Resulting sample dimensions and densities after sintering.

Composition	#	m_f (g)	d (cm)	h (cm)	ρ_g (g/cm^3)	Δd (%)	Δm (%)	ρ_r (%)
A	1	0.907		0.545	1.154	9.0	-9.3	44.0
	2	0.911	1.355	0.535	1.180	7.0	-8.9	45.0
1:2	3	0.896		0.535	1.161	7.0	-10.4	44.2
				$\bar{x} =$	**1.2**	**7.6**	**-9.5**	**44.4**
B	1	0.809		0.520	1.078	6.1	-19.1	41.1
	2	0.854	1.355	0.535	1.107	9.2	-14.6	42.2
1.2 : 2	3	0.821		0.520	1.095	6.1	-17.9	41.7
				$\bar{x} =$	**1.1**	**7.1**	**-17.2**	**41.7**
C-a	1	0.693		0.495	0.971	4.2	-30.7	37.0
	2	0.707	1.355	0.500	0.980	2.0	-29.3	37.3
1.5 : 2	3	0.691		0.490	0.978	-1.0	-30.9	37.3
				$\bar{x} =$	**1.0**	**1.7**	**-29.9**	**37.2**
C-b	1	0.724		0.560	0.896	1.8	-27.6	34.1
	2	0.748	1.355	0.550	0.944	0.9	-24.8	35.9
1.5 : 2	3	0.752		0.560	0.931	1.8	-24.8	35.5
				$\bar{x} =$	**0.9**	**1.5**	**-25.7**	**35.2**

Caption:

m_f – weight
Δl – linear retraction
ρ_g – geometrical density
d – diameter
Δm – mass variation
h – height
ρ_r – relative density

Comparative analysis of the previous tables shows that the samples have lost weight during sintering and underwent an expansion, leading to a decrease in the sample's density to values close to 40%. Also, comparing the results obtained for composition C samples, it is visible that the fact capsule C-a opened inside the furnace has caused a greater weight loss and expansion. Regardless of that, these samples apparently have relatively higher density values.

Similarly to *ex situ* processed samples, composition was determined by XRD on all samples and semi-quantification was calculated by Rietveld analysis. A typical XRD with the refinement pattern already included can be seen in Figure 4-34, where two crystalline phases have been identified: MgB_2 and MgO. Although possibly present in the samples, there are no peaks in the diffraction pattern that correspond to boron, for it is an amorphous phase. There are some unidentified peaks in the patterns, quite visible near the baseline. They must correspond to a third phase, but it was not possible do match any known phases in the database to them.

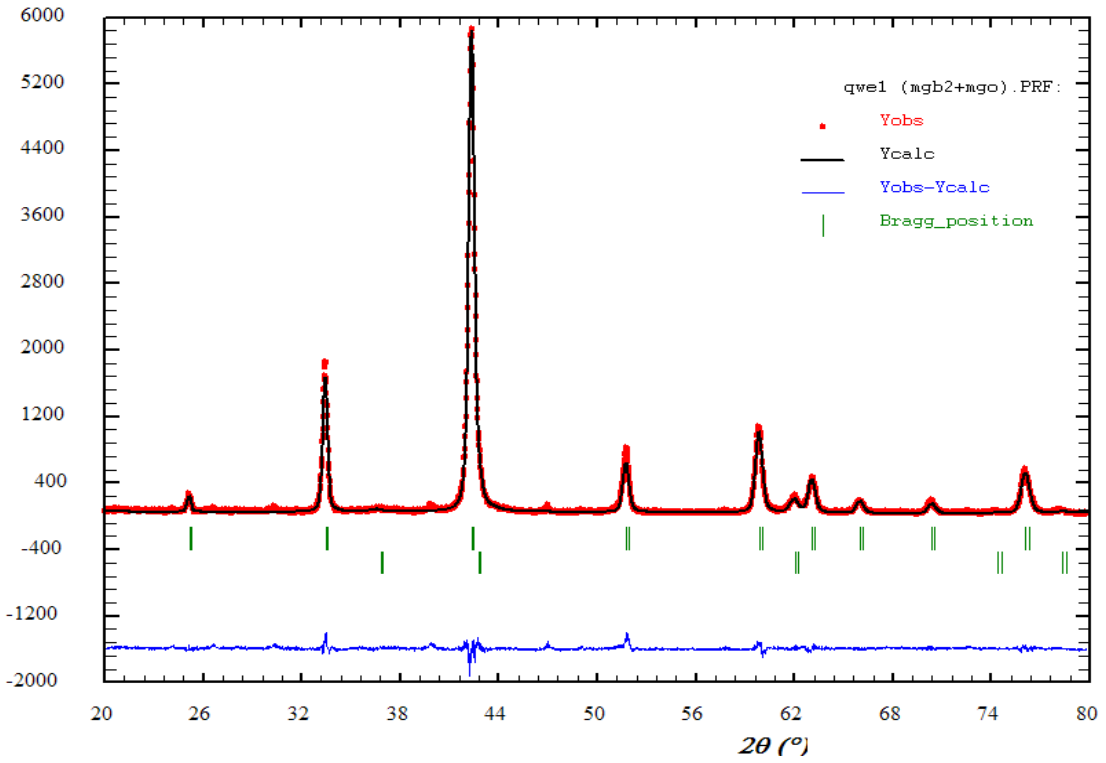

Figure 4-34 – XRD and profile fitting patterns for the sample B2. In the caption *Yobs* refers to the experimental data points (in red), *Ycalc* the refined peaks (in black), *Yobs-Ycalc* is the difference between theoretical and experimental data points (in blue, at the bottom), and *Bragg_position* the diffracting angles for both phases (in green: top – MgB_2, bottom – MgO).

In Table 4-13 the weight fraction values for both crystalline phases are presented. From these the volume fractions of each crystalline phase, as well as the porosity volume were calculated.

Table 4-13 – Results of phase quantification, both in volume and weight percentage, corrected density and porosity values for each sample.

Sample	Phase composition						ρ_g	ρ_t	ρ_r	Π
	(weight %)		(vol. %)		(real vol. %)					
	MgB_2	MgO	MgB_2	MgO	MgB_2	MgO	(g/cm^3)	(g/cm^3)	(%)	(%)
A1	92	8	94	6	40	3	1.154	2.683	43	57
A2	93	7	95	5	42	2	1.180	2.676	44	56
A3	88	12	91	9	39	4	1.161	2.713	43	57
B1	--	--	--	--	--	--	--	--	--	--
B2	95	5	96	4	40	2	1.107	2.661	42	58
B3	98	2	99	1	41	1	1.095	2.639	42	58
C1-a	59	41	66	34	22	11	0.971	2.953	33	67
C2-a	50	50	58	42	19	12	0.980	3.036	32	68
C3-a	65	35	72	28	24	9	0.978	2.900	34	66
C1-b	95	5	96	4	32	1	0.896	2.661	34	66
C2-b	96	4	97	3	35	1	0.944	2.654	36	64
C3-b	94	6	96	4	33	2	0.931	2.668	35	65

Caption:

weight % – relative weight fraction

vol. % – relative volume fraction

real vol. % – relative volume fraction with porosity

ρ_g – geometrical density

ρ_t – corrected theoretical density (calculated according to Equation 3-2)

ρ_r – relative density

Π – porosity fraction

Composition B has the highest relative density and superconducting phase obtained relatively to the amount of MgO. For all samples except those in capsule C-a, the amount of MgO was limited to a maximum value of 3 (wt. %).

All samples were prepared and observed in SEM. The collected images are presented in the following set of figures. The microstructures made up of a highly porous matrix (areas labelled “2”) with some denser particles dispersed and embedded in it (areas labelled “1”).

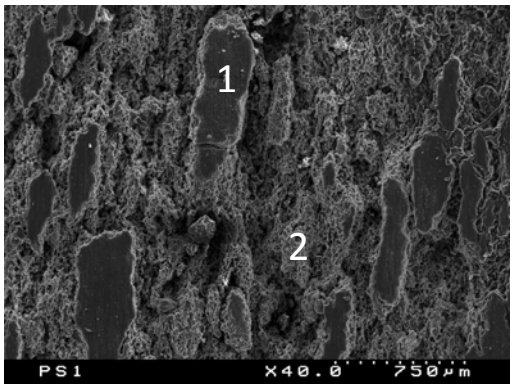

Figure 4-35 – Sample A1’s microstructure showing two distinct regions, marked 1 and 2.

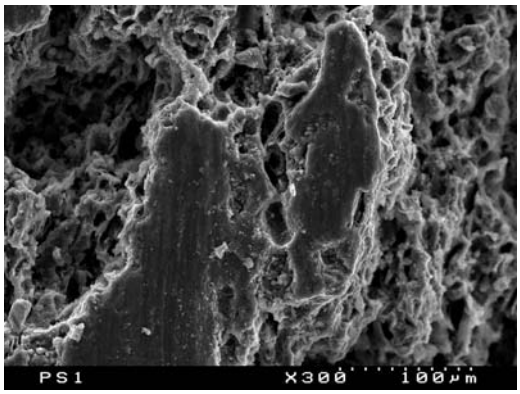

Figure 4-36 – Detailed view of region 1 in sample A1. (magnification 300x).

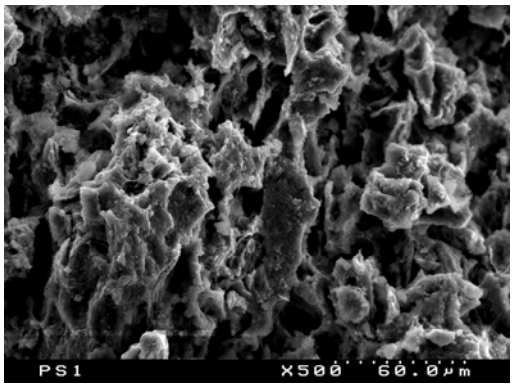

Figure 4-37 – Detailed view of region 2 in sample A1. (magnification 500x).

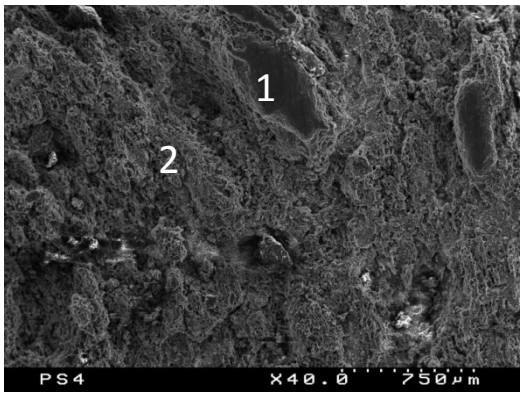

Figure 4-38 – Sample C3-a microstructure, again with two separate regions identified in the picture (magnification 40x).

5 Discussion and Conclusions

In this chapter all the results presented so far will be discussed following the same sequence found in the previous chapters. A list of conclusions will then be compiled and correlated with the electric and magnetic properties resulting from the samples physical characterization.

5.1 Ex situ

One of the major objectives during *ex situ* processing was to limit the amount of remnant MgO phase in the finished samples. MgO is known to be one of the most stable oxides. Combined analysis using XRD and Rietveld has determined its amount to be about 5 % wt. in the initial powder mixture. A second objective was to improve the density of the samples. Higher density values can be associated with increased intergranular connectivity. This effect was expected to positively influence the mechanical resistance of the samples as well as the electrical transport of superconducting currents. Reducing the amount of voids in the samples will increase the interfacial contact area between grains, indicated by an increase in the relative density values. In the same way, increasing the contact area will provide alternative routes for the current flow thus enhancing the percolation path. Maximizing the superconducting phase content was a third objective as it was expected to contribute with larger fraction volumes of superconductive material, thus also maximizing the samples' J_c. These aspects will be taken into consideration in the following discussion of the results.

5.1.1 Set A

5.1.1.1 Densification

The initial sample from SET A was a first attempt to produce a dense MgB_2 superconducting sample. With a final relative density value slightly above 88%, it is safe to say that the objectives were met. Some expected problems did occur, such as the fact that molten glass had adhered to the sample and had to be mechanically removed to the expense of the sample's integrity.

The relative amount of MgO increased almost three and a half times to 17% in the finished sample and 8% of MgB_4 was formed during processing. From these results the new objectives for the next set of samples were to increase the samples' density as much as possible and to avoid the formation of MgB_4, while maintaining the amount of MgO phase under control.

5.1.1.2 Formation of MgO and MgB_4

The presence of MgO and MgB_4 can be associated to MgB_2 decomposition during sample processing[34]. MgB_2 dissociation results in MgB_4 and magnesium; the free magnesium will easily react with any oxygen that remains inside the capsule or in the powder mixture despite the purge during vacuum encapsulation, and lead to oxidation of the samples during the HIP cycle resulting in additional MgO content. Therefore in the following preparations, extra magnesium was added to the bottom of the capsules with the intent to create a magnesium-enriched atmosphere which should deter the dissociation process and compete for the available oxygen inside the capsule. In addition, the samples were wrapped with metallic foil to avoid contact between the sample and the glass at all times. From the bibliographic survey tantalum and zirconium were the selected materials, since they tend to oxidize and would also compete for any available oxygen.

5.1.2 Set B

Even though these samples were sintered at a lower pressure than the previous sample, similar densification values were achieved in samples B2-4, while sample B5 reached 90%. Weight loss averaged 6.4% in all samples, except in the case of sample B5 where it was limited to 0.6%. Linear shrinkage values show a similar behaviour, averaging 10% in samples B2-4 and 6% in sample B5. These results seem to be the result of the proximity between the samples and the extra magnesium in the bottom of the capsule.

It can be seen in Table 5-1 that by taking the phase composition into account for the calculation of theoretical densities, the relative density values differ from those obtained geometrically. The latter are believed to be more accurate. Although there aren't any differences in the first 3 samples, the case of sample B5 shows that this difference can be significant. It is the sample with least amount of superconducting phase and also the most densified as opposed to being the least dense. The average relative density for this set of samples is 89%, representing a slight improvement when compared to sample A1, despite the relatively lower processing pressure.

Table 5-1 – Density values obtained by two different methods.

Sample	geometrical density (%)	corrected (Archimedes) (%)
B2	89	89
B3	88	88
B4	88	88
B5	80	90
	$\overline{\rho}$=86	$\overline{\rho}$=89

XRD results have shown that all samples are composed of a combination of MgB_2, MgB_4 and MgO. Rietveld composition analysis shows that there is still a considerable amount of both MgO and MgB_4 in the final samples. On average the amount of the former increased 2 to 3 times during processing from the initial amount of 5% initially found in the powders. When compared to sample A1, the amount of MgB_4 found in set B samples decreased to an average of 6.5%. The amount of MgB_2 is about 80% for all samples. Overall these results are slightly better than those obtained for the initial sample. Considering the different processing conditions they show improvement.

The effect of the extra magnesium on the results becomes relevant when one realizes the disposition of the samples inside the capsule: B2 was the closest to this extra source of magnesium, followed sequentially by the remaining samples. Even though in a first approximation the conditions inside the capsule should be the same all around, the fact is that the results show otherwise. There is a slight decrease of density from sample B2 to B5. In the same way, there's also a slight increase in the amounts of secondary phases. Therefore it is quite possible that these results are positively influenced by the proximity of the sample to the magnesium. This relationship will be developed in the next set of results.

5.1.2.1 SEM

The observed microstructures are very similar in all of the samples, even in the local features that are somewhat spread throughout the observed surfaces and that differ from the typical matrix. It is possible to identify three distinct areas in the images which were captured in the same micrograph, shown in Figure 5-1. The microstructure was divided into different regions according to their characteristics, labelled 1,2 and 3 on the figure.

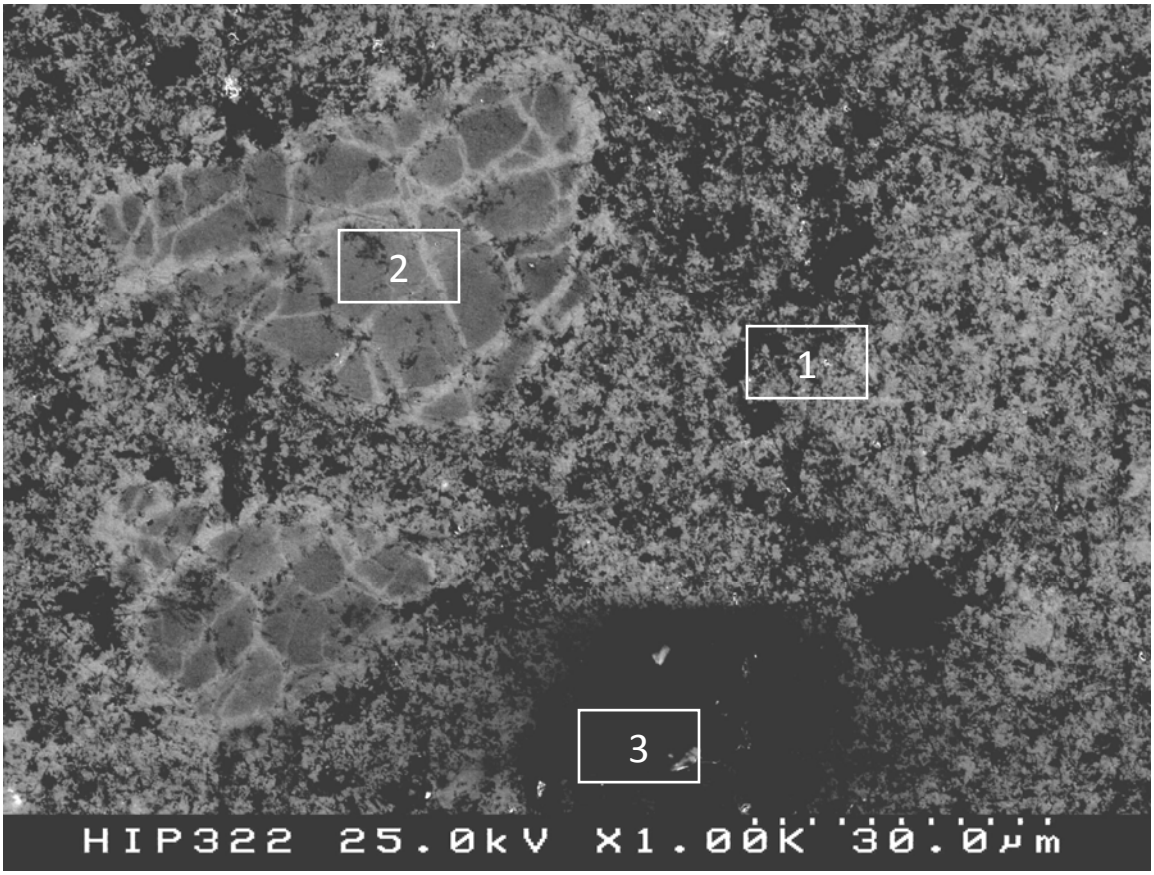

Figure 5-1 – SEM image showing some microstructural features of sample B3. The white rectangles indicate the 3 separate zones into which the microstructure can be divided.

Area labelled "1" represents the overwhelming majority of all sample's observable surface area. At higher magnification (seen in Figure 5-2) it is possible to see that the microstructure is granular, comprised of particles with irregular shapes and sizes, which can vary from 0.3 µm to 1 µm.

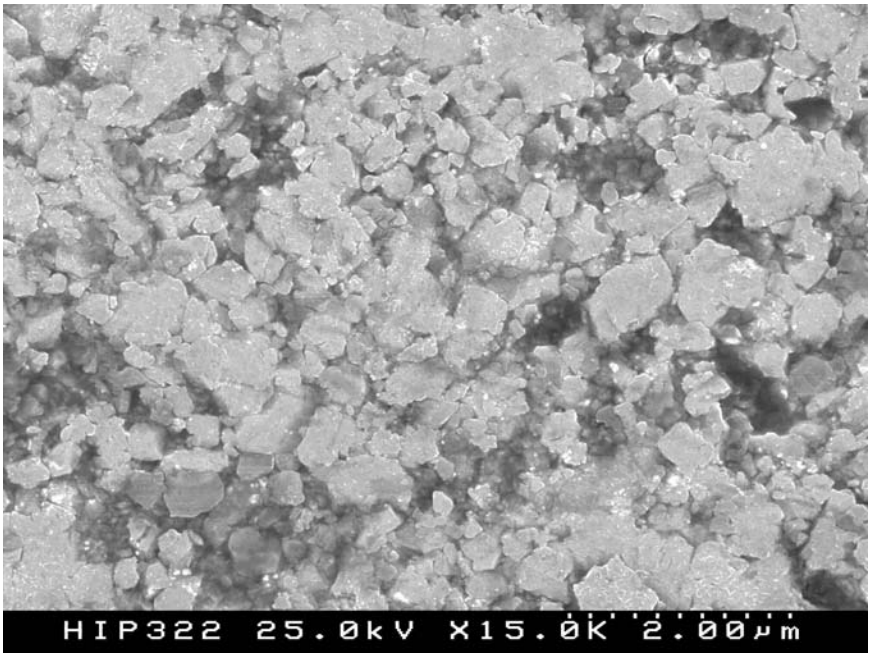

Figure 5-2 – Detail of the area labelled "1" in the previous figure. The darker areas are not seen at 15.000 magnification.

EDS analysis has revealed that the chemical composition consists of magnesium, boron and oxygen, which was expected. However, phases MgB_2 and MgB_4 are chemically indistinguishable under EDS analysis. Any attempt to make an elemental quantification would result in inaccurate results due to the fact that the beam interaction volume inside the sample would be too great for both magnesium and especially boron, which are light-weight elements. Combined with the small particle sizes this would result in a total interaction volume greater than the volume of the particle under analysis. Inevitably one would get chemical results not only from the desired particle but also from the immediate surroundings. The same reasoning may be applied to MgO particles. The detected signal for boron is, in any case, quite small and always subjected to some error. Given the chemical composition of the samples, boron should be the most abundant element detected in any EDS analysis performed. Yet it is usually the peak with less intensity. For these reasons, EDS was not performed in a specific point but in a general area instead. In this way it was possible to get a better idea of what elements are present in average in that area. For instances, it is possible to state that there is oxygen inside area 1, since there is a peak corresponding to oxygen in the resulting spectrograph. The form in which oxygen is present is not exactly clear, but it most probably comes from dispersed MgO particles identified previously by XRD.

Area labelled "2" is quite different. In Figure 5-3 a micrograph of a similar structure in the same sample is shown.

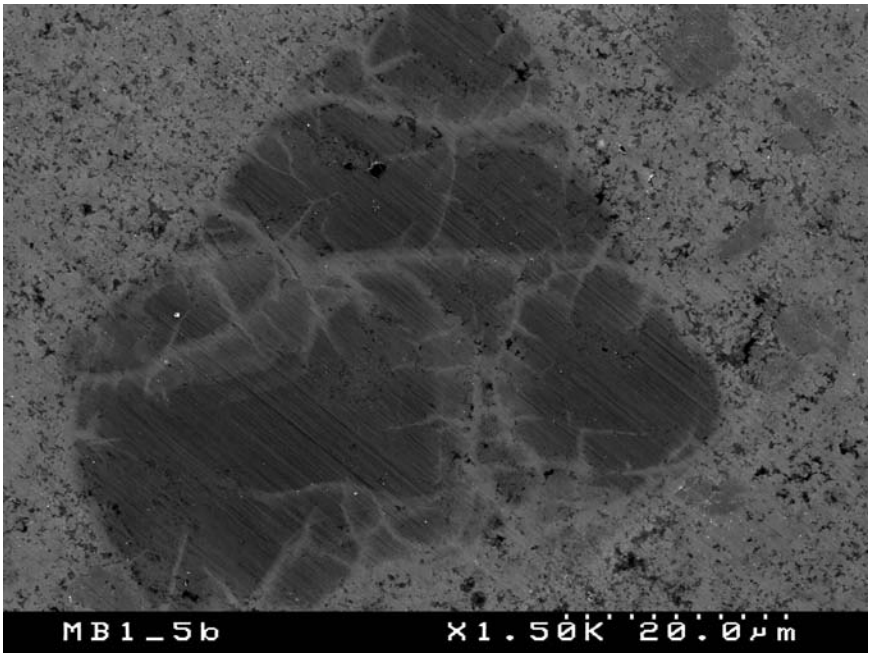

Figure 5-3 – SEM micrograph showing a darker area crossed by lighter ones, similar to the one found in area 2 in Figure 5-1.

Its shape is irregular and while the majority of the area has a slightly darker tonality than its surroundings, it is crossed by lines which in turn are lighter. This feature was only found in two samples: B4 and C7. EDS shows an Mg-B based compound together with a negligible signal for oxygen, if one takes into consideration the previous arguments regarding the signal intensity and sensibility. Because there is a contrast showing at least two different areas, one lighter than the other, it is valid to argue that it is a result of atomic weight contrast. Under this argument, the lighter areas should be richer in magnesium than the darker ones. In principle, because there are only two crystalline phases indentified by XRD which match these compositions, the darker areas should be MgB_2 and the lighter ones MgB_4. However, there are published results that state that there is a wide variation in stoichiometry for MgB_x compounds. In reference[172] similar structures were found, but in that case specifically, it was a very common feature that could be found in most of the grains. Electron probe microanalysis (EPMA) revealed Mg/B ratios that pointed to compositions such as MgB_2, MgB_7 and MgB_{12}. Because no XRD results were presented, one assumes that these conclusions were based only on electron microscopy and EPMA analysis. Such is not this case. Area labelled “3” is an internal pore and it is almost black in colour due to topography effects that make depressions appear in darker shades. This effect is particularly sensitive to the magnification at which one is observing the sample: the lowest the magnification, the stronger the effect as can be seen comparing Figure 5-1 and Figure 5-2. Whereas in the latter the interior of the depressions can be seen clearly without any indication of composition differences, the former shows every depression in a darker shade.

5.1.2.2 TEM

TEM studies have allowed identification and characterization of MgO particles in the samples. Unlike SEM where the sample is observed in bulk state, TEM observation is done on a very thin layer near the perforation edge. This limits the interaction volume simply because the volume of the samples is reduced to a minimum. In this way it is possible to run EDS on a specific grain and in case any oxygen is detected it is almost certainly from the chosen grain. Results have shown that MgO is present in two different forms: precipitates and fully grown grains. Precipitates are smaller in size (<0.1 μm) and are rounder in shape. They originate from magnesium resulting from MgB_2 dissociation, consequently reacting with any available oxygen or even from the free metallic magnesium inserted inside the processing capsule. MgO grains have a rectangular shape and are larger in size. These are already present in the initial powders and can also be the result of precipitate growth during processing. In either shape or form, MgO was not seen incorporated inside the matrix grains but isolated at the boundaries of MgB_2 grains instead.

For the same reason presented in the discussion of SEM results, the matrix grains could not be identified as being either MgB_2 or MgB_4. Typical particle size ranged from 3 μm to below 1 μm which are similar values to those obtained for the initial powders. This shows that there wasn't much grain growth occurring during thermal treatment. The grains have an irregular shape and appear to be well connected. There are some dislocation lines visible on their interior. These are a common feature of HIPed samples due to the external pressure applied to the samples which distorts the lattice structure. These results show that HIPing under these experimental parameters promotes densification of the samples, but not grain growth. This was also expected and is also related to the external pressure applied which increases the energy required for grain growth to occur.

5.1.3 Set C

The HIPing parameters for this set of samples had the highest value of applied pressure and the lowest hold time of all of the previous sets.

Contrary to the previous results, samples in this set have gained weight during HIPing while linear retraction values are slightly larger than those in set B. The average weight gain amounted to 0.7%, except that of sample C9 which was of 2.8%. This represents a difference of at least 3.5 times more than that of any other sample in this set. Again this seems to be related to the disposition of the samples

inside the capsule relatively to the source of extra magnesium. This time around sample C9 was closest to it, with distance increasing in the reverse sample order.

Table 5-2 – Density values obtained by two different methods.

Sample	geometrical density (%)	corrected (Archimedes) (%)
C6	87	91
C7	93	94
C8	89	98
C9	88	98
	$\overline{\rho}$=89	$\overline{\rho}$=95

This hypothesis is further supported with the results obtained for sample densities (Table 5-2). In the light of the previous argument regarding the two different methods by which these values were obtained, and which support the accuracy of the corrected values, only the second set of density values will be discussed. Average relative density for all samples was of 95%. This represents an increase of 6% over the previous set. Once more, samples C8 and C9 which were closer to the extra magnesium have the highest relative density values with 98%. Therefore one may conclude that the presence of magnesium on the sintering atmosphere (inside the capsule) improves the mechanical resistance of the samples by reducing porosity. On the other hand, while it is and effective way to hinder MgB_2 dissociation, it may be responsible for some of the MgO detected on the final samples.

XRD results show that the two samples that were farther from the extra magnesium source still developed MgB_4, while the two closest to it did not. For the latter, small amounts (below 1 % wt.) of metallic magnesium was detected and quantified, which accounts for the weight gain discussed earlier. The amount of MgB_4 calculated for samples C6 and C7 was of 8%. The amount of MgO is practically the same for all samples, averaging 13%. These are similar results to the ones obtained in Set B. The amount of superconducting phase averages 83% with a maximum of 89% and a minimum of 77% in sample C8 and C9, respectively.

Two issues arise from these results: on one hand, the higher the amount of detected MgB_4, the higher the amount of MgO (sample B3 is the only exception); on the other hand, samples C8 and C9 have no MgB_4, but still have similar amounts of MgO to those of C6 and C7. While it is still reasonable to assume that MgO and MgB_4 are a result from MgB_2 dissociation, it is not clear how the amount of MgO in samples C8 and C9 rose from 5% in the initial powders to ~12% in the processed samples, without forming any MgB_4. The hypothesis developed during this work is that some MgO has its origin in the extra magnesium which gets oxidized earlier in the processing cycle, instead of resulting from MgB_2 dissociation. Nonetheless, the final density values are quite positive and contribute significantly to the samples' mechanical properties allowing them not only to be easily handled, but also to be machined

into any desirable shapes. These results are certainly associated with the highest pressure applied during sintering which certainly contributed to sample densification. Despite the shorter hold time of 1,5 hours at 950 °C programmed for this HIP cycle formation of MgB_4 and oxidation of magnesium still occurred. One can conclude that shorter cycles at lower sintering temperatures in MgB_2 sample processing are not only possible and desirable, but advantageous from the results standpoint.

5.1.3.1 SEM

The microstructural changes associated to the increase of density values are clearly visible in the SEM micrographs obtained. The particles are much better interconnected. The microstructure of samples C6 and C7 still resembles those of the previous set but with better grain connectivity and less porosity. Grain sizes are quite similar to those found in set B, showing again that not much grain growth occurs during sintering. The microstructures of samples C8 and C9 are evidently denser than those in any other sample. In sample C7 an uncommon feature was found and presented in Figure 5-4. It appears to be a particle embedded in the microstructure. Some scratch lines crossing it are a result of sample polishing and indicate a lower hardness. Its size is largely superior to any other particle in the microstructure. EDS performed on this particle did not show any chemical difference from the surroundings. Given its darker shade this is believed to be a boron-rich area. Boron atoms provide weak scattering centres for X-ray diffraction so, the amount of this phase in the sample may not be enough to show up in the XRD patterns. One other hypothesis is that it is not a crystalline phase and as such, it is permeable to the technique. SEM does not allow one to reach definite conclusions in this regard. In reference [55] similar features were found and analysis also pointed to a B-rich composition, although no additional specifications were made. This sample also has a similar structure to that discussed previously for sample B4.

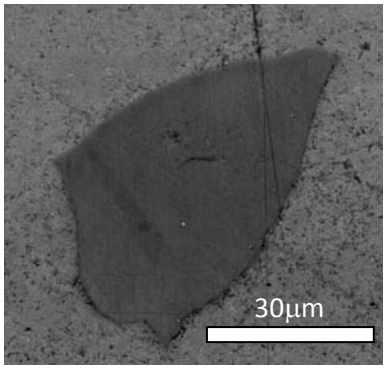

Figure 5-4 – Sample C7 micrograph taken in SEM at 500x magnification showing a darker island-like grain embedded in the matrix.

Immersing the sample in HCl did not result in clearer grain boundaries, but it did clean the surface and provided a clearer view of the microstructure. The surface changes that have occurred are believed to be the result of a reaction between the surface of the samples and the surrounding atmosphere. It is clear in that before the sample was polished a second time, a thin reaction layer over the microstructure was visible (Figure 5-5). Again, EDS was unable to reveal any chemical differences. The layer is not homogeneously spread along the surface. Instead it seems that it is limited, at least at this point, to certain areas of the microstructure, while other areas seem unaffected.

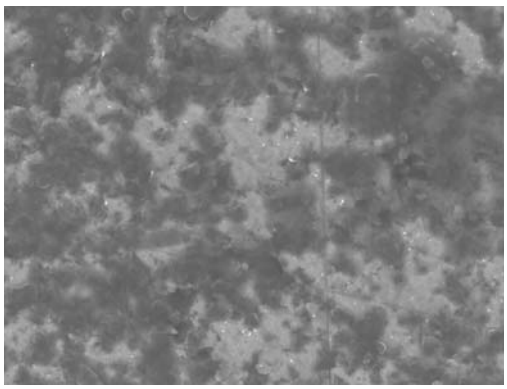

Figure 5-5 - Close-up of the reactive layer before sample polishing. It shows that the reaction is preferential in specific areas, while others remain apparently unchanged.

5.1.3.2 TEM

Observation of sample C7 under TEM was greatly affected by the existence of a contamination layer over the microstructure. This is a similar effect to the one reported during SEM discussion, most likely with the same origin. The reason why this sample was affected while sample B3 was not, is probably due to the fact that the latter was taken from the ion milling machine and immediately taken for TEM observation. The ion beam chamber is under high vacuum and the ion beam itself must have successfully removed any contamination around the observable area, near the puncture.

Oxidation of the surfaces, hydration or a combination of both, particularly in Mg-rich areas, were taken as possible explanations and although contamination appears to be a very thin superficial film, low angle X-ray diffraction was able to indicate the presence of an oxyhydroxy phase - $MgBO_2(OH)$. As presented in the previous chapter, this phase was only detected in the last three samples of set C in which sample C7 is included. It is therefore quite possible that the layer seen during TEM observation of this sample corresponds to this oxyhydroxyde. Previously observed sample B3 did not show any signs of this effect. It is quite reasonable to assume that the extra magnesium, also detected in low-angle XRD analysis, explains the existence of the oxyhydroxyde phase in these samples. The magnesium makes these samples prone to oxidation and hydration of their surfaces. However, definitive conclusions regarding the exact composition of the superficial layer were not possible due to a set of limitations regarding the techniques available and the chemical nature of the contamination itself:

- the oxyhydroxylized layer is very thin;
- oxyhydroxydes are amorphous to a certain degree;
- Low-angle diffraction technique is very sensitive to surface topography;

- EDS techniques are particularly limited in the case of low atomic weight elements.

MgO particles, perfectly identifiable by EDS analysis, were again found in this sample in the form of isolated grains and precipitates. Although, as stated in chapter 4, at times precipitates gave the impression of being inside MgB_x grains, analyses during observation lead to a different conclusion. If the precipitates were in deed growing inside the grains, strain lines due to lattice distortion surrounding them should be visible. Figure 5-6 shows an MgB_x grain very clearly, without any observable lattice distortion effects. Moreover the motion of the dislocation lines inside the bottom grain, while tilting the sample during observation, was smooth and continuous, further supporting that there is no precipitation of MgO inside MgB_x grains.

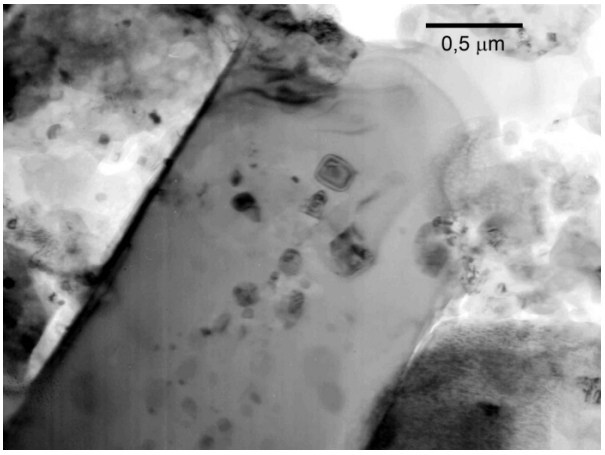

Figure 5-6 – Micrograph displaying an MgB_x grain with isolated MgO precipitates as well as grains, over it.

5.2 *In situ*

This set of samples was an attempt to synthesize MgB_2 from precursor powders under vacuum conditions. Boron and magnesium have quite different melting temperatures. While magnesium melts at 650 °C, melting point for boron is 2076 °C. Based on the results found in reference [38], magnesium melts at a slightly lower temperature than the MgB_2 formation temperature - roughly 50 °C higher (Figure 5-7). This has two implications on the process: the synthesis of the superconducting phase occurs by liquid-phase sintering; high amounts of magnesium will be lost by evaporation during sintering and will not react with boron. While the presence of liquid phase is usually helpful for densification, for promoting reaction and in shortening sintering times, it is detrimental in this specific case for all the reasons already presented.

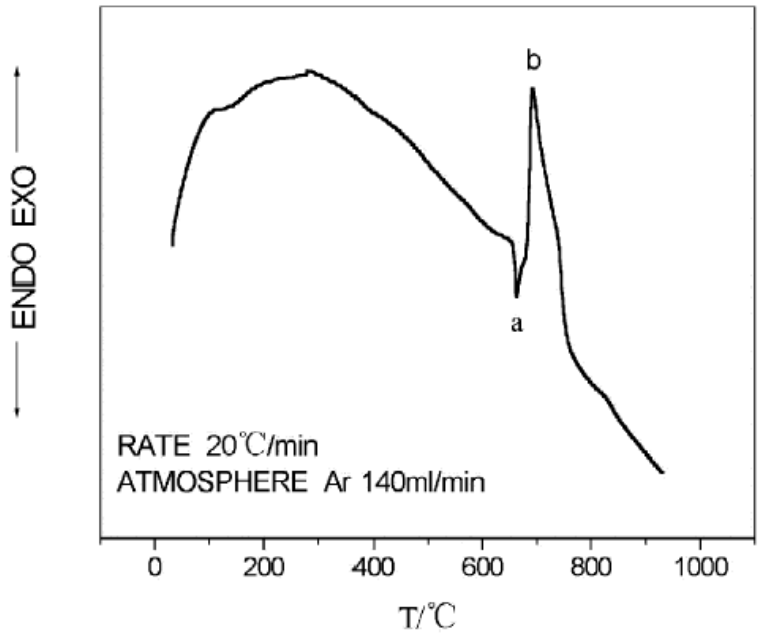

Figure 5-7 – Curve obtained by differential thermal analysis of a mixture of magnesium and boron powders (Mg:B = 1:2) showing one endothermic (a) and an exothermic (b) peak. These correspond to the melting point of magnesium and formation of MgB_2 phase, respectively.

The results have shown that the samples lose weight and expand during thermal treatment. These effects contribute to a decrease in sample density after processing, the reasons being two-fold. Weight loss is associated with the amount of magnesium lost by evaporation at processing temperature. In fact, weight loss is aggravated with increasing amounts of magnesium in the initial mixture. Average weight losses are 10%, 17% and 26% for samples of compositions A, B and C, respectively. Results also show that samples have expanded during sintering. Although formation of MgB_2 has been associated with an

expansion, this relation is not obvious with these results due to high amounts of porosity in resulting samples which influence the analysis.

XRD performed in all *in situ* processed samples has shown two crystalline phases present: MgB_2 and MgO. No MgB_4 was formed at this temperature. One must bear in mind that boron used was amorphous and thus cannot be detected by XRD. Amorphous boron was preferable to crystalline because, being in a metastable state, it is more reactive. Given the results and the fact that melting point of boron is much higher than the sintering temperature, there must be boron still present in all samples. This leads to some complications when determining relative phase composition. Even so, by determining the amounts of MgB_2 and MgO present, it is possible to evaluate the amount of superconducting phase relatively to the amount of periclase created during sintering. The average MgB_2/MgO ratios for each set can be seen in the next table.

Table 5-3 – MgB_2 and MgO volume fraction ratios for *in situ* samples.

Set	MgB_2 / MgO ratio
A	14
B	38
C-a	2
C-b	26

Under the processing conditions, composition B samples have resulted better both in terms of final relative density as in terms of the amount of superconducting phase obtained relatively to the amount of MgO. For all samples except those in capsule C-a, the amount of MgO was limited to a maximum value of 3 (wt. %). Another important aspect revealed with these results is the role played by the capsules during thermal treatment. Encapsulation effectively hinders the oxidation of magnesium. Samples in capsule C-a which were exposed inside the furnace chamber, have roughly 9 times the amount of MgO than those in capsule C-b. The effect of encapsulation on sample densification is minimum. The initial powder composition doesn't affect the amount of MgB_2 formed during sintering, because it doesn't stop magnesium to be released from the sample.

SEM micrographs show a highly porous structure with denser grains embedded. These grains are aligned perpendicularly to the direction of pressing. This means that packing of the initial powders plays a role in the densification of the samples. EDS is ineffective in detecting differences in chemical composition for these samples. The microstructures of these samples are completely different from the ones processed *ex situ*. The interconnection between grains is severely weak due to the high amounts of porosity caused by the absence of external pressure during sintering stage.

5.3 Electric and Magnetic properties

Parallel to the work presented in this thesis, the physical characterization of the samples was performed. This characterization was focused on the electrical and magnetic properties, in order to evaluate the superconducting performance of the samples. A summary of the most relevant results obtained are presented on Table 5-4, together with sample density values and phase composition. Transport measurements were made using conventional four point probe set-up. Magnetic measurements were obtained using a SQUID magnetometer.

Table 5-4 – Results from the magnetic characterization of the samples. Density, and phase composition results for all samples were included.

Sample	ρ (g/cm^3)	MgB_2 (wt. %)	MgO (wt. %)	MgB_4 (wt. %)	T_c (K)	ΔT_c (K)	J_c (x10^6 A/cm^2)		
							0 K	10 K	20 K
A1	88	75	17	8	36.40	0.9	----	----	----
B2	88.9	84	12	4	36.64	0.5	1.22	0.91	0.59
B3	87.5	80	12	8	36.98	0.5	0.50	0.37	0.25
B4	88.2	81	13	6	37.00	0.4	5.03	3.89	2.74
B5	90.2	78	14	8	37.18	0.3	0.38	0.29	0.2
C6	90.6	77	15	8	37.03	0.6	2.19	1.67	1.14
C7	94.4	79	13	8	36.92	0.5	2.88	2.2	1.51
C8	98.4	89	11	0	36.30	0.4	0.80	0.6	0.39
C9	98.2	86	13	0	36.39	0.5	----	----	----

Caption:
ρ - relative density
T_c – critical transition temperature (from transport measurements)
ΔT_c – transition width (from magnetic measurements)
J_c – critical current density (from magnetic measurements); values at 0K were obtained by extrapolation

Figure 5-8 shows the critical current Jc at zero magnetic field determined using the usual procedure, from the Bean critical state model[173], by accounting the magnetic irreversibility, ΔM, at a given magnetic field, and sample size, considering a long parallelepiped of section $2a$ x $2b$, according to Equation 5-1.

$$J_c(H) = \frac{10\Delta M}{a\left(1 - \frac{a}{3b}\right)}$$

Equation 5-1

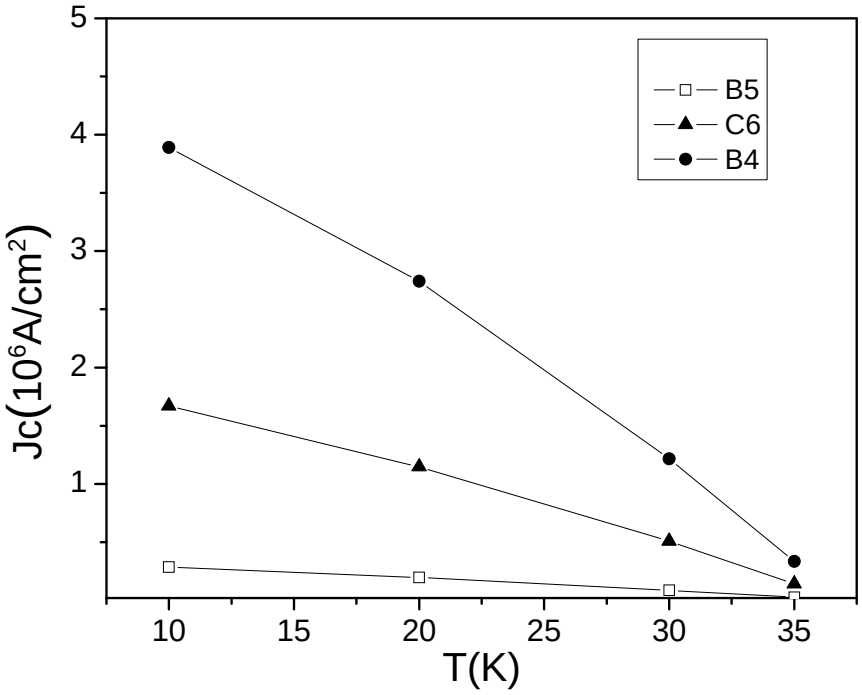

Figure 5-8 – Critical current (J_c) at zero magnetic field as a function of temperature for samples B4, B5 and C6.

The range of T_c values is relatively narrow - between 36.40 (sample A1) and 37.18 K (sample B5) for all samples. The transition temperature range is considerably low, ~0.5 K, corresponding to very sharp transitions both in transport (Figure 5-9) as well as in magnetic measurements (Figure 5-10). Such low transition width values are common in MgB_2 samples[38, 174-178]. J_c values measured at zero field and 10 K have a minimum of 0.6×10^6 in sample C8, and a maximum of 3.89×10^6 A/cm^2 for sample B4.

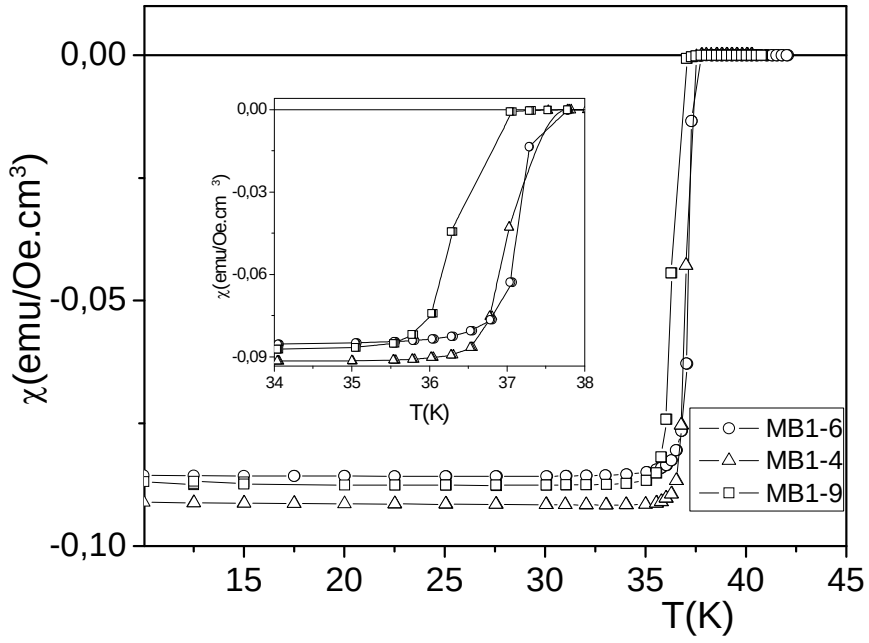

Figure 5-9 – Temperature dependence of the magnetic susceptibility. Inset: detail near Tc.

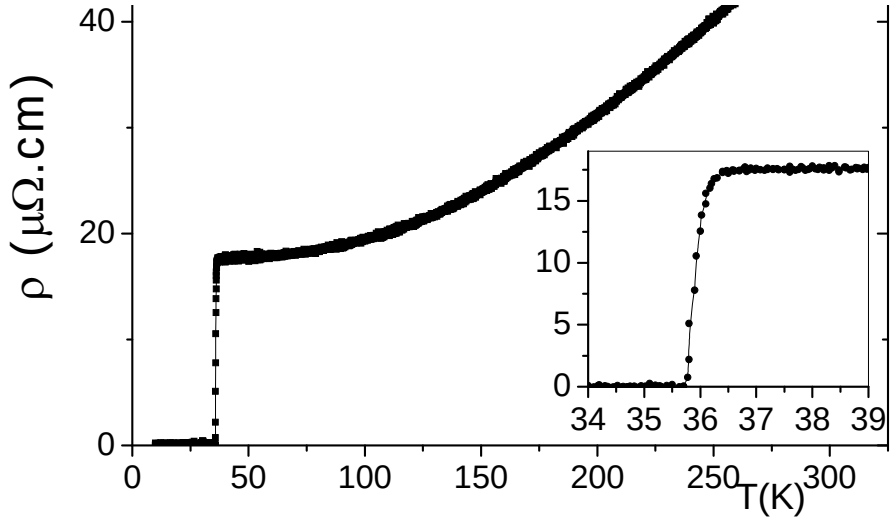

Figure 5-10 – Temperature dependence of the electrical resistivity of sample B3. Inset: detail near Tc.

The values obtained for T_c obtained through transport measurements are very similar for all samples. The difference between the highest and the lowest values is no greater than 1K, despite the microstructural and chemical differences between the samples. On the other hand the dispersion of J_c values is much greater. This is a consequence of the principles underlying each technique. While transport measurements are a function of the path taken by the intergranular currents, magnetic measurements are a function of both the inter and the intragranular currents generated during the experiments. Considering a hypothetical sample whose microstructure is comprised of superconducting grains and where each grain is perfectly isolated from each of its neighbours with a very thin and insulating layer, both methods would provide very different results. Transport measurements would not show any transition because the current had no way to flow from grain to grain. On the other hand, magnetic measurements would indicate that the sample was in deed superconductive with superconductive phase close to 100%, provided that the insulating layer was thin enough. In practical terms transport measurements are a much better indicator of the electric conductivity of the samples and as long as there is a percolative path between the superconducting material and the T_c will not vary much. Any variation in T_c is associated with interfacial phenomena at the grain boundaries, such as the presence of second phases for instances, like the amorphous layer observed in TEM in sample C7. Jc results obtained from magnetic measurements will be more sensible to phase composition and its relative amount in the samples. But Jc results in MgB_2 samples were found to be subjected to errors if typical Bean critical state model is applied directly, as will be discussed next.

One effect observed during this study was the dependence of the magnetic properties on sample dimensions (besides demagnetizing effects). This effect has also been reported in other studies[179, 180]. Such behaviour is characteristic of an inhomogeneous current distribution inside the material, with magnetic screening at different length scales, and may also be responsible for this discrepancy. Horvat *et al.* have measured the different length scales at which superconducting currents circulate on MgB_2 samples and found them to be of ~1 μm, ~10 μm, and in the whole of the sample (in the orders of millimeters)[180] Based on these results the report states that due to the inhomogeneous structure of MgB_2, $J_c(T)$ values obtained by simply applying the critical state model will be a result of different types of screening scale length's causing and will lead to errors. These errors include the "artificial" dependence of J_c on the sample size[180].

Given the T_c and J_c results obtained, there seems to be no apparent relation between these any of the factors studied in this thesis, namely densification, processing conditions, phase composition and microstructural characteristics. For instances, sample B4 has the highest J_c with 2.74×10^6 A/cm^2 (at 20 K) but is not the sample with highest amount of superconducting phase, with 84 wt. %. On the other hand, sample C8 which does have the highest amount of MgB_2 with 89 wt. % has one of the lowest J_c values with 0.39×10^6A/cm^2. (at 20 K). As already discussed, this correlation is subjected to some errors in J_c measurements and further studies are required to reach definite conclusions.

Overall these results are consistent with previous works in HIPed MgB_2 samples[54, 55, 174, 181] presented in Chapter 2. However, our work has resulted in a combination of high sample densities, improved

mechanical properties and composition control, while maintaining the physical properties. J_c results at 0T and 20K compete with some of the best results found for doped samples, namely with those doped with Zr[129], Ti[130] and Cu[136]. Comparison of J_c with different doping elements presented in Chapter 2 is irrelevant given the different measuring conditions, specifically the applied magnetic field.

5.4 Summary

The results presented and discussed throughout this report are the result of the combination between HIP sintering and a simple encapsulation technique, which has proven to be a successful strategy in fulfilling the purposed objectives with this study. The following lists summarize the conclusions reached and recommendations for future work.

Conclusions:

- Excellent mechanical properties were attained for all *ex situ* samples due to the samples' relative density which have reached values above 98%;
- Good degree of control over the final composition was attained with superconducting phase amounts reaching values near 90%;
- MgB_4 formation was successfully avoided by adding extra magnesium to the capsules;
- Although MgO amounts was still increased during sintering, its final amount was limited to a maximum of 15 wt. % with encapsulation step, and believed to be further decreased with lower sintering temperatures; small amounts of MgO may benefit physical properties[172], controlling the processing conditions can be one way to tailor its presence;
- Good physical properties with results that are consistent with previous works using HIP and compete even with results from doped samples;
- Despite the densification problems for in situ processed samples, it has allowed us to fully realize the importance of sample encapsulation and pressure-assisted sintering.

Future work recommendations:

- Systematic study on temperature and pressure parameters to search for the optimal conditions of MgB_2 superconducting bulk samples and minimize production costs;
- Systematic study on the optimal amount of MgO in superconducting samples to enhance flux pinning effects;
- Systematic study on doping to improve magnetic behaviour of MgB_2;
- Systematic study of the sample surface alteration and possible influence on the physical properties and applications;
- EPMMA and XPS studies to fully characterize phase composition of the samples;
- Systematic study on the influence of the presence of magnesium on the phase composition and physical properties of the samples.

6 Bibliography

1. Contributors. *Heike Kamerlingh Onnes*. Wikipedia [Web Page] 2006 24 September 2006 [cited 30-09-2006].
2. Onnes, H.K., *The superconductivity of Mercury.* Leyden Communications, 1911. **122**.
3. Meissner, W. and R. Oschenfeld, *Ein neuer Effekt bei Eintritt der Supraleitfähigkeit.* Naturwissenschaften, 1933. **21**(44).
4. Gavaler, J.R., *Superconductivity in Nb-Ge Films above 22 K.* Applied Physics Letters, 1973. **23**(8): p. 480-482.
5. Bednorz, J.G. and K.A. Muller, *Possible High-Tc Superconductivity in the Ba-La-Cu-O System.* Zeitschrift Fur Physik B-Condensed Matter, 1986. **64**(2): p. 189-193.
6. Bednorz, J.G., M. Takashige, and K.A. Muller, *Susceptibility Measurements Support High-Tc Superconductivity in the Ba-La-Cu-O System.* Europhysics Letters, 1987. **3**(3): p. 379-385.
7. Wu, M.K., J.R. Ashburn, C.J. Torng, P.H. Hor, R.L. Meng, L. Gao, Z.J. Huang, Y.Q. Wang, and C.W. Chu, *Superconductivity at 93-K in a New Mixed-Phase Y-Ba-Cu-O Compound System at Ambient Pressure.* Physical Review Letters, 1987. **58**(9): p. 908-910.
8. Maeda, H., Y. Tanaka, M. Fukutomi, and T. Asano, *A New High-Tc Oxide Superconductor without a Rare-Earth Element.* Japanese Journal of Applied Physics Part 2-Letters, 1988. **27**(2): p. L209-L210.
9. Dai, P., B.C. Chakoumakos, G.F. Sun, K.W. Wong, Y. Xin, and D.F. Lu, *Synthesis and Neutron Powder Diffraction Study of the Superconductor Hgba2ca2cu3o8+Delta by Tl Substitution.* Physica C, 1995. **243**(3-4): p. 201-206.
10. Superconductors.org. *Table of known superconducting elements*. 03-01-2007 [cited 14-03-2007]; Available from: www.superconductors.org/type1.htm.
11. Abrikosov, A.A., *On the Magnetic Properties of Superconductors of the Second Group.* Soviet Physics Jetp-Ussr, 1957. **5**(6): p. 1174-1183.
12. Reimer, D. *Fundamentals of superconductors*. A Guide to Superconductivity 1996 [cited 2007-02-06]; Available from: http://www.physnet.uni-hamburg.de/home/vms/reimer/htc/pt3.html.
13. Karpinski, J., M. Angst, J. Jun, S.M. Kazakov, R. Puzniak, A. Wisniewski, J. Roos, H. Keller, A. Perucchi, L. Degiorgi, M.R. Eskildsen, P. Bordet, L. Vinnikov, and A. Mironov, *MgB2 single*

crystals: high pressure growth and physical properties. Superconductor Science & Technology, 2003. **16**(2): p. 221-230.

14. Grant, P.M., *Superconductivity and electric power: Promises, promises ... past, present and future.* Ieee Transactions on Applied Superconductivity, 1997. **7**(2): p. 112-132.
15. Bardeen, J., L.N. Cooper, and J.R. Schrieffer, *Theory of Superconductivity.* Physical Review, 1957. **108**(5): p. 1175-1204.
16. Cooper, L.N., *Bound Electron Pairs in a Degenerate Fermi Gas.* Physical Review, 1956. **104**(4): p. 1189-1190.
17. Frohlich, H., *Theory of the Superconducting State .1. The Ground State at the Absolute Zero of Temperature.* Physical Review, 1950. **79**(5): p. 845-856.
18. Bardeen, J., *Wave Functions for Superconducting Electrons.* Physical Review, 1950. **80**(4): p. 567-574.
19. Plakida, N.M., *High-Temperature Superconductivity - Experiment and theory*. 1995, Berlin: Springer.
20. Gurevich, A. and E.A. Pashitskii, *Current transport through low-angle grain boundaries in high-temperature superconductors.* Physical Review B, 1998. **57**(21): p. 13878.
21. Barnes, P.N., M.D. Sumption, and G.L. Rhoads, *Review of high power density superconducting generators: Present state and prospects for incorporating YBCO windings.* Cryogenics, 2005. **45**(10-11): p. 670-686.
22. Jones, M.E. and R.E. Marsh, *The Preparation and Structure of Magnesium Boride, Mgb2.* Journal of the American Chemical Society, 1954. **76**(5): p. 1434-1436.
23. Nagamatsu, J., N. Nakagawa, T. Muranaka, Y. Zenitani, and J. Akimitsu, *Superconductivity at 39 K in magnesium diboride.* Nature, 2001. **410**(6824): p. 63-64.
24. Gasparov, V.A., N.S. Sidorov, I.I. Zver'kova, and M.P. Kulakov, *Electron transport in diborides: Observation of superconductivity in ZrB2.* Jetp Letters, 2001. **73**(10): p. 532-535.
25. D. Kaczorowski, A.J.Z., O. J. Zogal, J. Klamut, *Incipient superconductivity in TaB_2.* Preprint, 2006. **cond-mat/0103571**.
26. Leyarovska, L. and E. Leyarovski, *Search for Superconductivity Below 1-K in Transition-Metal Borides.* Journal of the Less-Common Metals, 1979. **67**(1): p. 249-255.
27. Felner, I., *Absence of superconductivity in BeB2.* Physica C-Superconductivity and Its Applications, 2001. **353**(1-2): p. 11-13.

28. Young, D.P., R.G. Goodrich, P.W. Adams, J.Y. Chan, F.R. Fronczek, F. Drymiotis, and L.L. Henry, *Superconducting properties of BeB2.75.* Physical Review B, 2002. **65**(18): p. -.

29. Buzea, C. and T. Yamashita, *Review of the superconducting properties of MgB2.* Superconductor Science & Technology, 2001. **14**(11): p. R115-R146.

30. Cooper, A.S., Corenzwi.E, Longinot.Ld, B.T. Matthias, and Zacharia.Wh, *Superconductivity - Transition Temperature Peak Below 4 Electrons Per Atom.* Proceedings of the National Academy of Sciences of the United States of America, 1970. **67**(1): p. 313-&.

31. JCPDS - International Centre for Diffraction Data, card number 74-0982, 2000.

32. Aswal, D.K., S. Sen, A. Singh, T.V.C. Rao, J.C. Vyas, L.C. Gupta, S.K. Gupta, and V.C. Sahni, *Synthesis and characterization of MgB2 superconductor.* Physica C-Superconductivity and Its Applications, 2001. **363**(3): p. 149-154.

33. *Crystal Structure of MgB2*. 2005 [cited 2005; Available from: http://www.asc.wisc.edu/mgb2/mgb2.htm.

34. Brutti, S., A. Ciccioli, G. Balducci, G. Gigli, P. Manfrinetti, and A. Palenzona, *Vaporization thermodynamics of MgB_2 and MgB_4.* Applied Physics Letters, 2002. **80**(16): p. 2892-2894.

35. Dou, S.X., J. Horvat, S. Soltanian, X.L. Wang, M.J. Qin, S.H. Zhou, H.K. Liu, and P.G. Munroe, *Transport critical current density in Fe-sheathed nano-SiC doped MgB2 wires.* Ieee Transactions on Applied Superconductivity, 2003. **13**(2): p. 3199-3202.

36. Cook, L.P., R. Klein, W. Wong-Ng, Q. Huang, R.A. Ribeiro, and P.C. Canfield, *Thermodynamics of MgB2 - by calorimetry and Knudsen thermogravimetry.* Ieee Transactions on Applied Superconductivity, 2005. **15**(2): p. 3227-3229.

37. Balducci, G., S. Brutti, A. Ciccioli, G. Gigli, P. Manfrinetti, A. Palenzona, M.F. Butman, and L. Kudin, *Thermodynamics of the intermediate phases in the Mg-B system.* Journal of Physics and Chemistry of Solids, 2005. **66**(2-4): p. 292-297.

38. Bando, H., Y. Yamaguchi, N. Shirakawa, and T. Yanagisawa, *Anisotropy in the upper and lower critical fields of MgB2 single crystals.* Physica C-Superconductivity and Its Applications, 2004. **412-14**: p. 258-261.

39. Kito, H., Y. Takano, and K. Togano, *Superconductivity in ternary germanide Y(Pt0.5Ge1.5) with the AlB2-type structure.* Physica C-Superconductivity and Its Applications, 2002. **377**(3): p. 185-189.

40. Chen, X.L., Q.Y. Tu, L. Dai, and Y.P. Xu, *A note on the AlB2 type structure.* Modern Physics Letters B, 2002. **16**(3): p. 73-77.

41. Prikhna, T.A., W. Gawalek, Y.M. Savchuk, V.E. Moshchil, N.V. Sergienko, T. Habisreuther, M. Wendt, R. Hergt, C. Schmidt, J. Dellith, V.S. Melnikov, A. Assmann, D. Litzkendorf, and P.A. Nagorny, *High-pressure synthesis of MgB2 with addition of Ti.* Physica C-Superconductivity and Its Applications, 2004. **402**(3): p. 223-233.

42. Angst, M., R. Puzniak, A. Wisniewski, J. Roos, H. Keller, P. Miranovic, J. Jun, S.M. Kazakov, and J. Karpinski, *Anisotropy of the superconducting state properties and phase diagram of MgB2 by torque magnetometry on single crystals.* Physica C-Superconductivity and Its Applications, 2003. **385**(1-2): p. 143-153.

43. Bouquet, F., Y. Wang, I. Sheikin, P. Toulemonde, M. Eisterer, H.W. Weber, S. Lee, S. Tajima, and A. Junod, *Unusual effects of anisotropy on the specific heat of ceramic and single crystal MgB2.* Physica C-Superconductivity and Its Applications, 2003. **385**(1-2): p. 192-204.

44. Lee, S.G., J.R. Ahn, Y. Kim, S.H. Moon, K.W. Lee, I.S. Kim, and Y.K. Park, *Properties of MgB2 thin films made by radio frequency magnetron co-sputtering.* Superconductor Science & Technology, 2003. **16**(12): p. 1550-1553.

45. Jung, C.U., M.S. Park, W.N. Kang, M.S. Kim, S.Y. Lee, and S.I. Lee, *Temperature- and magnetic-field-dependent resistivity of MgB2 sintered at high-temperature and high-pressure condition.* Physica C-Superconductivity and Its Applications, 2001. **353**(3-4): p. 162-166.

46. Kalavathi, S. and C. Divakar, *Superconductivity in dense Mg1-xMxB2 (M =Zr, Nb, Mo; x=0.05) materials sintered under pressure.* Bulletin of Materials Science, 2005. **28**(3): p. 249-252.

47. Kolesnikov, N.N. and M.P. Kulakov, *Synthesis of MgB2 from elements.* Physica C-Superconductivity and Its Applications, 2001. **363**(3): p. 166-169.

48. Fujii, H., H. Kumakura, and K. Togano, *Influence of MgB2 powder quality on the transport properties of Cu-sheathed MgB2 tapes.* Physica C-Superconductivity and Its Applications, 2001. **363**(4): p. 237-242.

49. Abe, H., M. Naito, K. Nogi, M. Matsuda, M. Miyake, S. Ohara, A. Kondo, and T. Fukui, *Low temperature formation of superconducting MgB2 phase from elements by mechanical milling.* Physica C-Superconductivity and Its Applications, 2003. **391**(2): p. 211-216.

50. Asthana, A., C. Shekhar, R. Giri, and O.N. Srivastava, *Improved superconducting properties of MgB2 bulk materials prepared by sintering.* Journal of Physics D-Applied Physics, 2003. **36**(17): p. 2165-2169.

51. Du, W., H.Z. Xu, H.B. Zhang, D. Xu, X.Q. Wang, X.Q. Hou, Y.Z. Wu, F.Y. Jiang, and L.J. Qin, *Single crystal growth of MgB2 by evaporating Mg-flux method.* Journal of Crystal Growth, 2006. **289**(2): p. 626-629.

52. Talapatra, A., S.K. Bandyopadhyay, P. Sen, A. Sarkar, and P. Barat, *Phase formation of superconducting MgB2 at ambient pressure.* Bulletin of Materials Science, 2004. **27**(5): p. 429-432.

53. Ghigo, G., D. Botta, A. Chiodoni, R. Gerbaldo, L. Gozzelino, F. Laviano, E. Mezzetti, B. Minetti, G. Giunchi, and S. Ceresara, *Pinning energy and vortex-phase diagram of MgB2 bulk materials.* International Journal of Modern Physics B, 2003. **17**(4-6): p. 584-589.

54. Frederick, N.A., S. Li, M.B. Maple, V.F. Nesterenko, and S.S. Indrakanti, *Improved superconducting properties of MgB2.* Physica C-Superconductivity and Its Applications, 2001. **363**(1): p. 1-5.

55. Shields, T.C., K. Kawano, D. Holdom, and J.S. Abell, *Microstructure and superconducting properties of hot isostatically pressed MgB2.* Superconductor Science & Technology, 2002. **15**(2): p. 202-205.

56. Klie, R.F., J.C. Idrobo, N.D. Browning, A. Serquis, Y.T. Zhu, X.Z. Liao, and F.M. Mueller, *Observation of coherent oxide precipitates in polycrystalline MgB2.* Applied Physics Letters, 2002. **80**(21): p. 3970-3972.

57. Civale, L., A. Serquis, D.L. Hammon, X.Z. Liao, J.Y. Coulter, Y.T. Zhu, T. Holesinger, D.E. Peterson, and F.M. Mueller, *High critical currents in powder in tube MgB2 wires: Influence of microstructure and heat treatments.* Ieee Transactions on Applied Superconductivity, 2003. **13**(2): p. 3347-3350.

58. Ahn, J.R., S.G. Lee, Y.S. Hwang, G.Y. Sung, and D.K. Kim, *Fabrication of MgB2 thin film by rf magnetron sputtering.* Physica C-Superconductivity and Its Applications, 2003. **388**: p. 127-128.

59. Dou, S.X., S. Soltanian, J. Horvat, X.L. Wang, S.H. Zhou, M. Ionescu, H.K. Liu, P. Munroe, and M. Tomsic, *Enhancement of the critical current density and flux pinning of MgB2 superconductor by nanoparticle SIC doping.* Applied Physics Letters, 2002. **81**(18): p. 3419-3421.

60. Senkowicz, B.J., J.E. Giencke, S. Patnaik, C.B. Eom, E.E. Hellstrom, and D.C. Larbalestier, *Improved upper critical field in bulk-form magnesium diboride by mechanical alloying with carbon.* Applied Physics Letters, 2005. **86**(20): p. -.

61. Canfield, P.C., D.K. Finnemore, S.L. Bud'ko, J.E. Ostenson, G. Lapertot, C.E. Cunningham, and C. Petrovic, *Superconductivity in dense MgB2 wires.* Physical Review Letters, 2001. **86**(11): p. 2423-2426.

62. Bar-Sadan, M., G. Leitus, and S. Reich, *Weak links and phase slip centers in superconducting MgB2 wires.* Journal of Superconductivity, 2004. **17**(4): p. 497-502.

63. Higashikawa, K., T. Nakamura, K. Osamura, M. Takahashi, and M. Okada, *Switching characteristics of MgB2 wires subjected to transient application of magnetic field.* Physica C-Superconductivity and Its Applications, 2005. **426**: p. 1261-1266.

64. Gencer, A., A. Kilic, N. Guclu, L. Ozyuzer, and I. Belenli, *Low-field behavior of Ti-added MgB2/Cu superconducting wires.* Ieee Transactions on Applied Superconductivity, 2005. **15**(2): p. 3352-3355.

65. Glowacki, B.A., M. Majoros, M. Eisterer, S. Toenies, H.W. Weber, M. Fukutomi, K. Komori, and K. Togano, *MgB2 superconductors for applications.* Physica C-Superconductivity and Its Applications, 2003. **387**(1-2): p. 153-161.

66. Martinez, E., L.A. Angurel, and R. Navarro, *Study of Ag and Cu/MgB2 powder-in-tube composite wires fabricated by in situ reaction at low temperatures.* Superconductor Science & Technology, 2002. **15**(7): p. 1043-1047.

67. Martinez, E., L.A. Angurel, R. Navarro, A. Millan, C. Rillo, and M. Artigas, *Study of MgB2 powders and Cu/MgB2 powder-in-tube composite wires with Zn addition.* Ieee Transactions on Applied Superconductivity, 2003. **13**(2): p. 3210-3213.

68. Maeda, M., K. Mizuno, A. Takashi, D. Uchiyama, T. Kawakami, H. Kobayashi, K. Yasohama, and Y. Kubota, *Crystal growth and critical current densities of polycrystalline MgB2 superconductor.* Ieee Transactions on Applied Superconductivity, 2005. **15**(2): p. 3300-3303.

69. Pachla, W., A. Presz, R. Diduszko, P. Kovac, and I. Husek, *Structural inhomogeneity of superconducting ex situ MgB2/CU wires made by the powder-in-tube technique.* Superconductor Science & Technology, 2002. **15**(9): p. 1281-1287.

70. Chen, C.P., X.F. Wang, Y. Lu, Z. Jia, J.P. Guo, X.N. Wang, M. Zhu, X.Y. Xu, J. Xu, and Q.R. Feng, *Thick MgB2 film with (101) oriented micro-crystals.* Physica C-Superconductivity and Its Applications, 2004. **416**(3-4): p. 90-94.

71. Xiao, H., W.H. Song, J.J. Du, Y.P. Sun, and J. Fang, *Preparation and superconductivity of MgB2/Cu tapes.* Physica C-Superconductivity and Its Applications, 2003. **386**: p. 593-597.

72. Lezza, P., R. Gladyshevskii, C. Senatore, G. Cusanelli, H.L. Suo, and R. Flukiger, *Anisotropy of J(c) in ex situ MgB2/Fe monofilamentary tapes.* Ieee Transactions on Applied Superconductivity, 2005. **15**(2): p. 3196-3199.

73. Kovac, P., I. Husek, and T. Melisek, *Transport currents of two-axially rolled and post-annealed MgB2/Fe wires at 4.2 K.* Superconductor Science & Technology, 2002. **15**(9): p. 1340-1344.

74. Flukiger, R., H.L. Suo, N. Musolino, C. Beneduce, P. Toulemonde, and P. Lezza, *Superconducting properties of MgB2 tapes and wires.* Physica C-Superconductivity and Its Applications, 2003. **385**(1-2): p. 286-305.

75. Cheng, C.H., H. Zhang, Y. Zhao, Y. Feng, X.F. Rui, P. Munroe, H.M. Zeng, N. Koshizuka, and M. Murakami, *Doping effect of nano-diamond on superconductivity and flux pinning in MgB2.* Superconductor Science & Technology, 2003. **16**(10): p. 1182-1186.

76. Feng, Y., G. Yan, Y. Zhao, C.F. Liu, B.Q. Fu, L. Zhou, L.Z. Cao, K.Q. Ruan, X.G. Li, L. Shi, and Y.H. Zhang, *Superconducting properties of MgB2 wires and tapes with different metal sheaths.* Physica C-Superconductivity and Its Applications, 2003. **386**: p. 598-602.

77. Balamurugan, S., T. Nakamura, K. Osamura, I. Muta, and T. Hoshino, *Structural and superconducting properties of PIT processed sintered MgB2/Fe wires.* Physica C-Superconductivity and Its Applications, 2004. **412-14**: p. 1184-1188.

78. Fang, H., P. Gijavanekar, Y.X. Zhou, P.T. Putman, and K. Salama, *Development of Fe-sheathed MgB2 wires and tapes for electric power applications.* Ieee Transactions on Applied Superconductivity, 2005. **15**(2): p. 3200-3203.

79. Grivel, J.C., R. Pinholt, N.H. Andersen, P. Kovac, I. Husek, and J. Homeyer, *In situ investigations of phase transformations in Fe-sheathed MgB2 wires.* Superconductor Science & Technology, 2006. **19**(1): p. 96-101.

80. Braccini, V., D. Nardelli, A. Malagoli, A. Tumino, C. Fanciulli, C. Bernini, A.S. Siri, and G. Grasso, *MgB2 tapes with non-magnetic sheath: Effect of the sintering temperature on the superconducting properties.* Ieee Transactions on Applied Superconductivity, 2005. **15**(2): p. 3211-3214.

81. Bellingeri, E., A. Malagoli, M. Modica, V. Braccini, A.S. Siri, and G. Grasso, *Neutron scattering studies of superconducting MgB2 tapes.* Superconductor Science & Technology, 2003. **16**(2): p. 276-280.

82. Katagiri, K., A. Iwamoto, Y. Shoji, K. Tachikawa, Y. Yamada, K. Watanabe, and T. Mito, *Stress/strain characteristics of PIT MgB2 tapes with nickel sheath-effect of indium addition to the core.* Physica C-Superconductivity and Its Applications, 2003. **397**(3-4): p. 95-98.

83. Katagiri, K., R. Takaya, K. Tachikawa, Y. Yamada, A. Iwamoto, and K. Watanabe, *Stress/strain characteristics of PIT MgB2 tapes with Ni sheath.* Journal of the Japan Institute of Metals, 2004. **68**(9): p. 642-647.

84. Grovenor, C.R.M., L. Goodsir, C.J. Salter, P. Kovac, and I. Husek, *Interfacial reactions and oxygen distribution in MgB2 wires in Fe, stainless steel and Nb sheaths.* Superconductor Science & Technology, 2004. **17**(3): p. 479-484.

85. Berenov, A., A. Serquis, X.Z. Liao, Y.T. Zhu, D.E. Peterson, Y. Bugoslavsky, K.A. Yates, M.G. Blamire, L.F. Cohen, and J.L. MacManus-Driscoll, *Enhancement of critical current density in low level Al-doped MgB2.* Superconductor Science & Technology, 2004. **17**(10): p. 1093-1096.

86. Serquis, A., L. Civale, D.L. Hammon, G. Serrano, and V.F. Nesterenko, *Optimization of critical currents in MgB2 wires and coils.* Ieee Transactions on Applied Superconductivity, 2005. **15**(2): p. 3188-3191.

87. Badica, P., K. Togano, S. Awaji, and K. Watanabe, *Growth of superconducting MgB2 films by pulsed-laser deposition using a Nd-YAG laser.* Superconductor Science & Technology, 2006. **19**(2): p. 242-246.

88. Bugoslavsky, Y., L. Cowey, T.J. Tate, G.K. Perkins, J. Moore, Z. Lockman, A. Berenov, J.L. MacManus-Driscoll, A.D. Caplin, L.F. Cohen, H.Y. Zhai, H.M. Christen, M.P. Paranthaman, D.H. Lowndes, M.H. Jo, and M.G. Blamire, *Effective vortex pinning in MgB2 thin films.* Superconductor Science & Technology, 2002. **15**(10): p. 1392-1397.

89. Ferdeghini, C., V. Ferrando, G. Grassano, W. Ramadan, E. Bellingeri, V. Braccini, D. Marre, P. Manfrinetti, A. Palenzona, F. Borgatti, R. Felici, and T.L. Lee, *Growth of c-oriented MgB2 thin films by pulsed laser deposition: structural characterization and electronic anisotropy.* Superconductor Science & Technology, 2001. **14**(11): p. 952-957.

90. Heinrich, A., C. Leirer, and B. Stritzker, *Pulsed laser deposition of MgB2 films with high critical temperatures.* Superconductor Science & Technology, 2005. **18**(9): p. 1215-1217.

91. Hikita, Y., T. Fukumura, T. Ito, M. Kawasaki, and H. Takagi, *Fabrication of MgB2 thin film on boride substrates by pulsed laser deposition.* Journal of Low Temperature Physics, 2003. **131**(5-6): p. 1187-1191.

92. Mijatovic, D., A. Brinkman, H. Hilgenkamp, H. Rogalla, G. Rijnders, and D.H.A. Blank, *Pulsed-laser deposition of MgB2 and B thin films.* Applied Physics a-Materials Science & Processing, 2004. **79**(4-6): p. 1243-1246.

93. Rogai, R., V. Galluzzi, A. Mancini, G. Celentano, T. Petrisor, A. Rufoloni, E. Varesi, G. Grassano, V. Boffa, and U. Gambardella, *Growth of MgB2 thin films by means of in situ deposition techniques.* International Journal of Modern Physics B, 2003. **17**(4-6): p. 703-708.

94. Liu, S., K.h. Xu, and M. Wang, *Preparation of Co powders for cemented carbides in China.* International Journal of Refractory Metals and Hard Materials, 2006. **24**(6): p. 405-412.

95. Akimitsu, J., S. Akutagawa, K. Kawashima, and T. Muranaka, *Superconductivity in MgB2 and its related materials.* Progress of Theoretical Physics Supplement, 2005(159): p. 326-337.

96. Schiestel, S., C.A. Carosella, J.S. Horwitz, M. Osofsky, C. Kendziora, S.B. Qadri, and D.L. Knies, *Ion beam assisted deposition of superconducting MgB2 thin films.* Surface & Coatings Technology, 2002. **158**: p. 203-207.

97. Lee, S., T. Masui, A. Yamamoto, H. Uchiyama, and S. Tajima, *Crystal growth of C-doped MgB2 superconductors: accidental doping and inhomogeneity.* Physica C-Superconductivity and Its Applications, 2004. **412-14**: p. 31-35.

98. Harada, N., O. Miura, H. Takemasa, Y. Hino, and D. Ito, *Superconducting properties and heat treatment condition on in-situ PIT MgB2 tapes made from Mg flakes.* Physica C-Superconductivity and Its Applications, 2006. **445**: p. 788-792.

99. Ueda, S., J. Shimoyama, A. Yamamoto, Y. Katsura, I. Iwayama, S. Horii, and K. Kishio, *Flux pinning properties of impurity doped MgB2 bulks synthesized by diffusion method.* Physica C-Superconductivity and Its Applications, 2005. **426**: p. 1225-1230.

100. Harada, Y., M. Uduka, Y. Nakanishi, N. Yoshimoto, and M. Yoshizawa, *Synthesis of as-grown superconducting MgB2 thin films by molecular beam epitaxy in UHV conditions.* Physica C-Superconductivity and Its Applications, 2004. **412-14**: p. 1383-1386.

101. Macovez, R., C. Cepek, M. Sancrotti, A. Goldoni, L. Petaccia, R. Larciprete, and S. Lizzit, *Ultra-high-vacuum epitaxial growth of MgB2(0001) thin films on Mg(0001) via molecular beam epitaxy.* Journal of Physics-Condensed Matter, 2004. **16**(33): p. S3451-S3458.

102. Maglione, M.G., F. Chiarella, R. Di Capua, R. Vaglio, M. Salvato, L. Maritato, and S.L. Prischepa, *High quality fully in-situ MgB2 thin films obtained by DC magnetron sputtering.* International Journal of Modern Physics B, 2003. **17**(4-6): p. 779-784.

103. Badica, P., T. Kondo, T. Kudo, Y. Nakamori, S. Orimo, and K. Togano, *Magnetization measurements on Li2Pd3B superconductor.* Applied Physics Letters, 2004. **85**(19): p. 4433-4435.

104. Yates, K.A., G. Burnell, N.A. Stelmashenko, J.L.M. Driscoll, and M.G. Blamire, *MgB2 thin film growth and characterisation.* Thermec'2003, Pts 1-5, 2003. **426-4**: p. 3379-3384.

105. Akinaga, M., *Synthesis of As-grown superconducting MgB2 thin films by sputtering method.* Cryogenics, 2003. **43**(10-11): p. 567-570.

106. Kuhberger, M., G. Gritzner, R. Fuger, M. Eisterer, S. Tonies, and H.W. Weber, *Superconducting MgB2 films on MgO substrates.* Applied Physics a-Materials Science & Processing, 2005. **80**(1): p. 127-129.

107. Cava, R.J., H.W. Zandbergen, and K. Inumaru, *The substitutional chemistry of MgB2.* Physica C-Superconductivity and Its Applications, 2003. **385**(1-2): p. 8-15.

108. Balaselvi, S.J., N. Gayathri, A. Bharathi, V.S. Sastry, and Y. Hariharan, *Peculiarities in the carbon substitution of MgB2.* Physica C-Superconductivity and Its Applications, 2004. **407**(1-2): p. 31-38.

109. Bharathi, A., Y. Hariharan, J. Balaselvi, and C.S. Sundar, *Superconductivity in MgB2: Phonon modes and influence of carbon doping.* Sadhana-Academy Proceedings in Engineering Sciences, 2003. **28**: p. 263-272.

110. Hol'anova, Z., J. Kacmarcik, P. Szabo, P. Samuely, I. Sheikin, R.A. Ribeiro, S.L. Bud'ko, and P.C. Canfield, *Critical fluctuations in the carbon-doped magnesium diboride.* Physica C-Superconductivity and Its Applications, 2004. **404**(1-4): p. 195-199.

111. Kasinathan, D., K.W. Lee, and W.E. Pickett, *On heavy carbon doping of MgB2.* Physica C-Superconductivity and Its Applications, 2005. **424**(3-4): p. 116-124.

112. Mickelson, W., J. Cumings, W.Q. Han, and A. Zettl, *Effects of carbon doping on superconductivity in magnesium diboride.* Physical Review B, 2002. **65**(5): p. -.

113. Paranthaman, M., J.R. Thompson, and D.K. Christen, *Effect of carbon-doping in bulk superconducting MgB2 samples.* Physica C-Superconductivity and Its Applications, 2001. **355**(1-2): p. 1-5.

114. Pogrebnyakov, A.V., X.X. Xi, J.M. Redwing, V. Vaithyanathan, D.G. Schlom, A. Soukiassian, S.B. Mi, C.L. Jia, J.E. Giencke, C.B. Eom, J. Chen, Y.F. Hu, Y. Cui, and Q. Li, *Properties of MgB2 thin films with carbon doping.* Applied Physics Letters, 2004. **85**(11): p. 2017-2019.

115. Avdeev, M., J.D. Jorgensen, R.A. Ribeiro, S.L. Bud'ko, and P.C. Canfield, *Crystal chemistry of carbon-substituted MgB2.* Physica C-Superconductivity and Its Applications, 2003. **387**(3-4): p. 301-306.

116. Singh, P.P., *Electron-phonon interaction in NbB2: a comparison with MgB2.* Solid State Communications, 2003. **125**(6): p. 323-326.

117. Kim, J.H., W.K. Yeoh, M.J. Qin, X. Xu, and S.X. Dou, *The doping effect of multiwall carbon nanotube on MgB2/Fe superconductor wire.* Journal of Applied Physics, 2006. **100**(1): p. -.

118. Cimberle, M.R., M. Novak, P. Manfrinetti, and A. Palenzona, *Magnetic characterization of sintered MgB2 samples: effect of substitution or 'doping' with Li, Al and Si.* Superconductor Science & Technology, 2002. **15**(1): p. 43-47.

119. de la Pena, O., A. Aguayo, and R. de Coss, *Effects of Al doping on the structural and electronic properties of Mg1-xAlxB2.* Physical Review B, 2002. **66**(1): p. -.

120. Klein, T., L. Lyard, J. Marcus, C. Marcenat, P. Szabo, Z. Hol'anovo, P. Samuely, B.W. Kang, H.J. Kim, H.S. Lee, H.K. Lee, and S.I. Lee, *Influence of Al doping on the critical fields and gap values in magnesium diboride single crystals.* Physical Review B, 2006. **73**(22): p. -.

121. Li, Z.Z., Y. Xuan, H.J. Tao, P.S. Luo, Z.A. Ren, G.C. Che, B.R. Zhao, and Z.X. Zhao, *Josephson tunneling in MgB2 break junctions.* Physica C-Superconductivity and Its Applications, 2002. **370**(1): p. 1-5.

122. Margadonna, S., K. Prassides, I. Arvanitidis, M. Pissas, G. Papavassiliou, and A.N. Fitch, *Crystal structure of the Mg1-xAlxB2 superconductors near x approximate to 0.5.* Physical Review B, 2002. **66**(1): p. -.

123. Putti, M., M. Affronte, P. Manfrinetti, and A. Palenzona, *Effects of Al doping on the normal and superconducting properties of MgB2: A specific heat study.* Physical Review B, 2003. **68**(9): p. -.

124. Rui, X.F., J. Chen, X. Chen, W. Guo, and H. Zhang, *Doping effect of nano-alumina on MgB2.* Physica C-Superconductivity and Its Applications, 2004. **412-14**: p. 312-315.

125. Xiang, J.Y., D.N. Zheng, J.Q. Li, L. Li, P.L. Lang, H. Chen, C. Dong, G.C. Che, Z.A. Ren, H.H. Qi, H.Y. Tian, Y.M. Ni, and Z.X. Zhao, *Superconducting properties and c-axis superstructure of Mg1xAlxB2.* Physical Review B, 2002. **65**(21): p. -.

126. Xiang, J.Y., D.N. Zheng, J.Q. Li, S.L. Li, H.H. Wen, and Z.X. Zhao, *Effects of Al doping on the superconducting and structural properties of MgB2.* Physica C-Superconductivity and Its Applications, 2003. **386**: p. 611-615.

127. Zambano, A.J., A.R. Moodenbaugh, and L.D. Cooley, *Effects of different reactions on composition homogeneity and superconducting properties of Al-doped MgB2.* Superconductor Science & Technology, 2005. **18**(11): p. 1411-1420.

128. Lu, H.X., H.W. Sun, G.X. Li, C.P. Chen, D.L. Yang, and X. Hu, *Microstructure and mechanical properties of Al2O3-MgB2 composites.* Ceramics International, 2005. **31**(1): p. 105-108.

129. Feng, Y., Y. Zhao, Y.P. Sun, F.C. Liu, B.Q. Fu, L. Zhou, C.H. Cheng, N. Koshizuka, and M. Murakami, *Improvement of critical current density in MgB2 superconductors by Zr doping at ambient pressure.* Applied Physics Letters, 2001. **79**(24): p. 3983-3985.

130. Cheng, C.H., Y. Zhao, L. Wang, and H. Zhang, *Preparation, structure and superconductivity of Mg1-xAgxB2.* Physica C-Superconductivity and Its Applications, 2002. **378**: p. 244-248.

131. Goto, D., T. Machi, Y. Zhao, N. Koshizuka, M. Murakami, and S. Arai, *Improvement of critical current density in MgB2 by Ti, Zr and Hf doping.* Physica C-Superconductivity and Its Applications, 2003. **392**: p. 272-275.

132. Okur, S., M. Kalkanci, M. Yavas, M. Egilmez, and L. Ozyuzer, *Microstructural and electrical characterization of Ti and Mg doped Cu-clad MgB2 superconducting wires.* Journal of Optoelectronics and Advanced Materials, 2005. **7**(1): p. 411-414.

133. Wilke, R.H.T., S.L. Bud'ko, P.C. Canfield, M.J. Kramer, Y.Q. Wu, D.K. Finnemore, R.J. Suplinskas, J.C. Marzik, and S.T. Hannahs, *Superconductivity in MgB2 doped with Ti and C.* Physica C-Superconductivity and Its Applications, 2005. **418**(3-4): p. 160-167.

134. Feng, Y., Y. Zhao, A.K. Pradhan, L. Zhou, P.X. Zhang, X.H. Liu, P. Ji, S.J. Du, C.F. Liu, Y. Wu, and N. Koshizuka, *Fabrication and superconducting properties of MgB2 composite wires by the PIT method.* Superconductor Science & Technology, 2002. **15**(1): p. 12-15.

135. Chen, S.K., K.S. Tan, B.A. Glowacki, W.K. Yeoh, S. Soltanian, J. Horvat, and S.X. Dou, *Effect of heating rates on superconducting properties of pure MgB2, carbon nanotube- and nano-SiC-doped in situ MgB2/Fe wires.* Applied Physics Letters, 2005. **87**(18): p. -.

136. Feng, W.J., T.D. Xia, T.Z. Liu, W.J. Zhao, and Z.Q. Wei, *Synthesis and properties of Mg(1-x)CuxB2 bulk obtained by self-propagating high-temperature synthesis (SHS) method at low temperature.* Physica C-Superconductivity and Its Applications, 2005. **425**(3-4): p. 144-148.

137. Beilin, V., I. Lapides, M. Roth, E. Dul'kin, E. Mojaev, A. Gerber, and O. Riss, *Rolling-induced texturing in metal-clad MgB2 tapes and magnetoresistivity anisotropy.* Journal of Applied Physics, 2006. **100**(4): p. -.

138. Soltanian, S., X.L. Wang, J. Horvat, S.X. Dou, M.D. Sumption, M. Bhatia, E.W. Collings, P. Munroe, and M. Tomsic, *High transport critical current density and large H-c2 and H-irr in nanoscale SiC doped MgB2 wires sintered at low temperature.* Superconductor Science & Technology, 2005. **18**(5): p. 658-666.

139. Medvedeva, N.I., J.E. Medvedeva, A.L. Ivanovskii, V.G. Zubkov, and A.J. Freeman, *Band structure of the superconducting MgB2 compound and modeling of related ternary systems.* Jetp Letters, 2001. **73**(7): p. 336-340.

140. Bernardini, F. and S. Massidda, *Anomalous effect of Li-Al codoping in MgB2: A simple explanation.* Physical Review B, 2006. **74**(1): p. -.

141. Monni, M., C. Ferdeghini, M. Putti, P. Manfrinetti, A. Palenzona, M. Affronte, P. Postorino, M. Lavagnini, A. Sacchetti, D. Di Castro, F. Sacchetti, C. Petrillo, and A. Orecchini, *Role of charge doping and lattice distortions in codoped Mg1-x(AlLi)(x)B-2 compounds.* Physical Review B, 2006. **73**(21): p. -.

142. Liao, X.Z., A. Serquis, Y.T. Zhu, J.Y. Huang, L. Civale, D.E. Peterson, F.M. Mueller, and H.F. Xu, *Mg(B,O)(2) precipitation in MgB2.* Journal of Applied Physics, 2003. **93**(10): p. 6208-6215.

143. Chen, S.K., M. Majoros, J.L. MacManus-Driscoll, and B.A. Glowacki, *In situ and ex situ Cu doping of MgB2.* Physica C-Superconductivity and Its Applications, 2005. **418**(3-4): p. 99-106.

144. Profeta, G., A. Continenza, A. Floris, and S. Massidda, *Cu doping effects in MgB2.* Physical Review B, 2003. **67**(17): p. -.

145. Tampieri, A., G. Celotti, S. Sprio, D. Rinaldi, G. Barucca, and R. Caciuffo, *Effects of copper doping in MgB2 superconductor.* Solid State Communications, 2002. **121**(9-10): p. 497-500.

146. Dou, S.X., S. Soltanian, W.K. Yeoh, and Y. Zhang, *Effect of nano-particle doping on the upper critical field and flux pinning in MgB2.* Ieee Transactions on Applied Superconductivity, 2005. **15**(2): p. 3219-3222.

147. Kuhberger, M. and G. Gritzner, *Effects of Sn, Co and Fe on MgB2.* Physica C-Superconductivity and Its Applications, 2002. **370**(1): p. 39-43.

148. Kuzmann, E., Z. Homonnay, Z. Klencsar, M. Kuhberger, A. Vertes, and G. Gritzner, *Local environments of iron and cobalt in doped MgB2 superconductors.* Superconductor Science & Technology, 2002. **15**(11): p. 1479-1485.

149. M'chirgui, A., F. Ben Azzouz, M. Annabi, M. Zouaoui, and M. Ben Salem, *Structure and superconductivity of Mg1-xPbxB2.* Solid State Communications, 2005. **133**(5): p. 321-325.

150. Kato, N., H. Nagao, K. Nishikawa, K. Nishidate, and K. Endo, *Possibility of superconductivity in intercalation compound related to MgB2.* International Journal of Quantum Chemistry, 2004. **96**(5): p. 457-462.

151. Sekkina, M.M.A. and K.M. Elsabawy, *Narrow range of iridium-substitution on Mg1-xIrxB2 superconductor.* Physica C-Superconductivity and Its Applications, 2003. **391**(3): p. 217-222.

152. Tampieri, A., G. Celotti, S. Sprio, R. Caciuffo, and D. Rinaldi, *Study of the sintering behaviour of MgB2 superconductor during hot-pressing.* Physica C-Superconductivity and Its Applications, 2004. **400**(3-4): p. 97-104.

153. Jiang, C.H., H. Hatakeyama, and H. Kumakura, *Effect of nanometer MgO addition on the in situ PIT processed MgB2/Fe tapes.* Physica C-Superconductivity and Its Applications, 2005. **423**(1-2): p. 45-50.

154. Alessandrini, M., H. Fang, M. Hanna, P. Putman, Y.X. Zhou, and K. Salama, *High critical current of Ti-sheathed MgB2 wires for AC and weight-critical applications.* Superconductor Science & Technology, 2006. **19**(1): p. 129-132.

155. Akune, T., H. Abe, N. Sakamoto, and Y. Matsumoto, *Magnetization and irreversibility field in powdered MgB2 superconductor.* Physica C-Superconductivity and Its Applications, 2003. **388**: p. 169-170.

156. Perner, O., W. Habler, R. Eckert, C. Fischer, C. Mickel, G. Fuchs, B. Holzapfel, and L. Schultz, *Effects of oxide particle addition on superconductivity in nanocrystalline MgB2 bulk samples.* Physica C-Superconductivity and Its Applications, 2005. **432**(1-2): p. 15-24.

157. Delfany, A., X.L. Wang, S. Soltanian, J. Horvat, H.K. Liu, and S. Dou, *Nano-sized Al2O3 doping effects on the critical current density of MgB2 superconductors.* Ceramics International, 2004. **30**(7): p. 1581-1583.

158. Ahn, K., R.K. Kremer, A. Simon, W.G. Marshall, P. Puschnig, and C. Ambrosch-Draxl, *Influence of pressure on the structure and electronic properties of the layered superconductor Y2C2I2.* Journal of Physics-Condensed Matter, 2005. **17**(40): p. S3121-S3130.

159. Caplin, A.D., Y. Bugoslavsky, L.F. Cohen, L. Cowey, J. Driscoll, J. Moore, and G.K. Perkins, *Critical fields and critical currents in MgB2.* Superconductor Science & Technology, 2003. **16**(2): p. 176-182.

160. Lyard, L., P. Samuely, P. Szabo, C. Marcenat, T. Klein, K.H.P. Kim, C.U. Jung, H.S. Lee, B. Kang, S. Choi, S.I. Lee, L. Paulius, J. Marcus, S. Blanchard, A.G.M. Jansen, U. Welp, G. Karapetrov, and W.K. Kwok, *Upper critical magnetic fields in single crystal MgB2.* Superconductor Science & Technology, 2003. **16**(2): p. 193-198.

161. de Lima, O.F., C.A. Cardoso, R.A. Ribeiro, M.A. Avila, and A.A. Coelho, *Angular dependence of the bulk nucleation field Hc2 of aligned MgB2 crystallites.* Physical Review B, 2001. **6414**(14): p. -.

162. Eltsev, Y., *Resistive behavior and magnetic phase diagram of MgB2 single crystals.* Physica C-Superconductivity and Its Applications, 2003. **385**(1-2): p. 162-168.

163. Eisterer, M., M. Zehetmayer, S. Tonies, H.W. Weber, M. Kambara, N.H. Babu, D.A. Cardwell, and L.R. Greenwood, *Neutron irradiation of MgB2 bulk superconductors.* Superconductor Science & Technology, 2002. **15**(2): p. L9-L12.

164. Krutzler, C., M. Zehetmayer, M. Eisterer, H.W. Weber, N.D. Zhigadlo, J. Karpinski, and A. Wisniewski, *Anisotropic reversible mixed-state properties of superconducting carbon-doped Mg(B1-xCx)(2) single crystals.* Physical Review B, 2006. **74**(14): p. -.

165. Kiuchi, M., H. Mihara, K. Kimura, T. Haraguchi, E.S. Otabe, T. Matsushita, A. Yamamoto, J. Shimoyama, and K. Kishio, *Critical current characteristics in MgB2 bulks.* Physica C-Superconductivity and Its Applications, 2006. **445**: p. 474-477.

166. Hata, S., T. Yoshidome, H. Sosiati, Y. Tomokiyo, N. Kuwano, A. Matsumoto, H. Kitaguchi, and H. Kumakura, *Microstructures of MgB2/Fe tapes fabricated by an in situ powder-in-tube method using MgH2 as a precursor powder.* Superconductor Science & Technology, 2006. **19**(2): p. 161-168.

167. Scanlan, R.M., A.P. Malozemoff, and D.C. Larbalestier, *Superconducting materials for large scale applications.* Proceedings of the Ieee, 2004. **92**(10): p. 1639-1654.

168. Dhalle, M., P. Toulemonde, C. Beneduce, N. Musolino, M. Decroux, and R. Flukiger, *Transport and inductive critical current densities in superconducting MgB2.* Physica C-Superconductivity and Its Applications, 2001. **363**(3): p. 155-165.

169. Young, R.A., *The Rietveld Method*. International Union of Crystallography book series. 1996: University Press.

170. Roisnel, J.R.-C.T., *FullProf.98*. 1998.

171. H & M Analytical Services, I. *Analysis of residual stresses*. 2002 [cited 2007-02-04]; Available from: http://www.h-and-m-analytical.com/pdfs/grazing_incidence.pdf.

172. Eyidi, D., O. Eibl, T. Wenzel, K.G. Nickel, M. Giovannini, and A. Saccone, *Phase analysis of superconducting polycrystalline MgB2.* Micron, 2003. **34**(2): p. 85-96.

173. Chen, D.X. and R.B. Goldfarb, *Kim Model for Magnetization of Type-Ii Superconductors.* Journal of Applied Physics, 1989. **66**(6): p. 2489-2500.

174. Indrakanti, S.S., V.F. Nesterenko, M.B. Maple, N.A. Frederick, W.H. Yuhasz, and S. Li, *Hot isostatic pressing of bulk magnesium diboride: mechanical and superconducting properties.* Philosophical Magazine Letters, 2001. **81**(12): p. 849-857.

175. Jung, C.U., H.J. Kim, M.S. Park, M.S. Kim, J.Y. Kim, Z. Du, S.I. Lee, K.H. Kim, J.B. Betts, M. Jaime, A.H. Lacerda, and G.S. Boebinger, *Effects of unreacted Mg impurities on the transport properties of MgB2.* Physica C-Superconductivity and Its Applications, 2002. **377**(1-2): p. 21-25.

176. Kayed, T.S., *Magnetoresistance, voltage-current characteristics, and Hall effect measurements of bulk MgB2 superconductors.* Crystal Research and Technology, 2004. **39**(1): p. 50-55.

177. Lee, H.B., Y.C. Kim, and D.Y. Jeong, *Non-special atmosphere synthesis for MgB2.* Journal of the Korean Physical Society, 2006. **48**(2): p. 279-282.

178. Singh, K.P., V.P.S. Awana, M. Shahabuddin, M. Husain, R.B. Saxena, R. Nigam, M.A. Ansari, A. Gupta, H. Narayan, S.K. Halder, and H. Kishan, *Phase formation and superconductivity of Fe-TUBE encapsulated and vacuum-annealed MgB2.* Modern Physics Letters B, 2006. **20**(27): p. 1763-1769.

179. Qin, M.J., S. Keshavarzi, S. Soltanian, X.L. Wang, H.K. Liu, and S.X. Dou, *Sample-size dependence of the magnetic critical current density in MgB2 superconductors.* Physical Review B, 2004. **69**(1): p. -.

180. Horvat, J., S. Soltanian, A.V. Pan, and X.L. Wang, *Superconducting screening on different length scales in high-quality bulk MgB2 superconductor.* Journal of Applied Physics, 2004. **96**(8): p. 4342-4351.

181. Serquis, A., X.Z. Liao, Y.T. Zhu, J.Y. Coulter, J.Y. Huang, J.O. Willis, D.E. Peterson, F.M. Mueller, N.O. Moreno, J.D. Thompson, V.F. Nesterenko, and S.S. Indrakanti, *Influence of microstructures and crystalline defects on the superconductivity of MgB2.* Journal of Applied Physics, 2002. **92**(1): p. 351-356.